

Physical model and applications of high-efficiency electro-optical conversion devices - volume II

Edited by

Feng Chi, Qiang Xu and Dan Luo

Published in

Frontiers in Physics



FRONTIERS EBOOK COPYRIGHT STATEMENT

The copyright in the text of individual articles in this ebook is the property of their respective authors or their respective institutions or funders. The copyright in graphics and images within each article may be subject to copyright of other parties. In both cases this is subject to a license granted to Frontiers.

The compilation of articles constituting this ebook is the property of Frontiers.

Each article within this ebook, and the ebook itself, are published under the most recent version of the Creative Commons CC-BY licence. The version current at the date of publication of this ebook is CC-BY 4.0. If the CC-BY licence is updated, the licence granted by Frontiers is automatically updated to the new version.

When exercising any right under the CC-BY licence, Frontiers must be attributed as the original publisher of the article or ebook, as applicable.

Authors have the responsibility of ensuring that any graphics or other materials which are the property of others may be included in the CC-BY licence, but this should be checked before relying on the CC-BY licence to reproduce those materials. Any copyright notices relating to those materials must be complied with.

Copyright and source acknowledgement notices may not be removed and must be displayed in any copy, derivative work or partial copy which includes the elements in question.

All copyright, and all rights therein, are protected by national and international copyright laws. The above represents a summary only. For further information please read Frontiers' Conditions for Website Use and Copyright Statement, and the applicable CC-BY licence.

ISSN 1664-8714
ISBN 978-2-83251-967-7
DOI 10.3389/978-2-83251-967-7

About Frontiers

Frontiers is more than just an open access publisher of scholarly articles: it is a pioneering approach to the world of academia, radically improving the way scholarly research is managed. The grand vision of Frontiers is a world where all people have an equal opportunity to seek, share and generate knowledge. Frontiers provides immediate and permanent online open access to all its publications, but this alone is not enough to realize our grand goals.

Frontiers journal series

The Frontiers journal series is a multi-tier and interdisciplinary set of open-access, online journals, promising a paradigm shift from the current review, selection and dissemination processes in academic publishing. All Frontiers journals are driven by researchers for researchers; therefore, they constitute a service to the scholarly community. At the same time, the *Frontiers journal series* operates on a revolutionary invention, the tiered publishing system, initially addressing specific communities of scholars, and gradually climbing up to broader public understanding, thus serving the interests of the lay society, too.

Dedication to quality

Each Frontiers article is a landmark of the highest quality, thanks to genuinely collaborative interactions between authors and review editors, who include some of the world's best academicians. Research must be certified by peers before entering a stream of knowledge that may eventually reach the public - and shape society; therefore, Frontiers only applies the most rigorous and unbiased reviews. Frontiers revolutionizes research publishing by freely delivering the most outstanding research, evaluated with no bias from both the academic and social point of view. By applying the most advanced information technologies, Frontiers is catapulting scholarly publishing into a new generation.

What are Frontiers Research Topics?

Frontiers Research Topics are very popular trademarks of the *Frontiers journals series*: they are collections of at least ten articles, all centered on a particular subject. With their unique mix of varied contributions from Original Research to Review Articles, Frontiers Research Topics unify the most influential researchers, the latest key findings and historical advances in a hot research area.

Find out more on how to host your own Frontiers Research Topic or contribute to one as an author by contacting the Frontiers editorial office: frontiersin.org/about/contact

Physical model and applications of high-efficiency electro-optical conversion devices - volume II

Topic editors

Feng Chi — University of Electronic Science and Technology of China, China

Qiang Xu — Nanyang Technological University, Singapore

Dan Luo — University of Waterloo, Canada

Citation

Chi, F., Xu, Q., Luo, D., eds. (2023). *Physical model and applications of high-efficiency electro-optical conversion devices - volume II*.

Lausanne: Frontiers Media SA. doi: 10.3389/978-2-83251-967-7

Table of contents

- 04 **Editorial: Physical model and applications of high-efficiency electro-optical conversion devices, volume II**
Feng Chi, Qiang Xu and Dan Luo
- 06 **An arc multi-electrode pixel structure for improving the response speed of electrowetting displays**
Shufa Lai, Lixia Tian, Shitao Shen, Dong Yuan and Biao Tang
- 14 **Electronic global-shutter one-thin-film-transistor active pixel sensor array with a pixel pitch of 50 μm and photoconductive gain greater than 100 for large-area dynamic imaging**
Yunfeng Hu, Yangbing Xu, Jinming Liu, Yihong Qi and Kai Wang
- 21 **Quantum dot scanning tunneling microscopy for Majorana bound states in continuum**
Hai-Rui Zhang and Yong-Ping Sun
- 29 **Reflectivity enhancement of full color tri-layer electrowetting display with polymer cholesteric liquid crystal films**
Beibei Zhang, Xiaoling Liao, Lijuan Xie, Biao Tang, Xin Zhou, Huapeng Ye and Dong Yuan
- 38 **Filling model of oil and polar liquid for electrowetting displays based on phase change**
Hongwei Jiang, Rongzhen Qian, Wenwen Chen, Rui Zhou and Guofu Zhou
- 47 **A high integration electrowetting displays system based on AC driving model**
Shixiao Li, Yijian Xu, Zhiyu Zhan, Linwei Liu and Pengfei Bai
- 59 **An extensible driving model for multiple grayscales colorful electrowetting displays**
Taiyuan Zhang, Yuanyuan Guo, Yong Deng and Hailing Sun
- 68 **A study on the influence of dose rate on total ionizing dose effect of anti-fuse field programmable gate array—The irradiation damage is attenuated at low dose rate**
Minqiang Liu, Xianguo Xu, Chao Zeng and Cen Xiong
- 75 **Andreev reflection mediated by Majorana zero modes in T-shaped double quantum dots**
Lian-Liang Sun and Jia Liu
- 82 **A 10 bit 1 MS/s SAR ADC with one LSB common-mode shift energy-efficient switching scheme for image sensor**
Yunfeng Hu, Lexing Hu, Bin Tang and Zichuan Yi



OPEN ACCESS

EDITED AND REVIEWED BY
Lorenzo Pavesi,
University of Trento, Italy

*CORRESPONDENCE

Feng Chi,
✉ chifeng@semi.ac.cn

SPECIALTY SECTION

This article was submitted to Optics and Photonics, a section of the journal Frontiers in Physics

RECEIVED 15 March 2023
ACCEPTED 27 March 2023
PUBLISHED 03 April 2023

CITATION

Chi F, Xu Q and Luo D (2023), Editorial: Physical model and applications of high-efficiency electro-optical conversion devices, volume II.
Front. Phys. 11:1186740.
doi: 10.3389/fphy.2023.1186740

COPYRIGHT

© 2023 Chi, Xu and Luo. This is an open-access article distributed under the terms of the [Creative Commons Attribution License \(CC BY\)](https://creativecommons.org/licenses/by/4.0/). The use, distribution or reproduction in other forums is permitted, provided the original author(s) and the copyright owner(s) are credited and that the original publication in this journal is cited, in accordance with accepted academic practice. No use, distribution or reproduction is permitted which does not comply with these terms.

Editorial: Physical model and applications of high-efficiency electro-optical conversion devices, volume II

Feng Chi^{1*}, Qiang Xu² and Dan Luo³

¹Zhongshan Institute, College of Electron and Information, University of Electronic Science and Technology of China, Zhongshan, China, ²Nanyang Technological University Singapore, Singapore, ³University of Waterloo, Waterloo, ON, Canada

KEYWORDS

electro-optical conversion, electrowetting displays, quantum dot, majorana bound 10 states, image sensor, field programmable gate array

Editorial on the Research Topic

Physical model and applications of high-efficiency electro-optical conversion devices, volume II

The realization of optoelectronic devices is driven by the optimization of their physical models, which determine the properties of the electro-optical conversion, energy harvesting, light-emitting, logic gates, and displays, *etc.* [1] Driven by the above demands, we have organized the present Research Topic and collected ten papers that can be classified into four research directions. This is the second volume on this Research Topic, the first has been published.

The first research direction focuses on electrowetting displays (EWDs) [2] with five papers. An arc multi-electrode pixel structure based on the electric wetting principle was proposed to improve the response speed of pixels in EWDs by Lai *et al.* They simulated the influence of the arc multipole pixel structure on the response speed by establishing a three-dimensional model. The effect of the driving sequence on oil movement in pixels was analyzed. Similarly, Zhang *et al.* proposed an EWD structure based on three cholesteric liquid crystal materials. It had an independent PCLC reflection film to improve the reflectivity and gamut width of EWDs. Their experimental results showed that this structure provided a new idea for improving the luminance and color gamut of current EWDs. In addition, the filling of oil and polar liquid would also affect the performance of EWDs. Therefore, Jiang *et al.* proposed a phase change filling structure to solve the defects of low video response speed and low luminance caused by the filling process. The structure provided a way to effectively shorten the filling and coupling times of the EWD panel, and thus to improve oil's controllability so as to obtain a good response time and aperture ratio. Specifically, designing a new structure could compensate for limitations of EWD devices, enhance its driving performance, and expand its application in the display field. An extensible driving waveform for multiple grayscale colorful EWDs was proposed to realize an 18-bit color dynamic display on an extended display matrix by Zhang *et al.* The driving waveform of the color grayscale display was designed by using a grayscale model and a color display model. And then, a large-size display based on a matrix panel was realized by using the extensible driving model. Similarly, an alternating current (AC) driving

waveform was proposed to improve the static image display instability and residual phenomenon caused by charge trapping and contact angle hysteresis by Li et al.. A highly integrated EWD system was constructed by using Xilinx field programmable gate array (FPGA). In addition, an asymmetric intermediate frequency AC driving waveform was proposed to eliminate video artifacts. The driving waveform was used to effectively solve the problem of residual and static images to achieve a highly smooth display output and provide a reliable test solution for EWDs.

The second direction contains two papers from Hu et al. In their first paper, they proposed a 10 bit 1 MS/s SAR ADC with one LSB common-mode shift energy efficient switching scheme for image sensor. The ADC design is based on the two sub-capacitor arrays architecture, the common-mode technique, low power dynamic comparator, bootstrap sampling switch and low-power Bit-Slice logic circuit. Simulated in 180 nm CMOS process and 1 MS/s sampling rate, the ADC achieves the 60.06 dB SNDR, the 75.43 dB SFDR and the 10.45 μ W power consumption. In their second paper, a 256×256 active pixel image sensor array based on a 3-D dual-gate photosensitive thin-film transistor was presented. The pixel pitch, pixel fill factor, photoconductive gain, and the spatial resolution are respectively 50 μ m, 63%, 10^2 – 10^4 and 505 ppi. Such an array is capable of dynamic imaging at a frame rate of 34 Hz.

In the third direction about the Majorana bound states (MBSs) Chi et al., Zhang et al. have studied the spectral function in a quantum dot connected only to one normal metal lead to detect the MBSs, which are formed at the ends of a topological superconductor nanowire and couple to the lead with spin-dependent hybridization strengths. They found that the lead–MBSs interaction induces a bound state characterized by an infinitely high peak in the dot's zero-energy spectral function. The overlap between the two modes of the MBSs turns this bound state into a resonant one, and thus the zero-energy peak is split into three with the height of the central one equaling to that in the absence of lead–MBSs coupling. Sun et al. have studied the Andreev reflection processes in a T-shaped double quantum dots with the central one coupled to the MBSs. They showed that the in-gap state is sensitive to the existence of MBSs, which induce Fano antiresonance in the local density of states at the in-gap state. The differential Andreev conductance also exhibits Fano-type resonance whose tails' directions can be adjusted by the MBSs.

Finally in the fourth research direction, experimental results of Liu et al. showed that the total ionizing dose (TID) irradiation failure

of the FPGA under different dose rates has nothing to do with the input voltage parameter exceeding the standard; with the decrease of cobalt source irradiation dose rate, the TID effect failure dose threshold of the FPGA gradually increased. Their theoretical analysis suggests that the oxide charge annealing effect plays a dominant role, and longer irradiation time is beneficial to the oxide charge annealing.

In conclusion, this editorial is devoted to present the latest progress of the Research Topic: Physical Model and Applications of High-Efficiency Electro-Optical Conversion Devices. Our special thanks to all authors of the articles published on this Research Topic for their valuable contributions and the Frontiers in Physics team for the technical assistance with publishing.

Author contributions

All authors listed have made a substantial, direct and intellectual contribution to the work, and approved it for publication.

Funding

FC acknowledges support from the Engineering Technology Research Center of Colleges and Universities in Guang-Dong Prov-ince (No. 2021GCZX005), the Innovation Team of Colleges and Universities in Guang-Dong Prov-ince (No. 2021KCXTD040).

Conflict of interest

The authors declare that the research was conducted in the absence of any commercial or financial relationships that could be construed as a potential conflict of interest.

Publisher's note

All claims expressed in this article are solely those of the authors and do not necessarily represent those of their affiliated organizations, or those of the publisher, the editors and the reviewers. Any product that may be evaluated in this article, or claim that may be made by its manufacturer, is not guaranteed or endorsed by the publisher.

References

1. Barzanjeh S, Xuereb A, Gröblacher S, Paternostro M, Regal CA, Weig EM. Optomechanics for quantum technologies. *Nat Phys* (2022) 18:15–24. doi:10.1038/s41567-021-01402-0
2. Lan L, Zou J, Jiang C, Liu B, Wang L, Peng J. Inkjet printing for electroluminescent devices: Emissive materials, film formation, and display prototypes. *Front Optoelectron* (2017) 10:329–52. doi:10.1007/s12200-017-0765-x



OPEN ACCESS

EDITED BY

Feng Chi,
University of Electronic Science and
Technology of China, China

REVIEWED BY

Qinhao Lin,
Guangdong University of Technology,
China
Wei Li,
Shunde Polytechnic, China

*CORRESPONDENCE

Shitao Shen,
shenshitao@scnu.edu.cn

SPECIALTY SECTION

This article was submitted to Optics and
Photonics,
a section of the journal
Frontiers in Physics

RECEIVED 22 June 2022

ACCEPTED 06 July 2022

PUBLISHED 08 August 2022

CITATION

Lai S, Tian L, Shen S, Yuan D and Tang B
(2022), An arc multi-electrode pixel
structure for improving the response
speed of electrowetting displays.
Front. Phys. 10:975317.
doi: 10.3389/fphy.2022.975317

COPYRIGHT

© 2022 Lai, Tian, Shen, Yuan and Tang.
This is an open-access article
distributed under the terms of the
[Creative Commons Attribution License](#)
(CC BY). The use, distribution or
reproduction in other forums is
permitted, provided the original
author(s) and the copyright owner(s) are
credited and that the original
publication in this journal is cited, in
accordance with accepted academic
practice. No use, distribution or
reproduction is permitted which does
not comply with these terms.

An arc multi-electrode pixel structure for improving the response speed of electrowetting displays

Shufa Lai, Lixia Tian, Shitao Shen*, Dong Yuan and Biao Tang

Guangdong Provincial Key Laboratory of Optical Information Materials and Technology, Institute of Electronic Paper Displays, South China Academy of Advanced Optoelectronics, South China Normal University, Guangzhou, China

Electrowetting display (EWD) is a new generation of reflective display technology with low power consumption and high contrast. To improve the response speed of pixels, an arc multi-electrode pixel was proposed, and its performance was verified by using the established three-dimensional model in this paper. According to the model, the influence of the arc multi-electrode pixel structure on response speed was simulated, and the influence of a driving sequence on oil movement inside pixels were analyzed. In addition, comparative experiments of oil movement inside pixels with single-electrode and arc multi-electrode were conducted. Experimental results showed that the response time of the arc multi-electrode structure was 0.9 ms faster than the single-electrode structure in a pixel opening stage. In the pixel closing stage, the oil recovery time can be accelerated by applying a boosting voltage to the electrode corresponding to the oil accumulation area, which was 2.3 ms faster than that of the single-electrode structure.

KEYWORDS

electrowetting display, arc multi-electrode, pixel structure, response speed, simulation

Introduction

Electrowetting is a phenomenon which uses an electric field to change the wettability of solid-liquid surface [1]. In recent years, electrowetting technology has been widely used in chemical industry, bioengineering, display, and other fields [2–4]. Among them, electrowetting displays (EWDs) are a new generation of reflective display technology [5, 6]. Compared with traditional reflective displays, EWDs have the advantages of low power consumption, high contrast, fast response, and full color [7, 8], which is one of the most attractive emerging display technologies [9].

A schematic diagram of EWDs structure is shown in Figure 1. The working principle of EWDs can be described as following two stages: At the first stage (named pixel opening stage), when a large enough voltage is applied, the surface tension between water and oil can be changed, the oil can therefore be squeezed by water, showing the color of the bottom substrate. During the second stage (named pixel closing stage), the voltage is

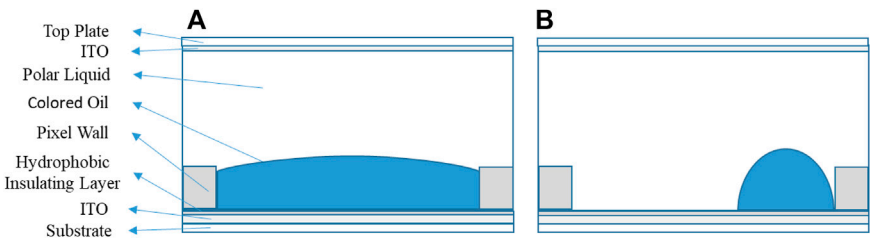


FIGURE 1
Pixel structure of a EWD panel. The structure includes a top plate, ITO, fluid (colored oil and polar liquid), pixel wall, hydrophobic insulating layer, and substrate. Two representative stages show (A) the colored oil spreads on hydrophobic layer as the voltage off, and (B) the colored oil is pushed to a pixel corner when applied a voltage.

TABLE 1 Structure, material, and interface parameters of the model.

Parameters	Quantity	Symbol	Value	Unit
Material	Density of oil	ρ_{oil}	880	kg/m ³
	Density of water	ρ_{water}	998	kg/m ³
	Dynamic viscosity of oil	μ_{oil}	0.004	Pa·s
	Dynamic viscosity of water	μ_{water}	0.001	Pa·s
	Dielectric constant of oil	ϵ_{oil}	4	1
	Dielectric constant of water	ϵ_{water}	80	1
	Dielectric constant of a hydrophobic dielectric layer	ϵ_{hyd}	1.28	1
	Dielectric constant of a pixel wall	ϵ_{pixel_wall}	3.28	1
Structure	Width of a pixel	w_{pixel}	160	μm
	Height of a pixel	d_{pixel}	50	μm
	Height of a pixel wall	d_{pixel_wall}	8	μm
	Width of a pixel wall	w_{pixel_wall}	15	μm
	Thickness of a hydrophobic dielectric layer	d_{hyd}	1	μm
	Thickness of oil	d_{oil}	8	μm
Interfacial	Surface tension of oil and water	γ_{ow}	0.02	N/m
	Contact angle of a pixel wall	θ_{pixel_wall}	95	deg
	Contact angle of a hydrophobic insulating layer	θ_{hyd}	150	deg
	Contact angle of the top plate	θ_{top}	30	deg

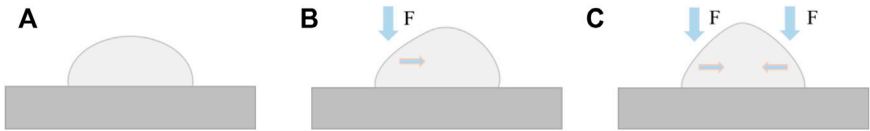
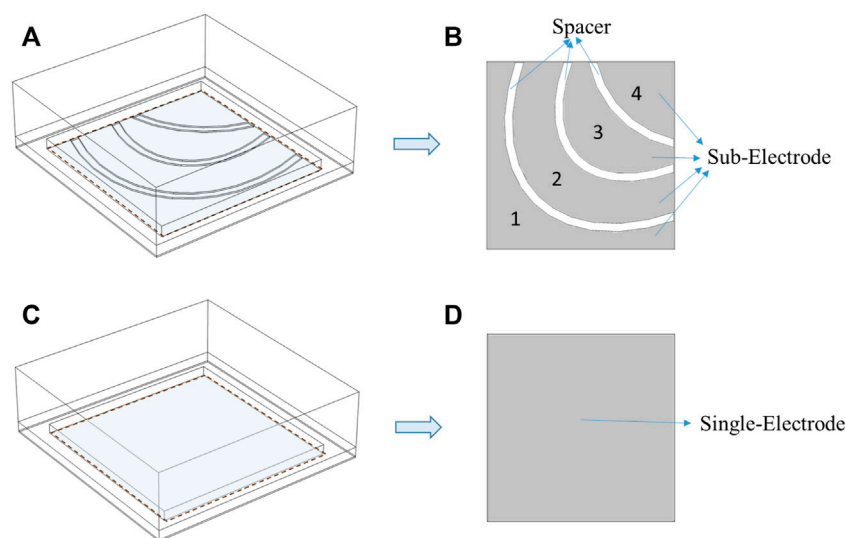


FIGURE 2
Deformation of a sessile droplet exerted by non-contact forces. Vertical arrows indicated the direction of non-contact force, and horizontal arrows indicated the direction of internal droplet velocity. (A) When the sessile droplet was stationary, it was a semicircular shape. (B) When the sessile droplet was subjected to a non-contact force on left, it was deformed on the left, and it had a tendency to move to right. (C) When the sessile droplet was subjected to non-contact force on both sides at the same time, it was deformed on both sides and was contracted to the middle of itself.

turned off, charges accumulated at the polar liquid interface are completely released, resulting in the restore of the original equilibrium between the water and the insulation layer,

showing the color of the oil. So, the effect of dynamic display for EWDs can be achieved. To quantify the response performance, the response time correlative to the on and off

**FIGURE 3**

Arc multi-electrode and single-electrode pixel structure. **(A)** An arc multi-electrode pixel structure. **(B)** The arc multi-electrode contains 4 sub-electrodes and 3 spacers. The width of all spacers was 6 μm . **(C)** A single-electrode pixel structure. **(D)** A single-electrode.

stages of pixels are defined as, 1) on-time refers to the time from applying the driving waveform to reaching the target aperture ratio of pixels. 2) off-time refers to the time from the target aperture ratio to 0.

At present, the response speed of pixels still needs to be improved [10]. In terms of improving the response speed of pixels, an asymmetric driving scheme with alternating positive and negative voltage was proposed. This method could reduce the response time of pixels in the closing stage by suppressing the dielectric charge trapping, thus the fast response of EWDs could be achieved [11]. Similarly, a driving waveform contained an overload phase and a driving phase was proposed. This driving scheme reduced the time required for oil rupture by applying a short overload voltage, thus the purpose of improving pixels response speed could be achieved [12]. From the perspective of fluid characteristics inside pixels, surface tension at the interface of oil/water was considered to be an important factor affecting oil movement. A weak surface tension could increase the aperture ratio of pixels and reduce its response time [13]. In addition, the pixel response speed was also affected by the dynamic viscosity of oil and water. It has been shown that the lower the dynamic viscosity of two immiscible oil/water, the faster the response of pixels [14]. Moreover, the researchers proposed a pixel structure which added spacer arrays to adjacent pixel wall. This structure changed the oil/water interface balance by adding spacers to the pixel wall, it could achieve a consistent oil movement direction and reduce the oil rupture time. Therefore, the response speed of pixels could also be improved [15].

In this work, an arc multi-electrode pixel structure for improving the response speed of EWDs was proposed, and a three-dimensional EWD pixel simulation model was conducted by using COMSOL Multiphysics software. The influence of the arc

multi-electrode and single-electrode on pixel response speed in this model was studied. Furthermore, a scheme for applying recovery waveform on sub-electrodes of arc multi-electrode was proposed to improve the oil recovery speed in the pixel closing stage.

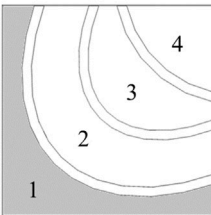
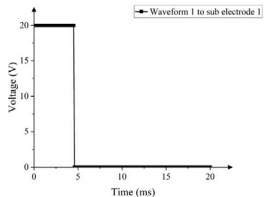
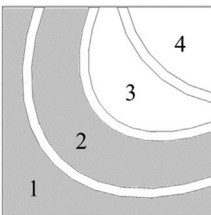
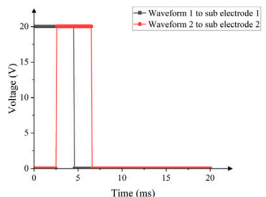
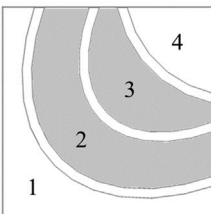
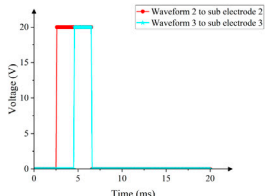
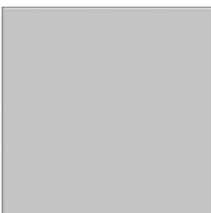
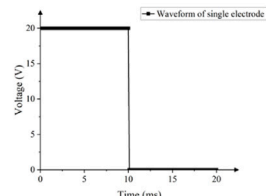
Numerical methodology

The three-dimensional EWD simulation was achieved using the COMSOL Multiphysics software. A laminar flow two-phase flow framework was used in the model. The laminar flow field was coupled with a phase field and an electrostatic field. The problem of fluid flow in the laminar flow field was solved by Navier-Stokes equation. Electrical parameters in the electrostatic field were solved by Maxwell's stress tensor equation. The voltage and electrostatic field force output in the electrostatic field was eventually coupled to the laminar flow field.

Governing equations

A phase-field method is used to build the model and investigate the dynamic process of a two-phase flow interface. A large number of data has been proved that the phase-field method could effectively predict droplet movement on the solid surface [16, 17]. The movement of interface is tracked indirectly by solving two equations. One of them is used to solve phase-field variable ϕ and the other is used to solve the mixed energy density ψ [18–20]. Equations 1–3 represent the governing equation of phase-field [21].

TABLE 2 Driving waveforms and driving mode used for two electrode structures.

Arc multi-electrode (stage one)	 
Arc multi-electrode (stage two)	 
Arc multi-electrode (stage three)	 
Single-electrode	 

$$\frac{\partial \phi}{\partial t} + u \cdot \nabla \phi = \nabla \cdot \frac{\gamma \lambda}{\varepsilon^2} \nabla \psi \quad (1)$$

$$\psi = -\nabla \cdot \varepsilon^2 \nabla \phi + (\phi^2 - 1)\phi + \left(\frac{\varepsilon^2}{\lambda}\right) \frac{\partial f_{ext}}{\partial \phi} \quad (2)$$

$$\sigma = \frac{2\sqrt{2}}{3} \frac{\lambda}{\varepsilon} \quad (3)$$

Where λ is the energy density and ε is the capillary width. Equation 3 describes the relationship between these two parameters and the surface tension coefficient σ . γ is the mobility parameter. ϕ was set to 1 for oil and -1 for water.

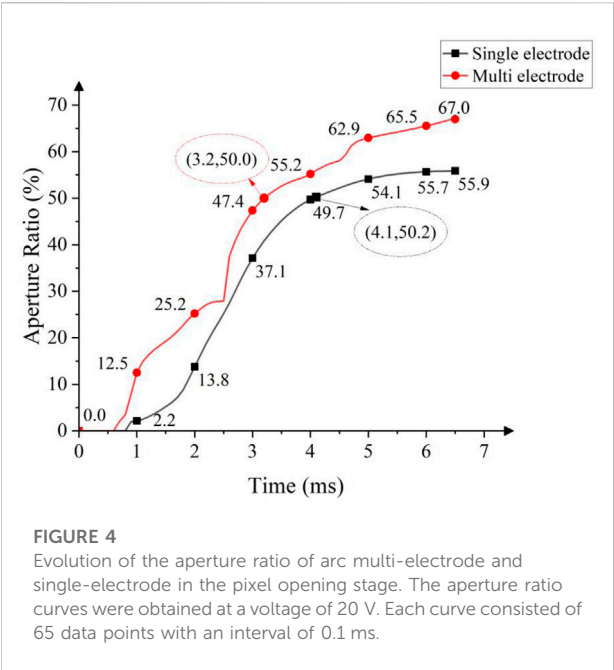
The laminar flow field can be solved by Navier-Stokes equation and continuity equation [22]. Navier-Stokes equation is described as Eq. 4. To depict the movement of two immiscible liquids, a transport of mass and a momentum are governed by incompressible Navier-Stokes equations.

$$\rho \left(\frac{\partial u}{\partial t} + u \cdot \nabla u \right) = -\nabla p + \nabla \cdot \left(\mu (\nabla u + (\nabla u)^T) - \frac{2}{3} u (\nabla \cdot u) I \right) + F \quad (4)$$

$$F = F_{st} + \rho g + F_{vf} \quad (5)$$

Where u , p , ρ , and μ represent velocity, pressure, density, and dynamic viscosity of fluid respectively. Each term in Eq. 4 corresponds to inertial force, pressure, viscous force, and external force, respectively. The external force consists of surface tension, gravity, and a volume force, F_{st} , g , and F_{vf} represent surface tension, gravity acceleration, and volume force, respectively.

As described in Eqs. 4, 5, the coupling between the laminar flow field and the electrostatic field is achieved by applying an electrostatic volume force to Navier-Stokes equation. The electrostatic field force is a main factor that can cause fluid-flowing [18]. In addition, the electrostatic field force can be



obtained by calculating the divergence based on Maxwell Stress Tensor (MST) [18], and the calculation is expressed by Eq. 6.

$$F_{vf} = \nabla T_{ik} \tag{6}$$

In a three-dimensional model simulation, MST is expressed as Eq. 7.

$$T = \begin{bmatrix} T_{xx} & T_{xy} & T_{xz} \\ T_{yx} & T_{yy} & T_{yz} \\ T_{zx} & T_{zy} & T_{zz} \end{bmatrix} \tag{7}$$

The variation of volume force caused by the electrostatic field acts on the interface between oil and water, and the calculation can be expressed by Eq. 8.

$$F = \begin{bmatrix} \frac{\partial(T_{xx})}{\partial x} & \frac{\partial(T_{xy})}{\partial y} & \frac{\partial(T_{xz})}{\partial z} \\ \frac{\partial(T_{yx})}{\partial x} & \frac{\partial(T_{yy})}{\partial y} & \frac{\partial(T_{yz})}{\partial z} \\ \frac{\partial(T_{zx})}{\partial x} & \frac{\partial(T_{zy})}{\partial y} & \frac{\partial(T_{zz})}{\partial z} \end{bmatrix} \tag{8}$$

For the calculation of contact angle, it was shown in Eq. 9 [7].

$$\cos \theta_e = \cos \theta_{hyd} + \frac{\epsilon_0 \epsilon_{hyd} V^2}{2 d_{hyd} \gamma_{ow}} \tag{9}$$

Where θ_e , θ_{hyd} , and γ_{ow} are electrowetting's contact angle, Young's contact angle of hydrophobic dielectric layer, and the surface tension respectively.

Boundary conditions

In the simulation model, the zero-charge boundary condition should be set on all sides of the model. For electrostatic field boundary conditions, the voltage and the ground needed to be specified. The

TABLE 3 Oil movement between arc multi-electrode and single-electrode in the pixel opening stage.

Time (ms)	0	1	2	3	4	5	6	6.5
Single-electrode								
Arc multi-electrode								

TABLE 4 Driving waveform used for the arc multi-electrode structure in the pixel closing stage.

Boosting Stage (6.5-7.5ms)		
-------------------------------	--	--

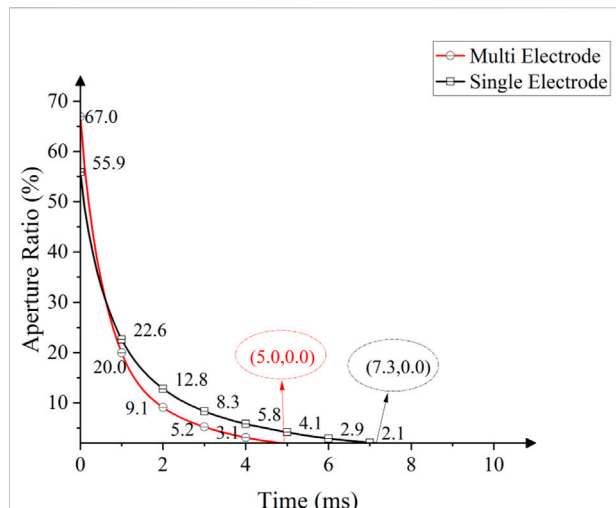


FIGURE 5

Aperture ratio corresponding to arc multi-electrode and single-electrode as a function of time in the pixel closing stage. Each curve consisted of 70 data points with an interval of 0.1 ms. A 15 V boosting voltage was applied to the sub-electrode 4 in the arc multi-electrode, but none at the single-electrode. The oil in the single-electrode was naturally recovered.

wetted wall, the initial interface, and the outlet needed to be specified in phase-field boundary conditions. In addition, the contact angle was defined as the inverse operation of Lippmann-Young equation.

The interface of the two-phase flow was selected as an initial boundary condition. Both sides of the model (except the pixel walls) were selected as inlet and outlet boundary conditions. In addition, initial values of pressure and velocity in the laminar flow field were set to 0. The wall condition was set to Navier-Slip.

Process and discussion

Setting of model parameters

Parameters used in the simulation were shown in Table 1. The fluid (oil and water) in the model was set to incompressible flow. It was assumed that the temperature (25°C) was kept

constant during fluid movement, the thermal expansion of fluid could be ignored. The influence of pressure on dynamic viscosity was ignored. In addition, the bond number described the relationship between gravity and surface tension, and it was far less than 1, thus the gravity could be neglected [18]. Moreover, the polar liquids were replaced by water [23, 24]. To compare the response speed of a single-electrode with that of an arc multi-electrode, the aperture ratio was required to characterize it. The ratio of white area to the pixel area was called aperture ratio, and it could be calculated by Eq. 10.

$$W_A = 1 - \left(\frac{S_{oil}}{S_{pixel}} \right) \times 100\% \quad (10)$$

Where W_A was the aperture ratio, S_{oil} was the area of the colored oil in the pixel, S_{pixel} was the area of the pixel.

Design of arc multi-electrode pixel structure

The arc multi-electrode pixel structure proposed in this paper had a faster response speed than single electrode, which could be elaborated from the following points. In electrowetting, when a droplet was subjected to an asymmetrical electric field force, it would be deformed on the side of the electric field force, which in turn caused the droplet to move [25, 26]. Similarly, in sessile EWDs, when a droplet was stationary, it was a semicircular shape, as shown in Figure 2A. When the droplet was subjected to a non-contact force on left, as shown in Figure 2B, the left droplet was deformed, and its inside would generate a velocity which was directed to the right. When the droplet was subjected to non-contact force on both sides at the same time, the two sides of the droplet were deformed and were contracted to the middle of the droplet, as shown in Figure 2C. In this case, it is not conducive to the droplet movement. Therefore, an asymmetric progressive stress was necessary to improve oil movement inside pixels in EWDs.

The proposed arc multi-electrode pixel structure was shown in Figure 3A, and the structure of source electrode was divided

TABLE 5 Oil movement between arc multi-electrode and single-electrode in the pixel closing stage.

Time (ms)	0	1	2	3	4	5	6	7
Single-Electrode								
Arc multi-Electrode								

into four sub-electrode with arc shape, as shown in [Figure 3B](#). Considering the difference of oil movement in a pixel structure (the oil near the pixel wall moved slowly due to a stronger capillary force, and the oil near the middle of pixel moved fast), spacers at sub-electrodes 1, 2, and 3 were set as an elliptical arc. The width of all spacers was 6 μm . When the spacer was set too large in experiment, it would cause the oil to rupture. If the spacer was set too small, it was meaningless. Other structures in the arc multi-electrode pixel remained the same as a traditional single-electrode pixel structure, as shown in [Figure 3C](#). [Figure 3D](#) described a traditional single-electrode structure in EWDs.

Relationship between driving sequence and oil movement

In the arc multi-electrode structure, corresponding driving waveforms were applied to different sub-electrodes at different times, as shown in [Table 2](#), and all effective voltages were set 20 V. The gray area represented a selected sub-electrode, and waveforms in the table represented driving waveforms applied to the corresponding sub-electrode. In order to push oil to a pixel corner quickly, the driving was implemented in three stages. In stage one, the driving waveform 1 was applied to sub-electrode 1, oil was ruptured in area of electrode 1. In the second stage, the driving waveform 1 was continued to be applied to the sub-electrode 1, it allowed residual oil in the spacer between electrodes 1 and 2 to contract. At the same time, the driving waveform 2 was applied to sub-electrode 2. This driving mode could reduce oil dispersion and push oil to move in a fixed direction. In the third stage, the driving waveform at sub-electrode 1 was released, and the corresponding driving waveform was applied to the second and third sub-electrodes, so that oil was pushed to a pixel corner quickly. In the single-electrode comparison experiment, the same voltage was applied and the effective time was maintained for 10 ms, so oil could be completely opened until it remained unchanged. The mode of driving waveform applied to a single-electrode was shown in [Table 2](#).

After applying driving waveforms mentioned in [Table 2](#), the aperture ratio variation curves of single and arc multi-electrode pixels were shown in [Figure 4](#). In the single-electrode, oil was ruptured at 0.9 ms. It took 4.1 ms for the pixel to reach 50% aperture ratio, and subsequently achieved the maximum aperture ratio of 55.9%. Whereas, in the arc multi-electrode, oil ruptured at 0.7 ms, the response time for pixels to reach 50% aperture ratio was 3.2 ms, and the maximum aperture ratio was 67%. Compared with single-electrode, the arc multi-electrode had obvious advantages in response speed and aperture ratio. The response time was 0.9 ms faster than the single-electrode, and the maximum aperture ratio was 11.1% larger than the single-electrode. [Table 3](#) shows the shrinkage process of oil in a pixel.

Boosting voltage and oil recovery

When driving waveforms were removed, oil naturally spread under the action of its own cohesive energy. In the closing stage of a single-electrode pixel, the time required for a pixel from the maximum aperture ratio to 0 was 7.3 ms. For the arc multi-electrode, a voltage of 15 V was applied to the sub-electrode 4 (area 4 in [Figure 3A](#)) and maintained for 1 ms, as shown in [Table 4](#). The applied voltage generated a driving force acting onto oil, and the driving force would accelerate the recovery of oil. The aperture ratio results of the comparative experiment were shown in [Figure 5](#). The time required for the arc multi-electrode from the maximum aperture ratio to 0 was 5 ms, which was 2.3 ms faster than that of the single-electrode. The recovery process of oil in two pixels was shown in [Table 5](#).

Conclusion

In this paper, an arc multi-electrode EWD pixel structure was proposed to improve the display quality, including aperture ratio and response time. To study the performance of electrode structure, a three-dimensional EWD simulation was carried out. The simulation demonstrates the differences in oil motion patterns between two different pixel structures. By dynamically selecting the driving sub-electrode and driving scheme, the arc multi-electrode effectively accelerated the oil movement and improved the pixel response speed. In terms of aperture ratio, the maximum aperture ratio of arc multi-electrode was 11.1% larger than that of single-electrode. In addition, in the pixel closing stage, oil spreading speed can be significantly accelerated by applying a boosting voltage to the sub-electrode corresponding to the oil accumulation area. The arc multi-electrode pixel structure with multiple electrodes design provides a strategy for actively turning off and flexibly turning on the pixel, which theoretically enables it to break through the upper bound on performance of typical EWDs.

Data availability statement

The raw data supporting the conclusions of this article will be made available by the authors, without undue reservation.

Author contributions

SL, LT, SS, DY, and BT: Investigation, methodology, formal analysis, editing. SL: Writing — review, and editing. SL, LT, and SS contributed to the theoretical background and design of the experiments. DY and BT provided theoretical guidance and the funds. All authors contributed to the article and approved the submitted version.

Funding

Supported by the National Key R&D Program of China (2021YFB3600602), Natural Science Foundation of Guangdong Province (No. 2021A1515010623), Science and Technology Program of Guangzhou (No. 2019050001), Program for Guangdong Innovative and Entrepreneurial Teams (No. 2019BT02C241), Program for Chang Jiang Scholars and Innovative Research Teams in Universities (No. IRT_17R40), Guangdong Provincial Key Laboratory of Optical Information Materials and Technology (No. 2017B030301007), Guangzhou Key Laboratory of Electronic Paper Displays Materials and Devices (201705030007) and the 111 Project.

References

- Jones TB. An electromechanical interpretation of electrowetting. *J Micromech Microeng* (2005) 15(6):1184–7. doi:10.1088/0960-1317/15/6/008
- Bai PF, Hayes RA, Jin ML, Shui LL, Yi ZC, Wang L, et al. Review of paper-like display technologies. *Prog Electromagnetics Res* (2014) 147:92–113. doi:10.2528/PIER13120405
- Yi ZC, Feng HQ, Zhou XF, Shui LL. Design of an open electrowetting on dielectric device based on printed circuit board by using a parafilm M. *Front Phys* (2020) 8:193. doi:10.3389/fphy.2020.00193
- Feng HQ, Yi ZC, Yang RZ, Qin XF, Shen ST, Zeng WJ, et al. Designing splicing digital microfluidics chips based on polytetrafluoroethylene membrane. *Micromachines* (2020) 11(12):1067. doi:10.3390/mi11121067
- Feenstra BJ, Hayes RA, Camps IJG, Hage LM, Johnson MT, Roques-Carnes T, et al. A video-speed reflective display based on electrowetting: Principle and properties. *J Soc Inf Disp* (2004) 12(3):293. doi:10.1889/1.1825703
- Yi ZC, Liu LW, Wang L, Li W, Shui LL, Zhou GF, et al. A driving system for fast and precise gray-scale response based on amplitude-frequency mixed modulation in TFT electrowetting displays. *Micromachines* (2019) 10(11):732. doi:10.3390/mi10110732
- Li W, Wang L, Zhang TY, Lai SF, Liu LW, He WY, et al. Driving waveform design with rising gradient and sawtooth wave of electrowetting displays for ultra-low power consumption. *Micromachines* (2020) 11(2):145. doi:10.3390/mi11020145
- Yi ZC, Huang ZY, Lai SF, He WY, Wang L, Chi F, et al. Driving waveform design of electrowetting displays based on an exponential function for a stable grayscale and a short driving time. *Micromachines* (2020) 11(3):313. doi:10.3390/mi11030313
- Jin ML, Shen ST, Yi ZC, Zhou GF, Shui LL. Optofluid-based reflective displays. *Micromachines* (2018) 9(4):159. doi:10.3390/mi9040159
- Chiu Y, Liang C, Chen Y, Lee W, Chen H, Wu S, et al. Accurate-gray-level and quick-response driving methods for high-performance electrowetting displays. *J Soc Inf Disp* (2011) 19(11):741–8. doi:10.1889/JSID19.11.741
- Chen YC, Chiu YH, Lee YW, Liang CC. A charge trapping suppression method for quick response electrowetting displays. *SID Symp Dig* (2010) 41(1):842–5. doi:10.1889/1.3500607
- Zeng WJ, Yi ZC, Zhao YM, Zeng WB, Ma SM, Zhou XC, et al. Design of driving waveform based on overdriving voltage for shortening response time in electrowetting displays. *Front Phys* (2021) 9:642682. doi:10.3389/fphy.2021.642682
- Zhao Q, Tang B, Dong B, Li H, Zhou R, Guo Y, et al. Electrowetting on dielectric: Experimental and model study of oil conductivity on rupture voltage. *J Phys D Appl Phys* (2018) 51(19):195102. doi:10.1088/1361-6463/aabb69

Conflict of interest

The authors declare that the research was conducted in the absence of any commercial or financial relationships that could be construed as a potential conflict of interest.

Publisher's note

All claims expressed in this article are solely those of the authors and do not necessarily represent those of their affiliated organizations, or those of the publisher, the editors and the reviewers. Any product that may be evaluated in this article, or claim that may be made by its manufacturer, is not guaranteed or endorsed by the publisher.

- Hong J, Oh JM, Kang KH. Switching time of electrowetting-based Devices. *Int Conf Nanochannels, Microchannels, Minichannels* (2009) 43499:149–54. doi:10.1115/ICNMM2009-82273
- Dou YY, Chen L, Li H, Tang B, Henzen A, Zhou GF, et al. Photolithography fabricated spacer arrays offering mechanical strengthening and oil motion control in electrowetting displays. *Sensors* (2020) 20(2):494. doi:10.3390/s20020494
- Cahn JW, Hilliard JE. Free energy of a nonuniform system. I. Interfacial free energy. *J Chem Phys* (1958) 28(2):258–67. doi:10.1063/1.1744102
- Dolatabadi A, Arzpeyma A, Wood-Adams P, Bhaseen S. A coupled electro-hydrodynamic numerical modeling of droplet actuation by electrowetting. *Colloids Surf A: Physicochemical Eng Aspects* (2008) 323(1/3):28–35. doi:10.1016/j.colsurfa.2007.12.025
- Zhou M, Zhao Q, Tang B, Groenewold J, Hayes RA, Zhou GF, et al. Simplified dynamical model for optical response of electrofluidic displays. *Displays* (2017) 49:26–34. doi:10.1016/j.displa.2017.05.003
- Yurkiv V, Yarin AL, Mashayek F. Modeling of droplet impact onto polarized and nonpolarized dielectric surfaces. *Langmuir* (2018) 34(34):10169–80. doi:10.1021/acs.langmuir.8b01443
- Zhu GP, Yao J, Zhang L, Sun H, Li AF, Shams B, et al. Investigation of the dynamic contact angle using a direct numerical simulation method. *Langmuir* (2016) 32(45):11736–44. doi:10.1021/acs.langmuir.6b02543
- Jones TB, Gunji M, Washizu M, Feldman MJ. Dielectrophoretic liquid actuation and nanodroplet formation. *J Appl Phys* (2001) 89(2):1441–8. doi:10.1063/1.1332799
- Jones TB, Fowler JD, Chang YS, Kim CJ. Frequency-based relationship of electrowetting and dielectrophoretic liquid microactuation. *Langmuir* (2003) 19(18):7646–51. doi:10.1021/la0347511
- Feng HQ, Yi ZC, Sun ZZ, Zeng WJ, Wang L, Yang JJ, et al. A spliceable driving system design for digital microfluidics platform based on indium tin oxide substrate. *J Nanoelectronics Optoelectronics* (2020) 15(9):1127–36. doi:10.1166/jno.2020.2838
- Lai SF, Zhong QH, Sun HL. Driving waveform optimization by simulation and numerical analysis for suppressing oil-splitting in electrowetting displays. *Front Phys* (2021) 9:720515. doi:10.3389/fphy.2021.720515
- Datta S, Kumar P, Das AK. Manipulation of droplets by electrostatic actuation and the related hydrodynamics. *J Indian Inst Sci* (2019) 99(1):121–41. doi:10.1007/s41745-019-0101-0
- Li J, Ha NS, Liu T, van Dam RM, Kim CJ. Ionic-surfactant-mediated electrowetting for digital microfluidics. *Nature* (2019) 572:507–10. doi:10.1038/s41586-019-1491-x



OPEN ACCESS

EDITED BY

Qiang Xu,
Nanyang Technological University,
Singapore

REVIEWED BY

Zhidong Lin,
Wuhan Institute of Technology, China
Xiaowen Zhang,
Guilin University of Electronic
Technology, China

*CORRESPONDENCE

Kai Wang,
wangkai23@mail.sysu.edu.cn

SPECIALTY SECTION

This article was submitted to Optics and
Photonics,
a section of the journal
Frontiers in Physics

RECEIVED 22 July 2022

ACCEPTED 22 August 2022

PUBLISHED 09 September 2022

CITATION

Hu Y, Xu Y, Liu J, Qi Y and Wang K (2022),
Electronic global-shutter one-thin-
film-transistor active pixel sensor array
with a pixel pitch of 50 μm and
photoconductive gain greater than
100 for large-area dynamic imaging.
Front. Phys. 10:1000909.
doi: 10.3389/fphy.2022.1000909

COPYRIGHT

© 2022 Hu, Xu, Liu, Qi and Wang. This is
an open-access article distributed
under the terms of the [Creative
Commons Attribution License \(CC BY\)](#).
The use, distribution or reproduction in
other forums is permitted, provided the
original author(s) and the copyright
owner(s) are credited and that the
original publication in this journal is
cited, in accordance with accepted
academic practice. No use, distribution
or reproduction is permitted which does
not comply with these terms.

Electronic global-shutter one-thin-film-transistor active pixel sensor array with a pixel pitch of 50 μm and photoconductive gain greater than 100 for large-area dynamic imaging

Yunfeng Hu¹, Yangbing Xu², Jinming Liu², Yihong Qi² and
Kai Wang^{2*}

¹University of Electronic Science and Technology of China, Zhongshan Institute, Zhongshan, Guangdong, China, ²State Key Laboratory of Optoelectronic Materials and Technologies, Guangdong Province Key Laboratory of Display Material and Technology, School of Electronics and Information Technology, Sun Yat-sen University, Guangzhou, Guangdong, China

In large-area dynamic imaging, an active pixel sensor (APS) is proposed. However, there is a trade-off between signal-to-noise ratio (SNR) and spatial resolution. To resolve this, a 256 × 256 active pixel image sensor array based on a 3-D dual-gate photosensitive thin-film transistor (TFT) is presented in this work, with a pixel pitch of 50 μm , pixel fill factor of 63%, photoconductive gain of 10^2 – 10^4 and spatial resolution of 505 ppi. An electronic global shutter is enabled by dual-gate biasing without additional a shutter TFT. Such an array is capable of dynamic imaging at a frame rate of 34 Hz.

KEYWORDS

large-area dynamic imaging, electronic global-shutter, one-TFT APS, sensor array, photoconductive gain

1 Introduction

Large-area optical image sensor manufactured by thin-film technologies can be found in numerous applications such as flat-panel X-ray detector and optical fingerprint scanning [1–11]. High sensitivity, high spatial resolution, and high speed of response are desirable particularly for dynamic imaging. Conventionally, a pixel consists of a photodetector (PD) and a thin-film transistor (TFT) switch in a passive pixel sensor (PPS) architecture. However, PPS is slow, suffers from low signal to noise ratio (SNR) and is incapable of supporting correlated double sampling (CDS) to remove the noise. To improve the SNR and enable the CDS, an active pixel sensor (APS) with an in-pixel amplifier is designed. APS integrates a PD with multiple TFTs

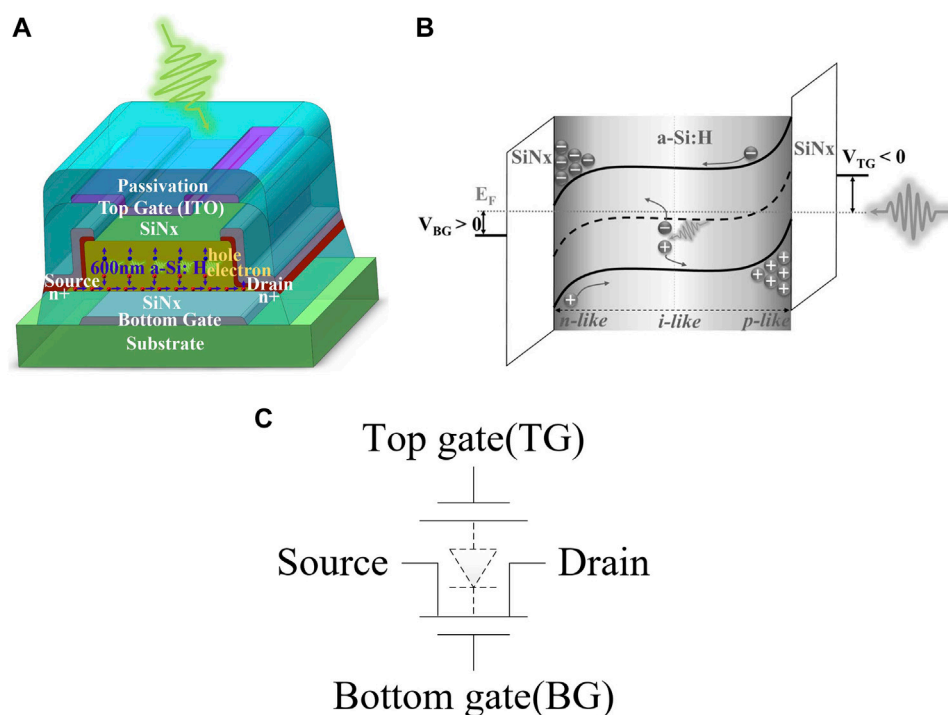


FIGURE 1
Diagram of pixel. (A) Pixel structure; (B) band diagram; (C) Equivalent circuit.

into one pixel. Consequently, it trades high SNR off against high spatial resolution and high fill factor [12–14]. The previous work reported one TFT APS aiming for high SNR, short sampling time, and high fill factor [15]. Even though it results in a decent increase in fill factor as opposed to the 3-TFT APSs, an integration capacitor is still needed to replace a reset TFT [15]. To take an image of a fast-moving object, a CMOS image sensor implements electronic global shutter. As for large-area dynamic imaging, a 4-TFT APS including one additional shutter TFT was proposed in the previous work [16]. However, it inevitably increases the pixel size and reduces the resolution. Despite all aforementioned efforts, the trade-off between SNR, fill factor, and spatial resolution still remains. To resolve the trade-off between SNR and resolution, we have proposed one-TFT APS concept for large area imaging applications [17–20]. This work presents an electronic global-shutter one-Thin-Film-Transistor active pixel sensor array with a pixel pitch of $50\ \mu\text{m}$ and photoconductive gain greater than 100 for large-area dynamic imaging.

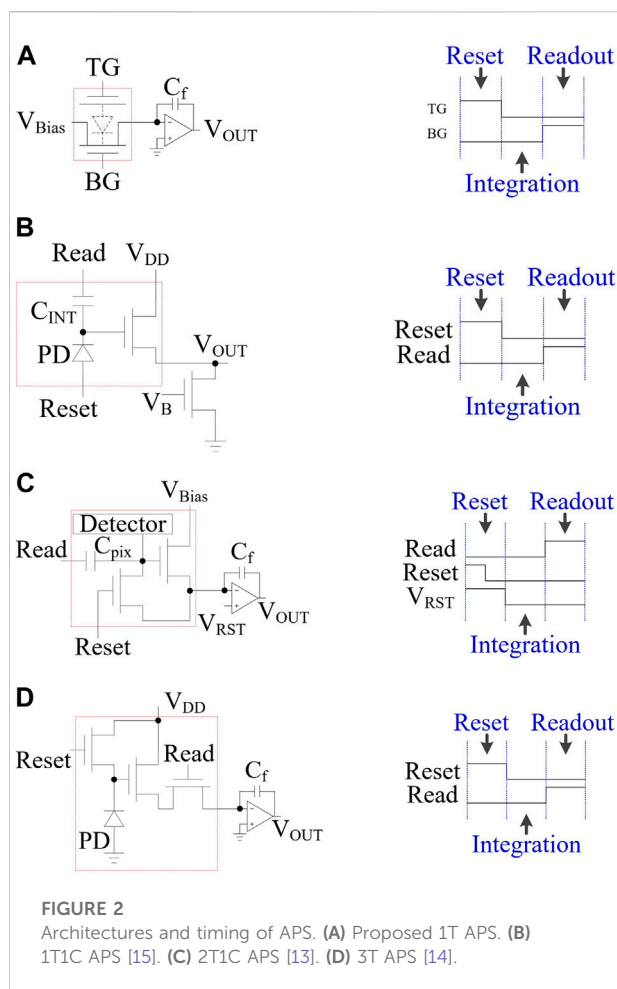
The design of the proposed sensor array is depicted in Section 2. The measured results and the performance summary are discussed in Section 3, and finally, we conclude this work in Section 4.

2 Design of sensor array

2.1 Pixel design of sensor array

In this work, we report an amorphous silicon (a-Si:H) TFT-based 256×256 image sensor array based on electronic-global-shutter one-TFT APS for high-resolution, high-sensitivity, and large-area dynamic imaging applications. Different from improving the spatial resolution by shrinking the TFT size in exchange for a smaller pixel, high resolution in this work is rather achieved by vertically embedding a PD and a switch to form a dual-gate photosensitive TFT.

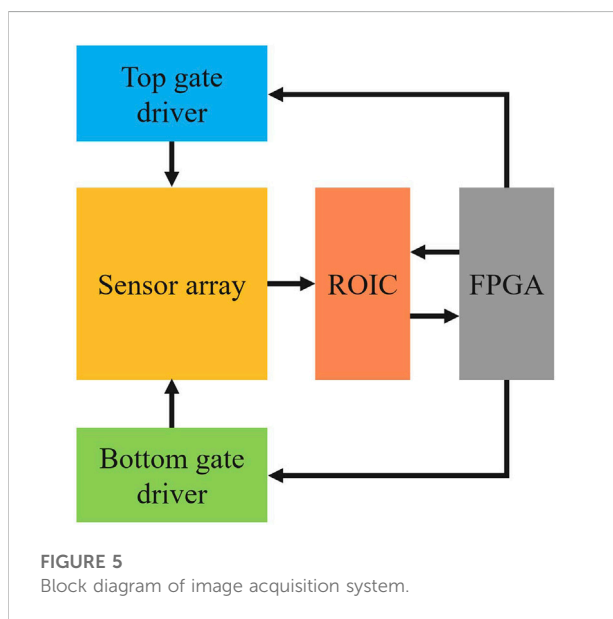
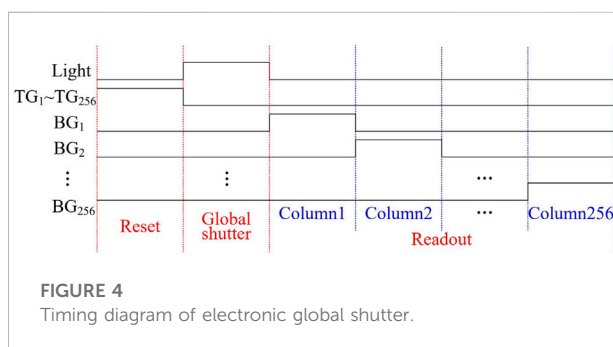
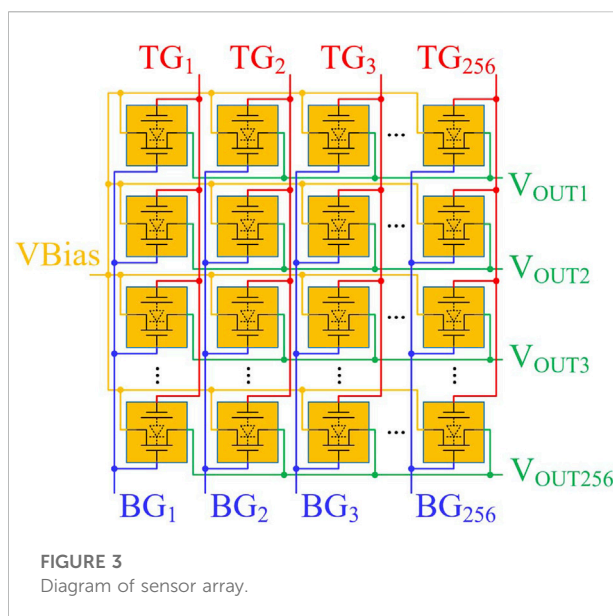
The schematic pixel structure can be found in Figure 1A. In order to make the TFT photosensitive, a-Si:H channel layer is built in a three-dimensional (3-D) π -shape. Through externally biasing both gates, an internal electric field is created and accordingly separates photo-generated electron-hole pairs and makes the 3-D π -shape channel region become a “virtual” PIN-like PD as seen in the schematic band diagram in Figure 1B. The bottom-gate TFT is therefore PD-gated and its threshold voltage will be light-dependent due to quasi-Fermi level shift upon light exposure as shown in Figure 1B. Figure 1C is the equivalent circuit of the pixel. Such a 3-D dual-gate photosensitive TFT combines a PD, a storage capacitor, and a switch, making pixel fill factor of 63%. High spatial resolution



can be attained easily with only one TFT in the pixel. In this work, the image sensor array with $45\ \mu\text{m} \times 55\ \mu\text{m}$ pixel size and 505 ppi resolution was successfully fabricated in an industrial G2.5 TFT-LCD mass production line.

2.2 Timing schemes of sensor array

Figure 2 plots the circuitry diagrams and timing schemes of the proposed one-TFT APS along with the other APS circuits. Similarly, the one-TFT APS presented in this work allows a three-phase pixel operation of reset, integration and readout and the CDS can be enabled by simply applying a reset pulse to the top gate for pixel resetting. The sampling time of the pixel is mainly governed by the resetting operation. Compared with the previous APSs, the proposed one-TFT APS removes the external reset TFT and the external PD as well, thus a reduced pixel sampling time is expected. With a small RC constant, the resetting in this pixel circuit can be done quickly, making it capable of very fast dynamic scanning.



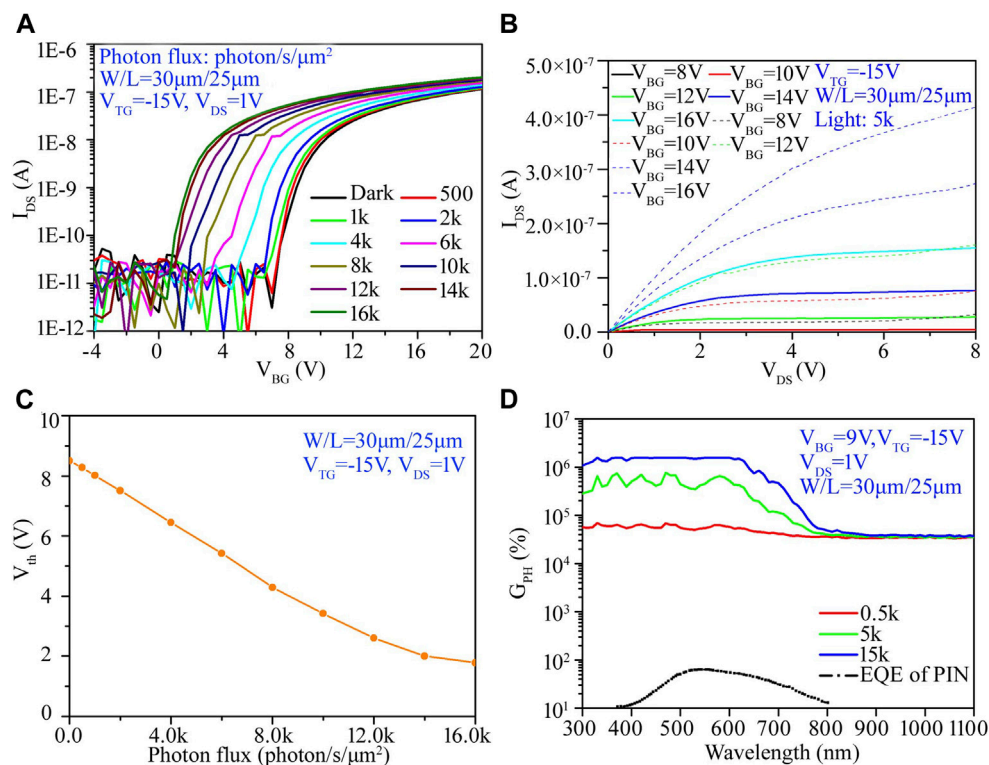


FIGURE 6

Characteristic curve of pixel. (A) Photo transfer characteristics. (B) Output characteristics (dot lines: light; solid lines: dark). (C) Photo-induced threshold voltage (V_{th}) decrease. (D) Gain (G_{Pth}) spectra at various photon fluxes.

The response speed of dynamic imaging is also dependent on electronic shutter technique. The previous APSs mentioned in Figure 2 use electronic roller shutter to acquire images. In some cases of shooting a fast-moving object, the images would be distorted and/or a ghost image would be presented if the frame rate and/or the sensor were slow.

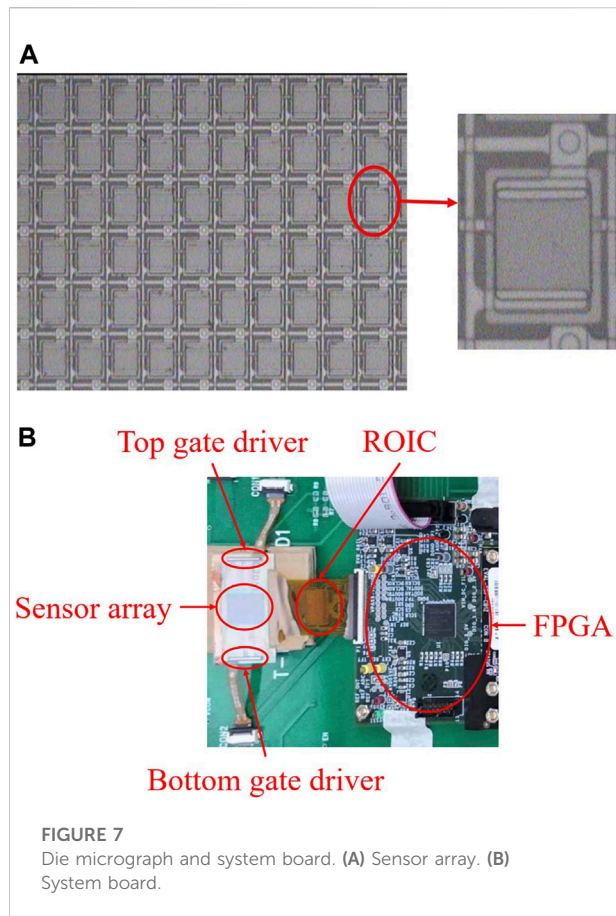
Figure 3 shows the diagram of sensor array. The array has 256 rows and 256 columns. The top gate lines of the pixels in each column are connected and routed from the top direction, the 256-column top-gated interconnects are named from TG_1 to TG_{256} . Similar to the top gate lines, the bottom gate lines of each column are named from BG_1 to BG_{256} . The drains of the pixels in each row are connected and routed from the right direction, which are named from V_{OUT1} to V_{OUT256} . The sources of all pixels are connected to V_{Bias} and routed from the left direction. BG_1 to BG_{256} and TG_1 to TG_{256} are used for timing control, V_{OUT1} to V_{OUT256} are used for signal output, and V_{Bias} is used for voltage bias.

Figure 4 shows the timing scheme of electronic global shutter in the proposed one-TFT APS. Since the

photo-generated charges can be temporarily stored inside the pixel in the integration period through the dual-gate biasing, it is possible to realize electronic global shutter by simply implementing the designed timing scheme in Figure 3 even without a physical shutter TFT. After resetting the whole array, electronic global shutter is initiated by a pulse of light and followed by scanning and reading the array in a sequence.

2.3 Image acquisition system

Figure 5 shows the block diagram of image acquisition system where the sensor array is connected by a top-gated driver IC, a bottom-gated driver IC and a 256-channel readout IC (ROIC). The driver ICs are controlled by the FPGA to provide the driving timing, and the ROIC is controlled by the FPGA to collect analog signals and digitize the signals. The FPGA is used to synchronize the timing clocks and assure that the external ICs and the image sensor array work together well during the dynamic image acquisition.



3 Example demonstration and discussion

Figure 6 illustrates device characteristics of the 3-D dual-gate photosensitive TFT. Upon light exposure, the transfer IV curves

shift negatively, implying that the threshold voltage drops with light and accordingly the output photocurrent increases as observed in both transfer (Figure 6A) and output characteristics (Figure 6B). Further study unveils that the threshold voltage exhibits a quasi-linear relation with the photon flux (Figure 6C). In pursuing high sensitivity, the proposed one-TFT APS differs from the previous APSs in that the high SNR is achieved by operating the dual-gate photosensitive TFT in the subthreshold region where the output current is an exponential function of the threshold voltage. In another word, a small threshold voltage drop upon light exposure will lead to an exponential increase in the output current. As a result, the proposed photosensitive TFT demonstrates a high photoconductive gain of 10^2 – 10^4 , nearly 2–4 orders of magnitude higher than the external quantum efficiency (EQE) of a typical PIN-type PD. It becomes even more important that such a high gain covers an entire studied spectrum with a wavelength ranging from 300 to 1,100 nm. The photosensitive TFT can therefore make a full utilization of all incoming photons in the studied wavelength range and outperform any a-Si:H based PIN-type PDs with an EQE generally below 85% (Figure 6D). Such a high gain can only be found in an avalanche photodiode where a strong electric field must be in presence to trigger avalanche electron multiplication (avalanche effect). However, shot noise also arises under such a strong electric field. Therefore, operating the photosensitive TFT in the subthreshold region becomes a possible approach to achieving high gain while suppressing the noise. Even though operation in the subthreshold region raises a concern of a narrow dynamic range, for low-level light sensing and low-dose dynamic X-ray imaging, high gain and full photon utilization are particularly more important. In the event that does need a wide dynamic range, the dual-gate photosensitive TFT can be tuned to operate in the linear or saturation region where gain is lower but dynamic range becomes wider.

TABLE 1 Comparison table.

	This work	Brown et al. [15]	Taghibakhsh et al. [13]	Karim et al. [14]	Roose et al. [12]
Technology	a-Si:H	CG-Silicon	a-Si:H	a-Si:H	a-IGZO
PD Type	Photosensitive TFT	Lateral PIN	Vertical PIN	Vertical PIN	NA
Gain or EQE of PD	$>10^2$	NA	$<85\%$	$<85\%$	NA
Critical dimension	5 μm	1.5 μm	10 μm	25 μm	3 μm
APS architecture	1T (dual-gate)	1T1C	2T1C	3T	3T1C
Pixel count	256 \times 256	640 \times 480	8 \times 8	3 \times 3	NA
Pixel size (resolution)	45 $\mu\text{m} \times$ 55 μm (505 ppi)	84 $\mu\text{m} \times$ 84 μm (300 ppi)	100 $\mu\text{m} \times$ 100 μm (254 ppi)	250 $\mu\text{m} \times$ 250 μm (102 ppi)	100 $\mu\text{m} \times$ 100 μm (254 ppi)
Pixel fill factor	63%	NA	50%	50%	NA
Frame rate	34 Hz	30 Hz	NA	NA	50 Hz
Electronic shutter	Global shutter	Roller shutter	Roller shutter	Roller shutter	Roller shutter
Operating region of TFT	Subthreshold, linear, saturation	Linear, saturation	Linear, saturation	Linear, saturation	Linear, saturation

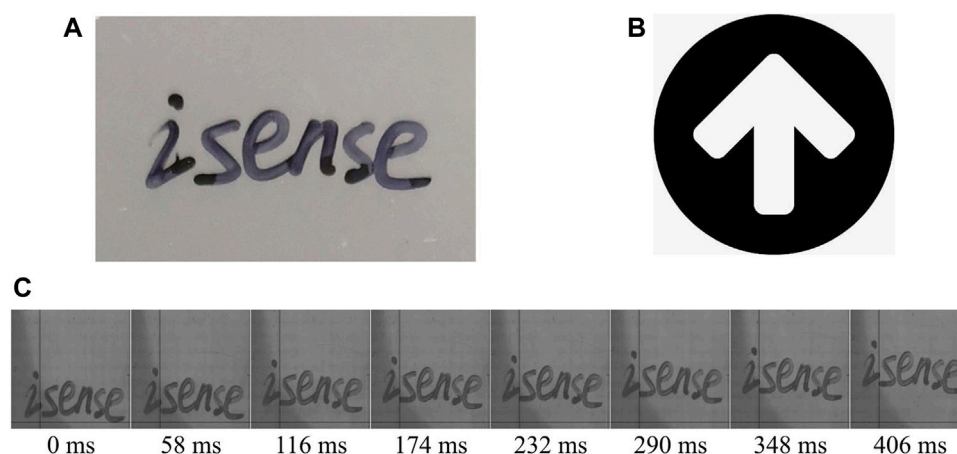


FIGURE 8

Example of dynamic imaging at a frame rate of 34 Hz under light exposure of 11 ms-pulsed green LED. (A) Target image. (B) Moving direction. (C) Sampling frames.

Figure 7 shows the micrograph of sensor array and system board where Figure 7A is a micrograph view of the array including pixels and traces and Figure 7B is a system board including driver ICs, ROIC, and FPGA. As shown, the top gates of each column are connected to the top-gated driver ICs, the bottom gates of each column are connected to the bottom-gated driver IC, and the signal outputs of each row are connected to the ROIC. The top-gated driver IC, bottom-gated driver IC and ROIC are all controlled by the FPGA. The image signal is sent to FPGA by ROIC.

One example of dynamic imaging using electronic global shutter is shown in Figure 8. Figure 8A is the target image with the characters of “isense” written on the transparent plastic. Figure 8B shows the moving direction of the target image. Figure 8C is a moving record of the target image, and the position of the target image is different at different times. In this example, the frame rate is 34 Hz.

A summary table and comparison with the previous works is given in Table 1. This work adopts a 1T APS structure, which has fewer devices than previous work, so it achieves the following advantages: smaller pixel size ($45\ \mu\text{m} \times 55\ \mu\text{m}$), larger resolution (505 ppi), better fill factor (63%), and higher photoconductive gain ($>10^3$). In addition, the array works in global shutter mode, and the frame rate can reach 34 Hz. Moreover, this work can operate in three regions (subthreshold, linear, saturation), while others can only work in two regions (linear, saturation).

4 Conclusion

In conclusion, we demonstrate a 256×256 active pixel image sensor array based on a 3-D dual-gate photosensitive TFT with a pixel pitch of $50\ \mu\text{m}$, pixel fill factor of 63%, photoconductive gain of 10^2 – 10^4 and spatial resolution of

505 ppi. An electronic global shutter is enabled by dual-gate biasing without additional shutter TFT. Such an array is capable of dynamic imaging at a frame rate of 34 Hz.

Data availability statement

The raw data supporting the conclusion of this article will be made available by the authors, without undue reservation.

Author contributions

YH: Designed the image acquisition system, performed the experimental work, and wrote part of the manuscript. YX: Captured the die micrograph of sensor array. JL: Processed image data. YQ: Tested the characteristic curve of pixel. KW: Conceived the project, organized the paper content, wrote, and edited the manuscript.

Funding

This work was financially supported by the National Key Research and Development Project of China (Grant No. 2016YFA0202002).

Conflict of interest

The authors declare that the research was conducted in the absence of any commercial or financial relationships that could be construed as a potential conflict of interest.

Publisher's note

All claims expressed in this article are solely those of the authors and do not necessarily represent those of their affiliated

organizations, or those of the publisher, the editors and the reviewers. Any product that may be evaluated in this article, or claim that may be made by its manufacturer, is not guaranteed or endorsed by the publisher.

References

1. Tiao YS, Sheu ML, Wu SM, Yang HM. Ieee. A cmos readout circuit for ltps-tft capacitive fingerprint sensor. In: 2005 IEEE Conference on Electron Devices and Solid-State Circuits; 19-21 December 2005; Hong Kong, China (2005). p. 631–4. doi:10.1109/EDSSC.2005.1635353
2. Xu M, Ou H, Chen J, Wang K. Evaluation of a single-pixel one-transistor active pixel sensor for fingerprint imaging. In: X Zhang, D Erickson, X Fan, Z Chen, editors. 2015 International Conference on Optical Instruments and Technology: Optical Sensors and Applications; Bellingham. Spie-Int Soc Optical Engineering (2015). doi:10.1117/12.2193336
3. Shin K, KarimA-Si:H KS. a-Si:H TFT-silicon hybrid low-energy X-ray detector. *IEEE Trans Electron Devices* (2017) 64(4):1624–9. doi:10.1109/TED.2017.2671365
4. Weisfield RL. Amorphous silicon tft X-ray image sensors. In: International Electron Devices Meeting 1998 Technical Digest (Cat No98CH36217); 06-09 December 1998; San Francisco, CA, USA (1998). p. 21–4. doi:10.1109/IEDM.1998.746237
5. CH Lee, I Chan, A Nathan, editors. *Mechanical stress and process integration of direct X-ray detector and tft in a-Si: H Technology*. Amorphous and nanocrystalline silicon-based films-2003. Warrendale: Materials Research Society (2003). doi:10.1557/PROC-762-A18.12
6. Sun IK, Sang Wook K, Jae Chul P, Young K, Sang Wook H, Ho Kyung K, et al. Highly sensitive and reliable X-ray detector with Hg₂ photoconductor and oxide drive tft. In: 2011 International Electron Devices Meeting; 05-07 December 2011; Washington, DC, USA (2011). 14.2.1–2.4. doi:10.1109/IEDM.2011.6131550
7. Liu X, Ou H, Chen J, Deng S, Xu N, Wang K. Highly photosensitive dual-gate a-Si:H tft and array for low-dose flat-panel X-ray imaging. *IEEE Photon Technol Lett* (2016) 28(18):1952–5. doi:10.1109/LPT.2016.2579199
8. Safavian N, Chaji GR, Nathan A, Rowlands JA. Three-tft image sensor for real-time digital X-ray imaging. *Electron Lett* (2006) 42(3):150–1. doi:10.1049/el:20063604
9. Huang H, Abbaszadeh S. Recent developments of amorphous selenium-based X-ray detectors: A review. *IEEE Sens J* (2020) 20(4):1694–704. doi:10.1109/JSEN.2019.2950319
10. Roose FD, Steudel S, Malinowski PE, Myny K, Dehaene W. Active pixel concepts for high-resolution large area imagers. In: International Image Sensor Workshop 2015; June 2015; Vaals. 1. (2015).
11. Jeon S, Ahn S-E, Song I, Kim CJ, Chung UI, Lee E, et al. Gated three-terminal device architecture to eliminate persistent photoconductivity in oxide semiconductor photosensor arrays. *Nat Mater* (2012) 11(4):301–5. doi:10.1038/nmat3256
12. Roose FD, Myny K, Steudel S, Willigems M, Smout S, Piessens T, et al. 16.5 a flexible thin-film pixel array with a charge-to-current gain of 59 $\mu\text{A}/\text{pc}$ and 0.33% nonlinearity and a cost effective readout circuit for large-area X-ray imaging. In: 2016 IEEE International Solid-State Circuits Conference (ISSCC); 31 Jan.–4 Feb. 2016; San Francisco, CA, USA. IEEE (2016). p. 296–7. doi:10.1109/ISSCC.2016.7418024
13. Taghibakhsh F, Karim KS. Two-transistor active pixel sensor for high resolution large area digital X-ray imaging. In: 2007 IEEE International Electron Devices Meeting; 10-12 Dec. 2007; Washington, DC, USA. IEEE (2007). p. 1011–4. doi:10.1109/IEDM.2007.4419126
14. Karim KS, Nathan A, Rowlands JA. Amorphous silicon pixel amplifier with/ $\Delta V_{\text{sub T}}$ /compensation for low noise digital fluoroscopy. In: Digest International Electron Devices Meeting; 8-11 Dec. 2002; San Francisco, CA, USA. IEEE (2002). p. 215–8. doi:10.1109/IEDM.2002.1175816
15. Brown C, Hadwen B, Kato H. A 2.6 inch vga lcd with optical input function using a 1-transistor active-pixel sensor. In: 2007 IEEE International Solid-State Circuits Conference Digest of Technical Papers; 11-15 Feb. 2007; San Francisco, CA, USA. IEEE (2007). p. 132–592. doi:10.1109/ISSCC.2007.373623
16. Lai J, Nathan A, Rowlands J. High dynamic range active pixel sensor arrays for digital X-ray imaging using a-Si: H. *J Vacuum Sci Technology A: Vacuum Surf Films* (2006) 24(3):850–3. doi:10.1116/1.2192526
17. Xu YB, Zhou Q, Huang J, Li WW, Chen J, Wang K. Highly-sensitive indirect-conversion X-ray detector with an embedded photodiode formed by a three-dimensional dual-gate thin-film transistor. *J Lightwave Technol* (2020) 38(14):3775–80. doi:10.1109/jlt.2020.2977891
18. Wang K, Qi Y, Hu Y, Xu Y, Xu Y, Liu J, et al. Subthreshold operation of photodiode-gated transistors enabling high-gain optical sensing and imaging applications. *IEEE J Electron Devices Soc* (2020) 8:1236–41. doi:10.1109/JEDS.2020.3022711
19. Wang K, Ou H, Chen J, Nathan A, Deng SZ, Xu NS. 3-D dual-gate photosensitive thin-film transistor architectures based on amorphous silicon. *IEEE Trans Electron Devices* (2017) 64(12):4952–8. doi:10.1109/ted.2017.2760320
20. Ou H, Wang K, Chen J, Nathan A, Deng SZ, Xu NS, et al. Dual-gate photosensitive fin-tft with high photoconductive gain and near-uv to near-ir responsivity. In: 2016 IEEE International Electron Devices Meeting (IEDM); 03-07 December 2016; San Francisco, CA, USA. IEEE (2016). doi:10.1109/IEDM.2016.7838529



OPEN ACCESS

EDITED BY

Qiang Xu,
Nanyang Technological University,
Singapore

REVIEWED BY

Jia Liu,
Inner Mongolia University of Science
and Technology, China
Yingjie Chen,
Qufu Normal University, China

*CORRESPONDENCE

Hai-Rui Zhang,
hxyhjxy@imnc.edu.cn

SPECIALTY SECTION

This article was submitted to Optics and
Photonics,
a section of the journal
Frontiers in Physics

RECEIVED 03 July 2022

ACCEPTED 19 August 2022

PUBLISHED 20 September 2022

CITATION

Zhang H-R and Sun Y-P (2022),
Quantum dot scanning tunneling
microscopy for Majorana bound states
in continuum.
Front. Phys. 10:985198.
doi: 10.3389/fphy.2022.985198

COPYRIGHT

© 2022 Zhang and Sun. This is an open-access article distributed under the terms of the [Creative Commons Attribution License \(CC BY\)](#). The use, distribution or reproduction in other forums is permitted, provided the original author(s) and the copyright owner(s) are credited and that the original publication in this journal is cited, in accordance with accepted academic practice. No use, distribution or reproduction is permitted which does not comply with these terms.

Quantum dot scanning tunneling microscopy for Majorana bound states in continuum

Hai-Rui Zhang^{1*} and Yong-Ping Sun²

¹Department of Environmental Engineering, Hohhot Minzu College, Hohhot, China, ²College of Physics and Electronic Information, Inner Mongolia Normal University, Hohhot, China

We propose a device composed of a quantum dot (QD) connected to a normal metal lead to detect Majorana bound states (MBSs), which are formed at the ends of a topological superconductor nanowire (TSNW) and coupled to the lead with spin-dependent hybridization strengths. The information of the MBSs leaked into the lead is inferred from the spectral function of the QD serving as the tip of a scanning tunneling microscope (STM). It is found that lead–MBSs interaction induces a bound state characterized by an infinitely high peak in the dot's zero-energy spectral function. The overlap between the two modes of the MBSs turns this bound state into a resonant one, and thus the zero-energy peak is split into three with the height of the central one equaling that in the absence of lead–MBSs coupling. We also find that the MBSs have lower impacts on the additional peak in the dot's spectral function induced by intradot Coulomb interaction.

KEYWORDS

quantum dot, Majorana bound states, bound states in continuum, scanning tunneling microscopy, spectral function

1 Introduction

In submicro- and nano-scale systems, the quantum interference effect resulting from electrons transporting through multiple paths or states induces various interesting phenomena that are important in both fundamental and applied subjects [1, 2]. Recently, to enrich physical phenomena, quantum dots (QDs) with well-separated and adjustable energy levels were embedded in the tunneling channels of multiply connected or T-shaped geometries [3–7]. Such energy levels couple to the states with a continuum energy spectrum in the leads that is connected to the central region and thus form exotic bound states in the continuum (BICs). This kind of platform enables the emergence of Fano and Dick effects that originally solely occurred in molecular systems [3, 6]. These two effects are characterized by the asymmetric line shape of the conductance varying with respect to the Fermi energy or dot level, as well as by zero-width resonant peaks in local density of states (LDOS). According to the uncertainty principle, a state with zero-width peak means that its lifetime is infinity and thus is important in applications such as quantum information or quantum storage. A recent experimental work demonstrated that Fano resonances are closely related to quasi-BICs [8]. These effects are also crucial for either fundamental or technological applications. For example, BICs

have been successfully used in designing new kinds of lasers that may be applicable in various fields including photoelectric devices, detection instruments, and quantum information [9]. The quantum interference effects induced by the presence of BICs have also been extensively studied in low-dimensional phononic systems [10]. Experimentally, BICs have been observed in systems beyond electronic ones, for example in optical waveguides arranged in a series [11], dielectric slabs [12], cylinders [13], and nano-scale resonators [9].

Issues related to BICs were also studied in the scope of topological phases of matter [12, 14]. In particular, recent theoretical and experimental work has demonstrated that exotic Majorana bound states (MBSs) can be formed at the ends of p-wave topological superconductor nanowires [15]. The MBSs are quasi-particles of Majorana fermions and of their own antiparticle excitations with zero energy. They are coherent superpositions of electrons and holes and resemble the properties of electron-hole pairs in superconductors. Accordingly, researchers have been seeking Majorana fermions in superconductors since they were predicted as early as in 1937 [16]. In 2008, Fu and Kane first demonstrated the possibility of realizing MBSs in a vortex core in a p-wave superconductor [17]. Subsequently, researchers proved that MBSs may be formed at opposite ends of a one-dimensional p-wave superconductor realized from a semiconductor nanowire with Rashba spin-orbit interaction subjected to both a strong external magnetic field and proximity-induced s-wave superconductor [17]. Until now, MBSs have been successfully prepared in various solid-state platforms, such as topological insulators connected to superconductors [17], defects in topological superconductors [18], semiconductor [19], or ferromagnetic [20] nanowires having strong spin-orbit interaction proximitized to conventional s-wave superconductors, Josephson junctions [21], single monolayer systems [22], and chains of magnetic adatoms [23]. The detection of MBSs remains a challenge. In the past 2 decades, zero-bias conductance peaks [24, 25] were believed to be the most reliable evidence of the existence of MBSs. But some theoretical and experimental works have proved that such an effect can also arise from trivial Andreev bound states and Yu-Shiba-Rusinov states, as well as from the Kondo effect in experimental platforms having a proximitized nanowire connected to a quantum dot (QD) [26, 27]. Due to the controversy regarding the zero-bias abnormal peak related to MBSs, some other means to detect MBSs were subsequently proposed. For example, the presence of MBSs may induce a sign reversion or abnormal enhancement of the power in a hybridized Majorana nanowire/QD system, and can efficiently detect the existence of the MBSs [28–31]. Impacts of MBSs on the properties of tunnel magnetoresistance [32], photo-assisted transport [33–36], and Fano resonance [37–40] were also demonstrated to be promising in the detection of MBSs.

Recently, the generation of BICs by the presence of MBSs was investigated in systems composed of QD and Majorana nanowires, an interesting phenomenon termed MBICs [41–43]. In a departure from earlier work, Vernek et al. proposed to generate and manipulate the MBICs under the condition that both the MBSs and the QD be coupled to an external lead with continuum energy spectrum [44], except when the MBSs and QD are directly connected. The researchers focused on the spectral and transport properties of the hybridized system in both the noninteracting and strong-interacting regimes of the QD [44]. Their numerical results show that there is bound state in the spectral function of the QD, as long as the MBS is coupled to the lead, regardless of the coupling strength. Such a result remains unchanged in the presence of intradot Coulomb interaction and variation of the system temperatures. They explained the physical mechanism of the MBICs by examining the properties of the dot-lead coupling strength under the influence of the MBSs. These results are useful for reading and writing information through veiling and unveiling these states, and they are promising in applications for quantum computing. In the present work, we revisit this system by considering both the MBS–MBS overlap and spin-dependent coupling between the MBSs and the lead, which were neglected in previous work. Experimentally, the two modes of the MBSs formed at opposite ends of the TSNW will interact with each and change the transport properties significantly [21, 24]. Moreover, the MBSs can couple to both spin-up and spin-down electrons, even with different coupling strengths [45, 46]. Our results show that the direct overlap between the two modes of the MBSs may destruct the MBICs under particular conditions, and the spin-dependent coupling between the MBSs and the lead enables the interaction between electrons of opposite spin directions, even in the noninteracting regime. The information of the MBSs at the ends of the TSNW will change the properties of the lead and then leak into the QD when the lead and QD are close enough. By investigating the behavior of the spectral function of the QD, one can infer the existence of the MBSs or the MBICs. The QD thus functions as the tip of an STM to detect the above two phenomena.

2 Model and methods

The system we study here is similar to that in Ref. [44], except that the two modes of the MBSs overlap, and one mode of the MBSs interacts with electrons in a lead with spin-dependent hybridization strength. The lead-dot coupling strength is sensitive to the properties of MBSs and thus to changing the spectral function of the QD. The Hamiltonian of this system can be written in the following form [25, 44]:

$$H = \sum_{k\sigma} \varepsilon_{k\sigma} c_{k\sigma}^\dagger c_{k\sigma} + \sum_{\sigma} \varepsilon_d d_{\sigma}^\dagger d_{\sigma} + U d_{\uparrow}^\dagger d_{\downarrow}^\dagger d_{\downarrow} d_{\uparrow} + \sum_{k\sigma} (t_k c_{k\sigma}^\dagger d_{\sigma} + H.c.) + H_{MBSs}, \quad (1)$$

where $c_{k\sigma}^\dagger$ ($c_{k\sigma}$) creates (annihilates) an electron of momentum k and energy $\varepsilon_{k\sigma}$, which depends on electron spin $\sigma = \uparrow, \downarrow$ in the lead serving as the tip of an STM. The operator d_{σ}^\dagger (d_{σ}) is the creation (annihilation) operator of an electron with gate voltage tunable energy level ε_d , spin- σ , and intradot Coulomb interaction U . The MBSs couple to spinless electrons in the QD because of the chirality properties, which has been studied in previous papers. Experimentally, this happens when the system holding MBSs is subjected to strong magnetic fields that enable only one spin-component electron to dwell on the systems due to the Zeeman splitting effect [25]. When the external magnetic field is not too strong, and both the spin-up and spin-down energy levels of the systems are in the transport window, the MBSs interact with both spin-up and spin-down electrons [24]. The Coulomb repulsion between the electrons is crucial and should be considered. The coupling strength between the QD and the lead is described by t_k . The last term, H_{MBSs} , in Eq. 1 is for the MBSs prepared at opposite ends of a TSNW. Here we consider the case in which only one mode of the MBS is coupled to the electrons on the lead with spin-dependent hybridization strength λ_{σ} [45, 46]:

$$H_{MBSs} = i\delta_M \eta_1 \eta_2 + \sum_{\sigma} \lambda_{\sigma} (d_{\sigma} - d_{\sigma}^\dagger) \eta_1, \quad (2)$$

in which δ_M is the interaction strength between the MBSs whose operators satisfy $\eta_j = \eta_j^\dagger$ ($j = 1, 2$) and $\{\eta_i, \eta_j\} = \delta_{ij}$. The coupling strength between the MBSs and electrons on the lead is λ_{σ} . The information of the MBSs leaked into the lead can be detected non-invasively by investigating the local density of the states (LDOS) ρ_{σ} of the QD attached to the lead [44]. It can be obtained from the imaginary part of the retarded Green's function as $\rho_{\sigma} = -\text{Im}[\langle\langle d_{\sigma} | d_{\sigma}^\dagger \rangle\rangle^r] / \pi$. By adopting the equation-of-motion technique, the Green's function can be expressed in the following matrix form [24, 25, 44]

$$\begin{bmatrix} G_{d,\uparrow}^{r-1} + K\Gamma\Lambda_{\uparrow} & K\Gamma\Lambda_{\uparrow} & K\Gamma\sqrt{\Lambda_{\uparrow}\Lambda_{\downarrow}} & K\Gamma\sqrt{\Lambda_{\uparrow}\Lambda_{\downarrow}} \\ K\Gamma\sqrt{\Lambda_{\uparrow}\Lambda_{\downarrow}} & \tilde{G}_{d,\uparrow}^{r-1} + K\Gamma\Lambda_{\uparrow} & K\Gamma\sqrt{\Lambda_{\uparrow}\Lambda_{\downarrow}} & K\Gamma\sqrt{\Lambda_{\uparrow}\Lambda_{\downarrow}} \\ K\Gamma\sqrt{\Lambda_{\uparrow}\Lambda_{\downarrow}} & K\Gamma\sqrt{\Lambda_{\uparrow}\Lambda_{\downarrow}} & G_{d,\downarrow}^{r-1} + K\Gamma\Lambda_{\downarrow} & K\Gamma\Lambda_{\downarrow} \\ K\Gamma\sqrt{\Lambda_{\uparrow}\Lambda_{\downarrow}} & K\Gamma\sqrt{\Lambda_{\uparrow}\Lambda_{\downarrow}} & K\Gamma\Lambda_{\downarrow} & \tilde{G}_{d,\downarrow}^{r-1} + K\Gamma\Lambda_{\downarrow} \end{bmatrix} \times \begin{bmatrix} \langle\langle d_{\uparrow} | d_{\uparrow}^\dagger \rangle\rangle^r \\ \langle\langle d_{\uparrow}^\dagger | d_{\uparrow}^\dagger \rangle\rangle^r \\ \langle\langle d_{\downarrow} | d_{\uparrow}^\dagger \rangle\rangle^r \\ \langle\langle d_{\uparrow}^\dagger | d_{\downarrow}^\dagger \rangle\rangle^r \end{bmatrix} = \begin{bmatrix} \delta_{\uparrow,\sigma} \\ 0 \\ \delta_{\downarrow,\sigma} \\ 0 \end{bmatrix}, \quad (3)$$

in which the inverse of the QD Green's function is

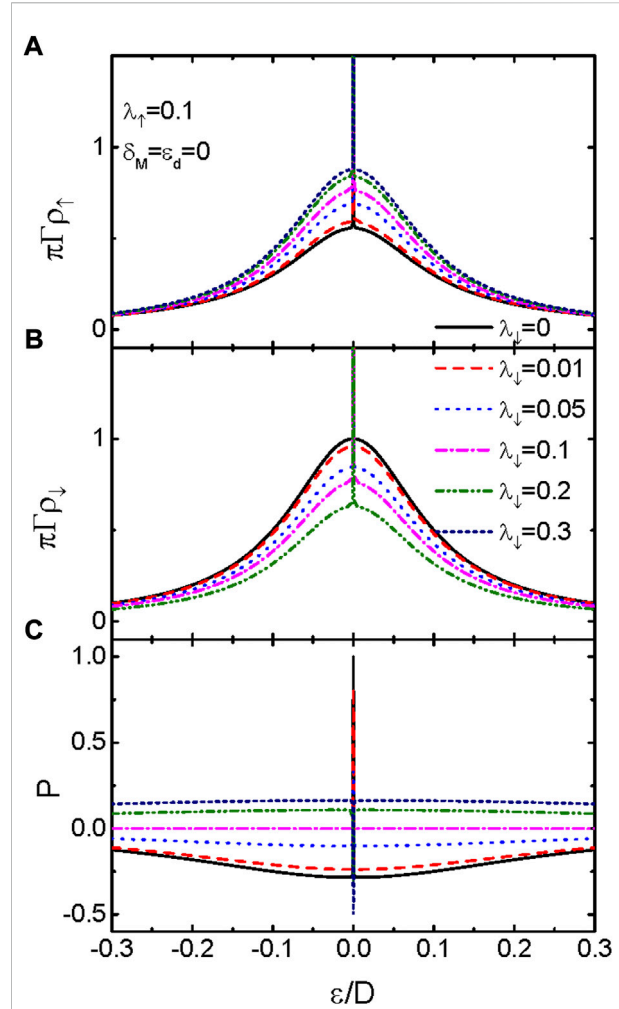


FIGURE 1

(Color online) Spin-up (A) and spin-down (B) LDOS varying as functions of electron energy for different values of λ_l . (C) is for the spin polarization of the LDOS. Other parameters are $U = 0$, $\lambda_{\uparrow} = 0.1$, dot level $\varepsilon_d = 0$, and MBS–MBS interaction strength $\delta_M = 0$. With increasing λ_l , the magnitude of ρ_{\uparrow} (A) and ρ_{\downarrow} (B) is individually enhanced and suppressed. As a result, the spin polarization of the LDOS (C) first decreases, changing its sign, and then increases.

$$G_{d,\sigma}^{r-1} = \frac{(\varepsilon - \varepsilon_d)(\varepsilon - \varepsilon_d - U)}{\varepsilon - \varepsilon_d - U(1 - n_{\sigma})} + i\Gamma, \quad (4)$$

and the Green's function of holes is

$$\tilde{G}_{d,\sigma}^{r-1} = \frac{(\varepsilon + \varepsilon_d)(\varepsilon + \varepsilon_d + U)}{\varepsilon + \varepsilon_d + U(1 - n_{\sigma})} + i\Gamma, \quad (5)$$

where $\sum_{k\in\varepsilon\pm\varepsilon_{k\sigma}} |t_k|^2 = -i\Gamma$, $\sum_{k\in\varepsilon\pm\varepsilon_{k\sigma}} |\lambda_{\sigma}|^2 = -i\Lambda_{\sigma}$, and $K = [\varepsilon + 2i\sum \Lambda_{\sigma} - \delta_M^2/(\varepsilon + i0^+)]^{-1}$. The occupation number n_{σ} must be calculated from the self-consistent equation of $n_{\sigma} = -\int \text{Im}[\langle\langle d_{\sigma} | d_{\sigma}^\dagger \rangle\rangle^r] f(\varepsilon) d\varepsilon / \pi$, with $f(\varepsilon)$ being the Fermi distribution function in the equilibrium state.

3 Results and discussion

In the following numerical calculations, we choose half-band width of the lead $D \equiv 40$ [25] as the energy unit and fix the value of dot-lead coupling strength at $\Gamma = 0.1$. Figure 1 presents the spin-up (a) and spin-down (b) spectral functions and (c) their spin-polarization $P = (\rho_{\uparrow} - \rho_{\downarrow})/(\rho_{\uparrow} + \rho_{\downarrow})$ for different values of spin-down lead-MBS hybridization strength λ_{\downarrow} with fixed $\lambda_{\uparrow} = 0.1$. For $\lambda_{\downarrow} = 0$, the zero-energy spin-up spectral function is $\pi\Gamma\rho_{\uparrow}(\varepsilon = 0) \rightarrow \infty$ (black solid line in Figure 1A), whereas $\pi\Gamma\rho_{\downarrow}(\varepsilon = 0) = 1$ is shown by the solid black line in Figure 1B. This indicates that the MBSs leaked into the lead, inducing a bound state in the QD at zero electron energy. Turning on the coupling between spin-down electrons on the QD and the MBSs in the lead ($\lambda_{\downarrow} \neq 0$), the bound state in spin-up spectral function is stable, which is characterized by $\pi\Gamma\rho_{\uparrow}(\varepsilon = 0) \rightarrow \infty$. Now the zero-energy spectral function of the QD for spin-down electrons also becomes a bound state ($\pi\Gamma\rho_{\downarrow}(\varepsilon = 0) \rightarrow \infty$). Note that the bound state emerges as long as the dot-lead coupling is turned on and is independent in its magnitude. Shifting the QD energy level by gate voltage away from zero energy, it is found that the magnitude of spin-up (spin-down) spectral function is monotonously enhanced (suppressed) by increasing λ_{\downarrow} . The reason is that the MBSs leaked into the QD change the dot level, and then the electron transport probability in each channel (electron state) is lowered. This result is in consistent with earlier works [25, 44].

The bound state induced by the MBSs can be understood by examining the properties of the hybridization between the QD and the lead $K\Lambda_{\sigma}$. As is known from the Green's function, the position of the peaks in the spectral function is determined by the dot level as well as by the real part of the self-energy, and the width (lifetime of the state) of the peaks is related to the value of the imaginary part of the self-energy. A larger (smaller) value of the imaginary part of the self-energy corresponds to wider (narrower) peaks, and hence a longer (shorter) electron life on the energy state. The real part of $K\Lambda_{\sigma}$ will shift the dot level, and its imaginary part determines the broadening of peaks in the spectral function $\pi\Gamma\rho_{\sigma}(\varepsilon)$. As shown in Ref. [44], $-\text{Im}[K\Lambda_{\sigma}]$ is the effective coupling between the QD and the lead with continuum spectrum. Under the conditions of $\lambda_{\sigma} = 0$ and $\varepsilon_d = 0$, $-\text{Im}[K\Lambda_{\sigma}]$ reduces to Γ of the usual case with $\pi\Gamma\rho_{\sigma}(\varepsilon = 0) = 1$. In the presence of coupling between the QD and the continuum ($\lambda_{\sigma} \neq 0$), $-\text{Im}[K\Lambda_{\sigma}] \equiv 0$ at $\varepsilon = 0$ indicates the emergence of a bound state with infinite long-electron dwell time due to the uncertainty relation of $\Delta t \sim \hbar/2\Gamma$. The real part of $K\Lambda_{\sigma}$ however, is zero at $\varepsilon = 0$, and the position of the peak in spectral function is unchanged. Note that the value of $K\Lambda_{\sigma}$ also depends on the dot level ε_d , which is out of the scope of the present work because the MBSs exert significant impacts on the electron transport at zero energy. The spin-polarization of the spectral functions P is shown in Figure 1C. It is found that the value of P depends on both λ_{σ} and electron energy ε . At $\varepsilon = 0$, the spin-polarization is 1 for $\lambda_{\downarrow} = 0$. This means now only spin-up electrons

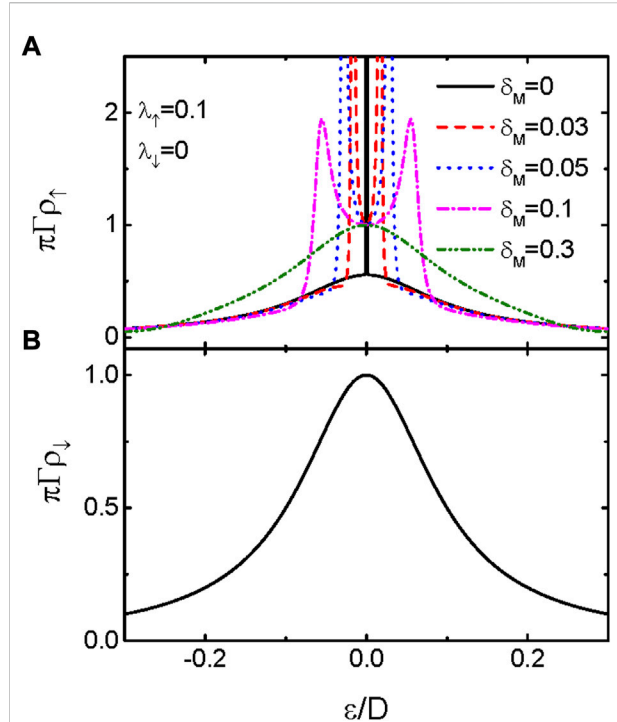


FIGURE 2
(Color online) (A) Spin-up and (B) spin-down LDOS as functions of the electron energy for fixed $\lambda_{\uparrow} = 0.1$, $\lambda_{\downarrow} = 0$, and different values of δ_M . The other parameters are as in Figure 1.

can enter the QD, an ideal case for spintronic devices. With increasing λ_{\downarrow} , the magnitude of the spin-polarization is reduced. Now both spin-up and spin-down electrons can occupy the states on the QD. Interestingly, at sufficiently large λ_{\downarrow} , the value of the spin-polarization is changed from a positive value to a negative one. Now the majority spin in the QD is changed from spin-up to spin-down, and the system can be used as a spin-conversion device by changing the hybridization between the QD and the lead.

In real cases, the two modes of the MBSs prepared at opposite ends of the nanowire overlap with each other with strength $\delta_M \sim \exp(-l/\zeta)$, where l is the length of the nanowire and ζ is directly proportional to the magnetic field applied on the nanowire. The overlap between the MBSs changes their properties significantly, but this fact has been neglected in previous work concerning MBSs coupled to continuum [44]. Figure 2A shows the behavior of $\pi\Gamma\rho_{\uparrow}(\varepsilon)$ for different values of δ_M with fixed $\lambda_{\uparrow} = 0.1$ and $\lambda_{\downarrow} = 0$. As is shown by the black solid line in Figure 2A, a bound state is formed at $\varepsilon = 0$ characterized by infinite large $\pi\Gamma\rho_{\uparrow}$ for δ_M , which is just the case shown in Figure 1. Turning on the hybridization between the two modes of the MBSs ($\delta_M \neq 0$), the zero-energy peak of the spin-up spectral function is split into two. Meanwhile, the two peaks are broadened and lowered. Importantly, the height of the central peak in the spin-up spectral function reduces from

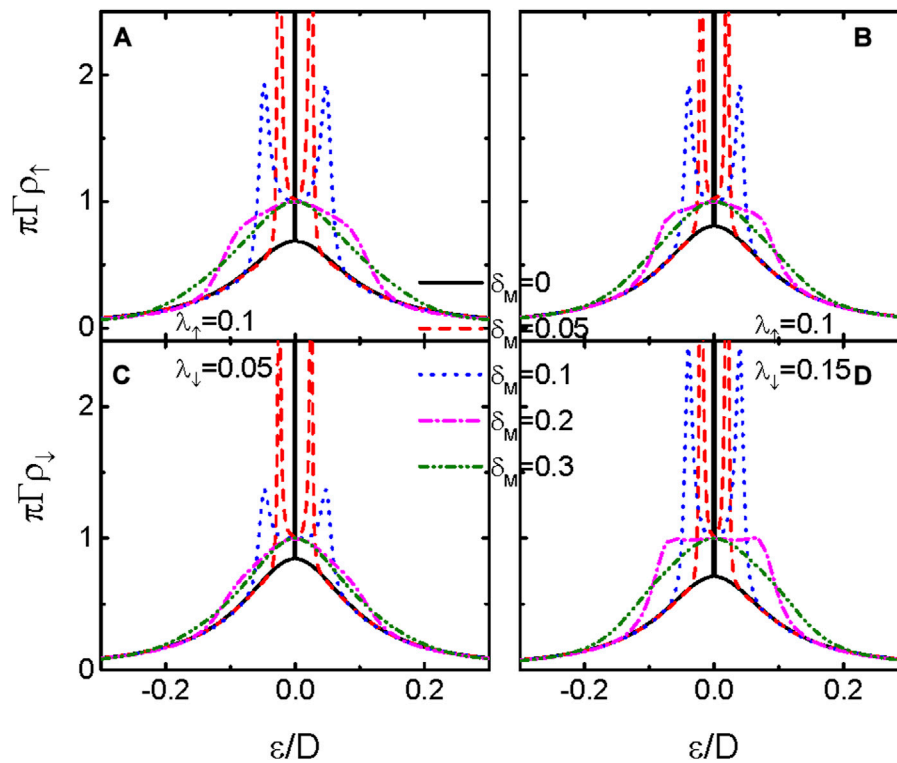


FIGURE 3

(Color online) Spin-resolved LDOS varying with respect to the electron energy for fixed $\lambda_{\uparrow} = 0.1$ and different values of δ_M . The value of λ_{\uparrow} in (A,C) is 0.05, and is fixed at 0.15 in (B,D). The other parameters are as in Figure 1.

infinity to one as long as $\delta_M \neq 0$. For $\delta_M = 0.3$, as is shown by the green dash-dot-dot line, the central peak in $\pi\Gamma\rho_{\uparrow}$ evolves into a broad resonant one. The spin-down spectral function in Figure 2B is unchanged regardless of the value of δ_M , as the spin-down electrons are decoupled from the MBSs ($\lambda_{\downarrow} = 0$). The results shown in Figure 2 indicate that the imaginary part of the effective self-energy $-\text{Im}[K\Gamma\Lambda_{\sigma}]$ no longer equals zero at $\varepsilon = 0$, and the overlap between the two modes of the MBSs destroy the bound state induced by them.

We now study the case in which both spin-up and spin-down electrons are coupled to the MBSs with different hybridization strengths in Figure 3. Similar to the results in Figure 2, in which only spin-up electrons on the QD interact with the MBSs, the single-peak in the spectral functions of the two spin components is split into a broadened and lowered double-peak configuration, indicating the destruction of the bound states by direct hybridization between the two modes of the MBSs. With increasing δ_M , the central peaks in both spin-up and spin-down spectral functions evolve into resonant ones with a fixed value of $\pi\Gamma\rho_{\sigma}(\varepsilon = 0) = 1$. Comparing Figure 3A,C and Figure 3B,D, one finds that the width of the central peak in

the spectral function is changed to be non-monotonous by both λ_{σ} and δ_M . Apart from the Fermi energy $\varepsilon = 0$, the magnitude of the spectral function is enhanced by increasing δ_M , indicating that the impacts of the MBSs on electron transport are weakened by their direct hybridization.

In submicro-nano structures including QD, electron-electron Coulomb interaction can generate some interesting phenomena, such as Coulomb blockade and Kondo effects, that exert significant influences on transport processes. We next show the impacts of intradot Coulomb interaction on the spectral function $\pi\Gamma\rho_{\sigma}(\varepsilon)$ for fixed λ_{\uparrow} and different values of λ_{\downarrow} in Figure 4A,B and different δ_M in Figure 4C,D. It is found that the spectral functions in the presence of intradot Coulomb interaction resemble those in Figures 2, 3, except that an additional peak arises at $\varepsilon = U$. A bound state is also induced by hybridization between the electrons on the QD and the MBSs formed at the ends of the nanowire. As was shown in Ref. [44], even with the effective self-energy $-\text{Im}[K\Gamma\Lambda_{\sigma}] = 0$ at both $\varepsilon = 0$ and U , the state at $\varepsilon = U$ is still a resonant one. The values of λ_{σ} and δ_M mainly change the spectral functions at $\varepsilon = 0$ and have less

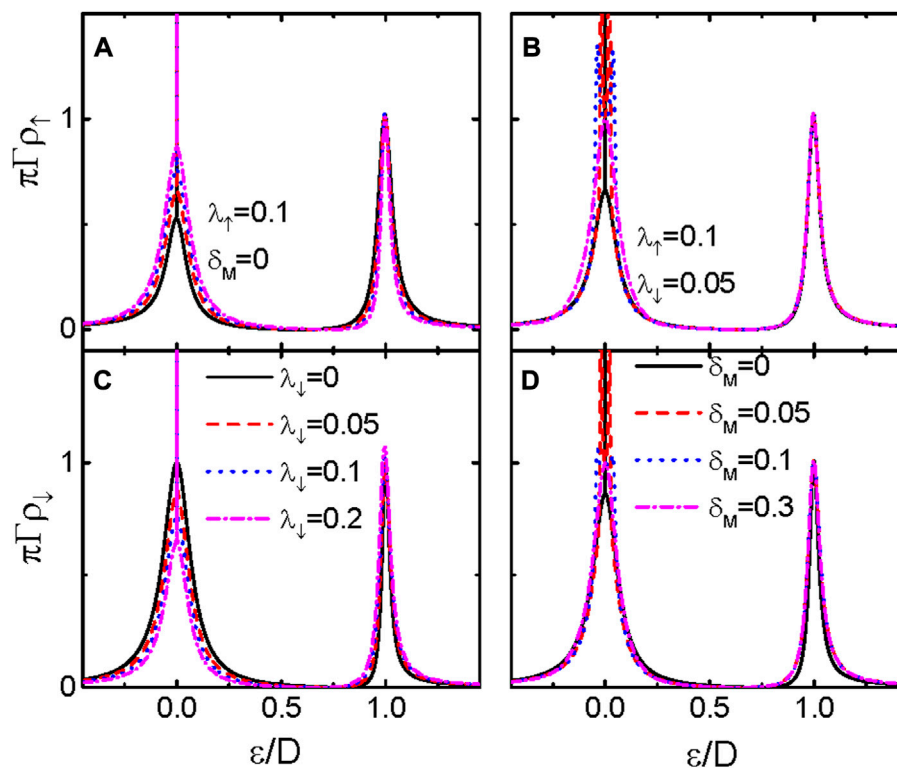


FIGURE 4

(Color online) Spin-up and spin-down LDOS in the presence of intradot Coulomb interaction $U = 1$ as functions of the electron energy for different values of λ_i and $\delta_M = 0$ in (A,D), and $\lambda_i = 0.05$ and different δ_M in (B,C). The value of λ_i is fixed at 0.1. The other parameters are as in Figure 1.

impact on those at $\varepsilon = U$. Moreover, their functions are similar to the non-interacting cases given in Figures 1–3.

4 Summary

In conclusion, we have studied the properties of a QD coupled to a lead with a continuum energy spectrum, which interacts with one mode of the MBSs formed at the ends of a TSNW. Our results show that the spectral function, which is detectable experimentally in terms of techniques of transport spectroscopy, develops a sharp peak with infinite height at zero energy, indicating a bound state induced by the MBSs leaked into the QD. This bound state is destroyed as long as the two modes of the MBSs are overlapped, and the height of the central peak in the spectral function is suppressed from infinity to unit. Moreover, the central peak is split into a double-peak configuration by direct MBS–MBS hybridization. This bound state induced by the MBSs is robust against the presence of the intradot Coulomb interaction, although it generates another peak in the spectral function due to the Coulomb blockade effect. The present device can be used as an STM for the non-invasive detection of MBSs.

Data availability statement

The raw data supporting the conclusion of this article will be made available by the authors, without undue reservation.

Author contributions

H-RZ derived the formulas, performed the numerical calculations, and wrote the original manuscript. Y-PS helped polish the manuscript and discussed the physical mechanisms of the results.

Funding

This study was supported by the Program for 2020 Key Research Items of Hohhot Minzu College (Grant No. HMZD-202004).

Conflict of interest

The authors declare that the research was conducted in the absence of any commercial or financial relationships that could be construed as a potential conflict of interest.

Publisher's note

All claims expressed in this article are solely those of the authors and do not necessarily represent those of their affiliated

References

- Miroshnichenko AE, Flach S, Kivshar YS. Fano resonances in nanoscale structures. *Rev Mod Phys* (2010) 82:2257–98. doi:10.1103/RevModPhys.82.2257
- Hsu CW, Zhen B, Stone AD, Joannopoulos JD, Soljačić M. Bound states in the continuum. *Nat Rev Mater* (2016) 1:16048. doi:10.1038/natrevmats.2016.48
- Hofstetter W, König J, Schoeller H. Kondo correlations and the fano effect in closed aharonov-bohm interferometers. *Phys Rev Lett* (2001) 87:156803. doi:10.1103/PhysRevLett.87.156803
- Yacoby A, Heiblum M, Mahalu D, Shtrikman H. Coherence and phase sensitive measurements in a quantum dot. *Phys Rev Lett* (1995) 74:4047–50. doi:10.1103/PhysRevLett.74.4047
- Kubala B, König J. Flux-dependent level attraction in double-dot aharonov-bohm interferometers. *Phys Rev B* (2002) 65:245301. doi:10.1103/PhysRevB.65.245301
- Guevara MLL, Claro F, Orellana PA. Ghost fano resonance in a double quantum dot molecule attached to leads. *Phys Rev B* (2003) 67:195335. doi:10.1103/PhysRevB.67.195335
- Ueda A, Eto M. Resonant tunneling and fano resonance in quantum dots with electron-phonon interaction. *Phys Rev B* (2006) 73:235353. doi:10.1103/PhysRevB.73.235353
- Melik-Gaykazyan EM, Koshelev K, Choi JH, Kruk SS, Bogdanov A, Park Y, et al. From fano to quasi-bic resonances in individual dielectric nanoantennas. *Nano Lett* (2021) 21:1765–71. doi:10.1021/acs.nanolett.0c04660
- Kodigala A, Lepetit T, Gu Q, Bahari B, Fainman Y, Kanté B. Lasing action from photonic bound states in continuum. *Nature* 541 (2017) 196. doi:10.1038/nature20799
- Huang SB, Liu T, Zhou ZL, Wang X, Zhu J, Li Y. Extreme sound confinement from quasibound states in the continuum. *Phys Rev Appl* (2020) 14:021001. doi:10.1103/PhysRevApplied.14.021001
- Doeleman H, Monticone F, den Hollander W, Alù A, Koenderink AF. Experimental observation of a polarization vortex at an optical bound state in the continuum. *Nat Photon* (2018) 12:397–401. doi:10.1038/s41566-018-0177-5
- Bulgakov EN, Maksimov DN. Topological bound states in the continuum in arrays of dielectric spheres. *Phys Rev Lett* (2017) 118:267401. doi:10.1103/PhysRevLett.118.267401
- Marinica DC, Borisov AG, Shabanov SV. Bound states in the continuum in photonics. *Phys Rev Lett* (2008) 100:183902. doi:10.1103/PhysRevLett.100.183902
- Benalcazar WA, Cerjan A. Bound states in the continuum of higher-order topological insulators. *Phys Rev B* (2020) 101:161116. doi:10.1103/PhysRevB.101.161116
- Wang R, Su W, Zhu J, Ting CS, Li H, Chen C, et al. Kondo signatures of a quantum magnetic impurity in topological superconductors. *Phys Rev Lett* (2019) 122:087001. doi:10.1103/PhysRevLett.122.087001
- Volovik GE. Fermion zero modes on vortices in chiral superconductors. *Jetp Lett* 70 (1999) 609. doi:10.1134/1.568223
- Mourik V, Zuo K, Frolov SM, Plissard SR, Bakkers EPAM, Kouwenhoven LP. Signatures of majorana fermions in hybrid superconductor-semiconductor nanowire devices. *Science* (2012) 336:1003–7. doi:10.1126/science.1222360
- Wimmer M, Akhmerov AR, Medvedeva MV, Tworzydło J, Beenakker CWJ. Majorana bound states without vortices in topological superconductors with electrostatic defects. *Phys Rev Lett* (2010) 105:046803. doi:10.1103/PhysRevLett.105.046803
- Lutchyn RM, Sau JD, Das Sarma SD. Majorana fermions and a topological phase transition in semiconductor-superconductor heterostructures. *Phys Rev Lett* (2010) 105:077001. doi:10.1103/PhysRevLett.105.077001
- Choy TP, Edge JM, Akhmerov AR, Beenakker CWJ. Majorana fermions emerging from magnetic nanoparticles on a superconductor without spin-orbit coupling. *Phys Rev B* (2011) 84:195442. doi:10.1103/PhysRevB.84.195442
- San-Jose P, Prada E, Aguado R. Ac josephson effect in finite-length nanowire junctions with majorana modes. *Phys Rev Lett* (2012) 108:257001. doi:10.1103/PhysRevLett.108.257001
- San-Jose P, Lado JL, Aguado R, Guinea F, Fernández-Rossier J. Majorana zero modes in graphene. *Phys Rev X* (2015) 5:041042. doi:10.1103/PhysRevX.5.041042
- Nadj-Perge S, Drozdov I, Bernevig BA, Yazdani A. Proposal for realizing majorana fermions in chains of magnetic atoms on a superconductor. *Phys Rev B* (2013) 88:020407. doi:10.1103/PhysRevB.88.020407
- Ricco LS, de Souza M, Figueira MS, Shelykh IA, Seridonio AC. Spin-dependent zero-bias peak in a hybrid nanowire-quantum dot system: Distinguishing isolated majorana fermions from andreev bound states. *Phys Rev B* (2019) 99:155159. doi:10.1103/physrevb.99.155159
- Liu DE, Baranger HU. Detecting a majorana-fermion zero mode using a quantum dot. *Phys Rev B* (2011) 84:201308R1–4. doi:10.1103/PhysRevB.84.201308
- He JB, Pan D, Yang G, Liu ML, Ying JH, Lyu ZZ, et al. Nonequilibrium interplay between andreev bound states and kondo effect. *Phys Rev B* (2020) 102:075121. doi:10.1103/PhysRevB.102.075121
- Liu DH, Cao Z, Liu X, Zhang H, Liu DE. Topological kondo device for distinguishing quasi-majorana and majorana signatures. *Phys Rev B* (2021) 104:205125. doi:10.1103/PhysRevB.104.205125
- López R, Lee M, Serra L, Lim J. Thermoelectrical detection of majorana states. *Phys Rev B* 89 (2014) 205418. doi:10.1103/PhysRevB.89.205418
- Hong L, Chi F, Fu ZG, HouWang YKML Z, Wang Z, Li K-M, et al. Large enhancement of thermoelectric effect by majorana bound states coupled to a quantum dot. *J Appl Phys* 127 (2020) 124302. doi:10.1063/1.5125971
- Chi F, Fu ZG, Liu J, Li K, Wang Z, Zhang P. Thermoelectric effect in a correlated quantum dot side-coupled to majorana bound states. *Nanoscale Res Lett* 15 (2020) 79. doi:10.1186/s11671-020-03307-y
- Sun LL, Fu ZG. Spin seebeck effect in a hybridized quantum-dot/majorana-nanowire with spin heat accumulation. *Front Phys* 9 (2021) 750102. doi:10.3389/fphy.2021.750102
- Tang LW, Mao WG. Detection of majorana bound states by sign change of the tunnel magnetoresistance in a quantum dot coupled to ferromagnetic electrodes. *Front Phys* 8 (2020) 147. doi:10.3389/fphy.2020.001471
- Tang HZ, Zhang JJ, Liu J-J. Photon-assisted tunneling through a topological superconductor with majorana bound states. *AIP ADVANCES* 5 (2015) 127129. doi:10.1063/1.4939096
- Chen H, Zhu K. All-optical scheme for detecting the possible majorana signature based on qd and nanomechanical resonator systems. *Sci China Phys Mech Astron* 58 (2015) 1. doi:10.1007/s11433-014-5637-4
- Väyrynen JJ, Rastelli G, Belzig LI, Glazman LI. Microwave signatures of majorana states in a topological josephson junction. *Phys Rev B* 92 (2015) 134508. doi:10.1103/PhysRevB.92.134508
- Chi F, He TY, Wang J, Fu ZG, Liu LM, Liu P, et al. Photon-assisted transport through a quantum dot side-coupled to majorana bound states. *Front Phys* 8 (2020) 2541. doi:10.3389/fphy.2020.00254
- Ueda A, Yokoyama T. Anomalous interference in aharonov-bohm rings with two majorana bound states. *Phys Rev B* (2014) 90:081405. doi:10.1103/PhysRevB.90.081405
- Jiang C, Zheng YS. Fano effect in the Andreev reflection of the Aharonov-Bohm-Fano ring with Majorana bound states. *Solid State Commun* (2015) 212:14–8. doi:10.1016/j.ssc.2015.04.001
- Zeng QB, Chen S, Lü R. Fano effect in an ab interferometer with a quantum dot side-coupled to a single majorana bound state. *Phys Lett A* (2016) 380:951–7. doi:10.1016/j.physleta.2015.12.026
- Chi F, Wang J, He TY, Fu ZG, Zhang P, Zhang XW, et al. Quantum interference effects in quantum dot molecular with majorana bound states. *Front Phys* 8 (2021) 631031. doi:10.3389/fphy.2020.631031

41. Ricco LS, Marques Y, Dessotti FA, Machado RS, de Souza M, Seridonio AC. Decay of bound states in the continuum of majorana fermions induced by vacuum fluctuations: Proposal of qubit technology. *Phys Rev B* (2016) 93:165116. doi:10.1103/PhysRevB.93.165116
42. Guessi LH, Dessotti FA, Marques Y, Ricco LS, Pereira GM, Menegasso P, et al. Encrypting majorana fermion qubits as bound states in the continuum. *Phys Rev B* (2017) 96:041114. doi:10.1103/PhysRevB.96.041114
43. Zambrano D, Ramos-Andrade JP, Orellana PA. Bound states in the continuum poisoned by majorana fermions. *J Phys Condens Matter* (2018) 30:375301. doi:10.1088/1361-648X/aad7ca
44. Ramos-Andrade JP, Orellana PA, Vernek E. Majorana bound state in the continuum: Coupling between a majorana bound state and a quantum dot mediated by a continuum energy spectrum. *Phys Rev B* 101 (2020) 115403. doi:10.1103/PhysRevB.101.115403
45. Hoffman S, Chevallier D, Loss D, Klinovaja J. Spin-dependent coupling between quantum dots and topological quantum wires. *Phys Rev B* (2017) 96:045440. doi:10.1103/PhysRevB.96.045440
46. Górski G, Kucab K. The spin-dependent coupling in the hybrid quantum dot-majorana wire system. *Phys Status Solidi B* (2019) 256:1800492. doi:10.1002/pssb.201800492



OPEN ACCESS

EDITED BY

Qiang Xu,
Nanyang Technological University,
Singapore

REVIEWED BY

Lanying Zhang,
Peking University, China
Zhixian Lin,
Fuzhou University, China

*CORRESPONDENCE

Xin Zhou,
735588385@qq.com
Huapeng Ye,
yehp@m.scnu.edu.cn
Dong Yuan,
yuandong@m.scnu.edu.cn

[†]These authors contributed equally to
this work and share first authorship

SPECIALTY SECTION

This article was submitted to Optics and
Photonics,
a section of the journal
Frontiers in Physics

RECEIVED 06 August 2022

ACCEPTED 22 August 2022

PUBLISHED 29 September 2022

CITATION

Zhang B, Liao X, Xie L, Tang B, Zhou X,
Ye H and Yuan D (2022), Reflectivity
enhancement of full color tri-layer
electrowetting display with polymer
cholesteric liquid crystal films.
Front. Phys. 10:1013102.
doi: 10.3389/fphy.2022.1013102

COPYRIGHT

© 2022 Zhang, Liao, Xie, Tang, Zhou, Ye
and Yuan. This is an open-access article
distributed under the terms of the
[Creative Commons Attribution License](https://creativecommons.org/licenses/by/4.0/)
(CC BY). The use, distribution or
reproduction in other forums is
permitted, provided the original
author(s) and the copyright owner(s) are
credited and that the original
publication in this journal is cited, in
accordance with accepted academic
practice. No use, distribution or
reproduction is permitted which does
not comply with these terms.

Reflectivity enhancement of full color tri-layer electrowetting display with polymer cholesteric liquid crystal films

Beibei Zhang^{1,2,3†}, Xiaoling Liao^{1,3†}, Lijuan Xie^{1,3}, Biao Tang¹,
Xin Zhou^{1,3*}, Huapeng Ye^{1,3*} and Dong Yuan^{1,3*}

¹Guangdong Provincial Key Laboratory of Optical Information Materials and Technology and Institute of Electronic Paper Displays, South China Academy of Advanced Optoelectronics, South China Normal University, Guangzhou, China, ²The Fifth Institute of Electronics, Ministry of Industry and Information Technology, Guangzhou, China, ³SCNU-TUE Joint Lab of Device Integrated Responsive Materials (DIRM), National Center for International Research on Green Optoelectronics, South China Normal University, Guangzhou, China

Electronic paper display has received increasing attention due to its outstanding properties of wide viewing angle, bistable state and lower energy consumption. Among various electronic paper display technologies, electrowetting e-paper (EWD) is the most promising as it can achieve full-color display by using stacked layers or RGB color filter. However, the EWD is faced with several challenges, including poor color brightness, low contrast ratio and small color gamut. To improve the performance of the EWD, we proposed a new configuration of EWD consisting of three independent PCLC reflection films based on the cholesteric liquid crystal materials. We designed and experimentally fabricated three types of reflection films, and then added the PCLC films to the tri-layered EWD device. We experimentally characterized the reflectivity and color gamut of the sample in the dark room. It is found that the experimental results and simulation results match with each other. It is demonstrated that with the PCLC films, the reflectivity is improved by 20%, while the color gamut is improved by 80%, which is sufficient for the daily display demand of E-paper. The proposed EWD device containing PCLC reflection films provide a new strategy to improve the brightness and color gamut of current EWD device, and is promising for realizing the full-color E-paper display.

KEYWORDS

electrowetting display, electronic paper, full-color display, polymer cholesteric liquid crystal, color gamut, reflectance

1 Introduction

Electrowetting display (EWD), which is based on the quick manipulation of microfluid, is a type of reflective electronic paper display technology [1]. Compared with the commercialized electronic paper product of electrophoresis display (EPD), EWD has the same advantages, including low energy consumption, visual healthy and flexibility.

Moreover, EWD is capable of realizing “color” and “video” display simultaneously, which is rather difficult to achieve by other reflective display technologies [2]. Therefore, EWD has become one of the mainstreams of electronic paper display in recent decade.

The concept of EWD was pioneered by G. Beni et al. [3, 4] in 1981, who used the electrowetting effect to manipulate the liquid movement in the pixel structure, so as to change the optical spatial coherence in the pixel, and realize display by switching between white and colored state. Fundamentally, electrowetting is based on electrocapillarity, which was first discovered by Gabriel Lippmann in 1875 and raised the famous Young-Lippmann equation [5]. In 1993, Berge proposed the concept of electrowetting based on dielectric layer [6], which became the basis of modern electrowetting devices [7], such as displays, lenses [8], microfluidic platform [9], heat transfer [10], energy conversion [11] etc. In 2003, Robert A. Hayes reported a video-speed electronic paper based on electrowetting [1], and started the research of EWD technology officially.

So far, the performance of EWD devices have been greatly improved in the past 2 decades, including the reflectivity [12], response time [13] and reliability [14, 15]. EWD prototypes with high brightness and video-speed has also been demonstrated. However, the EWD color display is still unsatisfactory, due to the difficulties in achieving high brightness and high color gamut simultaneously [16]. For reflective color display, the additive color mixing with red (R), green (G) and blue (B) color filter is unfavorable, since each of the color subpixels absorbs roughly 2/3 of the incident white light and thus reduce the brightness/gamut performance [17]. By contrast, subtractive color, mixing with vertical cyan (C), magenta (M) and yellow (Y) stack, is more promising for reflective EWD with wide color gamut while maintaining high reflectivity [18–20]. As reported by H. You et al. [18], the CMY color EWD layers can be switched and are responsible for RGB light control independently in the vertical direction. By controlling the opening rate of each layer, the three primary colors of different gray scales can be obtained, and finally achieve full color display.

Currently, although the multi-layered EWD configuration can achieve high brightness in principle, however, it also causes evident light loss due to the excessive number of functional layers and limit the brightness of the device ultimately. To reduce the light loss, this study report a new approach to enhance the optical performance of the EWD device. Selective reflection films made of polymer cholesteric liquid crystal (PCLC) were added under each layer to reflect the light that has been modulated. The reflectance and color gamut of this new EWD device structure were studied by experiment and simulation, and both results show that this method greatly enhanced the reflectivity and color gamut of tri-layers EWD.

2 Device structure and reflectivity enhancement mechanism

2.1 Full-color EWD device construction

The full color tri-layered EWD device is formed by stacking three monolayer EWD devices, which operates independently and regulates part of the visible light. The working principle of monolayer EWD device is shown in Figure 1A. Specifically, when in the off state, the color ink spreads at the bottom of the pixel and absorbs the corresponding band of light, the pixel presents the color of the ink. When in the on state, the wettability and the contact angle between water and insulator are changed after applying voltage to the upper and lower electrodes. The ink is pushed to the corner of the pixel, and thus the area without ink becomes transparent. Moreover, the opening rates of the oil which depends on the contact angle θ near the three-phase contact line, can be achieved by adjusting the voltage and calculated by the Young-Lippmann equation as shown in Eq. 1.

$$\gamma_{LV} \cos \theta = \gamma_{SV} - \gamma_{SL} + \frac{\epsilon_0 \epsilon_d V^2}{2d} \quad (1)$$

where γ_{LV} , γ_{SV} and γ_{SL} are the interfacial tensions at the solid-gas, liquid-gas and solid-liquid interfaces respectively, ϵ_0 and ϵ_d are the dielectric constants, d is thickness of the hydrophobic insulating layer, V is the applied voltage.

In tri-layered EWD device, CMY oils are used to absorb RGB light respectively. As shown in Figure 1B, when the visible light passes through the layer consisting of Y oil, the blue light is absorbed, whereas the red and green light pass through the Y oil layer. Subsequently, the transmitted light continues to pass through the M oil layer, and the green light is absorbed. In this process, only the red light can pass, and is absorbed by Coil finally. Therefore, when the three layers of ink are spread, the pixels show black. By contrast, when the three layers of ink are contracted, the visible light can pass through the open area, thus resulting in white pixels. It can be inferred that the modulation of the three ink layers on the RGB tri-color light is independent. Moreover, by controlling the open rate of each layer of ink, the absorption of RGB light can be adjusted, and the full-color display can finally be realized.

However, it should be emphasized that the aforementioned mechanism to realize color display suffers from strong losses in the process of light passing through the entire device and reflecting back in a three-layer superimposed EWD device, although in principle other ink layers have no effect on the light outside the absorption spectrum. Taking the blue light as an example, the blue light in the reflected spectrum is regulated by the uppermost yellow ink layer, which has already been completed by the first layer of EWD devices. However, the regulated blue light still needs to pass through the lower two layers of the device to reach the reflective film and again go through the three layers of the device before it comes to human

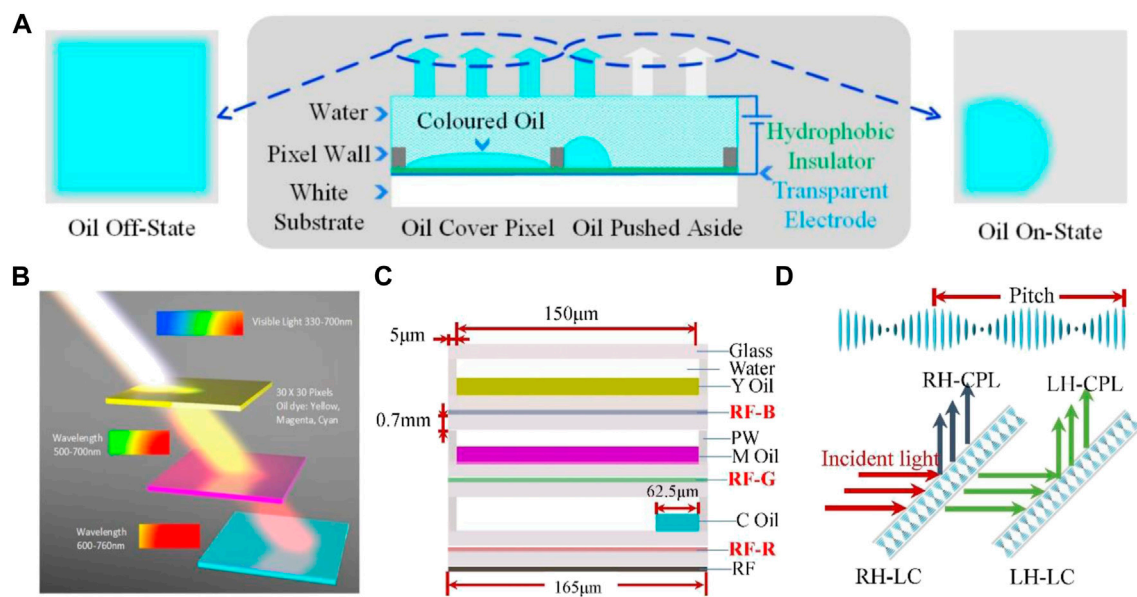


FIGURE 1

Schematic diagram of EWD device: (A) the working principle of EWD technology, (B) the vertical subtractive color mixing mechanism, (C) the basic structure and geometry parameters of tri-layers EWD pixels (here, PW: pixel wall, RF: reflector film), (D) selective reflection principle of PCLC films.

eyes. In this process, the intensity of the blue light is weakened by the absorption of the material, the reflection of the interface and the diffraction of the structure, which eventually leads to a significant reduction in the reflectivity of the blue light.

In order to mitigate this problem, we proposed to place a selective reflective layer under each single-layer device, which helps to reflect the light modulated by the upper ink layer as soon as possible, as shown in Figure 1C. Specifically, a reflection layer (RF-B) corresponding to the band of blue light is added below the yellow ink layer that regulates the blue light. The RF-B layer directly reflects the modulated blue light to prevent the loss of blue light, which may be induced by the structure of the following two layers of devices. Similarly, RF-G and RF-R are also effective in preventing the loss of green and red light, respectively. Thereby, the proposal based on adding three reflective layers are promising in improving the overall reflectivity of the device.

2.2 Enhancement principle of PCLC films

In order to realize the selective reflection of the visible spectrum, PCLC films were employed as the dichromatic reflector in this work. Cholesteric liquid crystal (CLC) is a kind of one-dimensional photonic material with a chiral-spiral structure with Bragg reflective properties, which reflect circularly polarized light in the same direction as its chiral spiral (plus references). According to the Bragg reflection, the reflected band

λ_o of CLC is directly related to its pitch P and refractive index, which can be described by following formula:

$$\lambda_o = \bar{n}P \quad (2)$$

where \bar{n} is the effective refractive index of the liquid crystal material. Liquid crystal is a birefringent crystal material with two refractive indices, namely ordinary refractive index n_o and extraordinary refractive index n_e . The effective refractive index \bar{n} can be calculated with following formula:

$$\bar{n}^2 = \frac{n_e^2 + 2n_o^2}{3} \quad (3)$$

P is the pitch of the CLC, which is the distance at which the liquid crystal molecule rotates in orientation for one circle, as shown in Figure 1D. The reason for choosing the CLC material in this study is that it can adjust the reflection band by adjusting the p value. In principle, the value of P can be realized by adjusting the concentration of the chiral dopant in the liquid crystal material. The pitch of the CLC can be determined by Eq. 4

$$P = \frac{1}{HTP \times c} \quad (4)$$

where c is the concentration of chiral dopant, and HTP is the helical twisting power of chiral dopant in this nematic liquid crystal. Therefore, the reflection band can be adjusted by adjusting the concentration of the dopant.

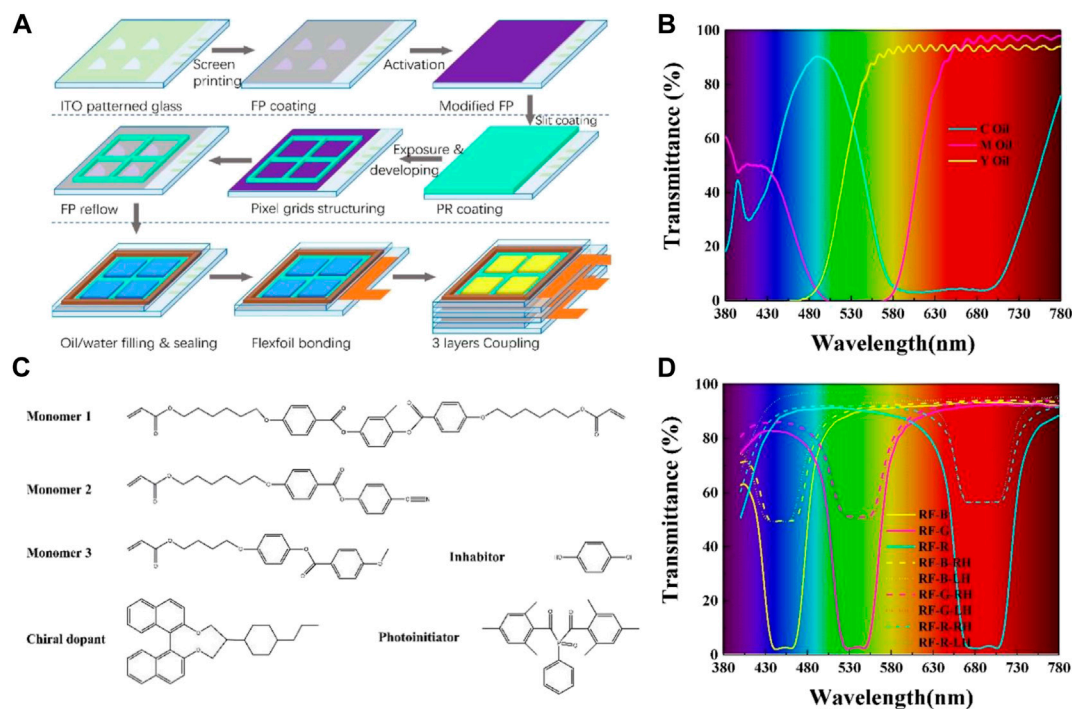


FIGURE 2

Fabrication of tri-layer EWD device and PCLC film: (A) fabrication process of tri-layer EWD device, (B) transmittance spectrum of CMY oil, (C) LC monomer materials for PCLC films and (D) transmittance spectrum of PCLC films.

Another reason for employing the CLC material in this study is that the CLC with optical birefringence has a relatively wide reflective bandwidth, which is compatible with the absorption spectrum of CMY oil. The reflected bandwidth $\Delta\lambda$ of the CLC is related to its birefringence Δn , which is calculated as follows:

$$\Delta\lambda = \lambda_o \frac{\Delta n}{n} = P\Delta n \quad (5)$$

And Δn of liquid crystal material can be calculated with the following Equation:

$$\Delta n = n_e - n_o \quad (6)$$

In this study, the polymerizable liquid crystal monomer material is used as the main body to prepare PCLC film, which can be directly attached to the surface of the EWD substrate. Moreover, since CLC materials can only reflect circular polarized light in the same direction as their chiral helix, two PCLC films with right-handed (RH) and left-handed (LH) rotation respectively are prepared. As shown in Figure 1D, after the incident light passes through the RH PCLC, the RH-CPL (circularly polarized light) is reflected, and the LH-CPL transmitted and is reflected again by the PCLC of the second layer LH, so that the total reflection within a certain bandwidth can be realized. Hence, in this article, PCLC was used to fabricate the RGB tri-color light reflective films that match with the oil

absorption spectrum so as to improve the reflectivity of the EWD device.

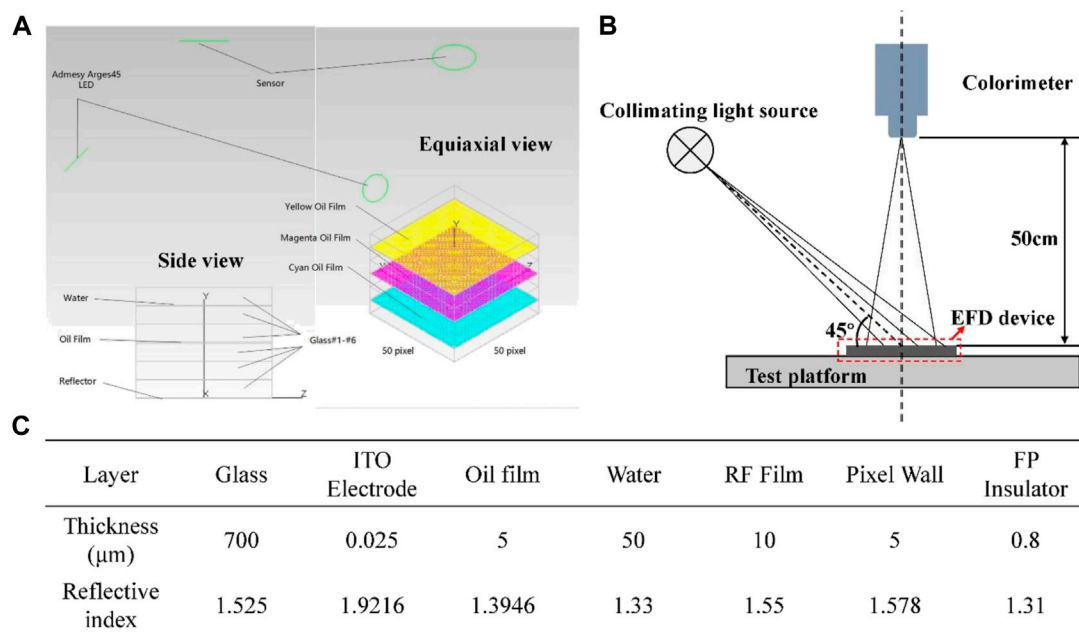
3 Experiment construction

In order to demonstrate the proposed prototype consisting of tri-layer full-color EWD devices and verify the effect of PCLC reflective film on enhancing reflectivity and color gamut, both of simulation and experimental studies are conducted here.

3.1 Device fabrication and characterisation

3.1.1 Fabrication of EWD device

The tri-layer EWD device is fabricated by coupling three separate EWD devices together, as shown in Figure 2A. The detailed fabrication process can be found in our previous publication [20]. The pixel size of the sample is $165 \mu\text{m} \times 165 \mu\text{m}$ with $150 \mu\text{m}$ working area and $15 \mu\text{m}$ pixel wall width. The height of the pixel wall grid composed of photoresist SU8 is $5 \mu\text{m}$. Amorphous fluoropolymer (FP) Teflon AF1600X is used as the insulator layer. The colored oils are prepared via dissolving self-synthesized dyes in oily solvents. The transmittance spectra of CMY oils are measured

**FIGURE 3**

Optical simulation and characterisation of tri-layer EWD device: (A) optical simulation model, (B) optical performance test system, (C) optical and geometrical parameter of functional layers in EWD device.

and shown in Figure 2B. It can be seen that these oils absorb corresponding RGB light and have good transmittance in other wavelength. The oil and water are filled into the cells with 50 μm height and then the whole device is sealed. After bonding FPC, the three EWD layers can be driven separately.

3.1.2 Fabrication of PCLC films

Figure 2C depicts the materials used for producing the PCLC film by photo-copolymerizing three liquid crystalline monomers. The concentration of three monomers is adjusted to have suitable n_e and n_o . In order to adjust the selective reflection wavelength, we varied the concentration and chirality of chiral dopant S/R 5011. Moreover, inhibitor was adopted to avoid premature polymerization. The constituents were mixed by dissolving in the dichloromethane, which was evaporated subsequently. The liquid crystal mixtures were capillary filled into the cells with 5 μm gap and parallel alignment layer on both internal surface at 65°C for 15 min. The cells were then cooled down to 50°C for another 15 min before polymerization to achieve better alignment. The samples were polymerized by UV light source at 50°C, post-cured by heat at 125°C for 15 min to ensure full cure of the acrylate monomers, and then cool down to room temperature on the hot plate slowly. Finally, the cells were opened so to take out the PCLC films.

In this work, six PCLC films, which were designed to reflect the RH-CPL and LH-CPL RGB light respectively, were

fabricated. Figure 2D shows the transmission spectra of these six films, the RH and LH films after stacking. It reveals that the reflection band of PCLC films fits exactly with the absorption band of CMY. In order to maintain the color gamut of the EWD device, the reflected bandwidth is made slightly narrower than the absorption bandwidth of the ink. Moreover, it can be seen that the reflectivity of the film after stack reaches more than 95% in the band where light should be reflected. On the contrary, the transmittance is higher than 90% in the band where light can pass. These PCLC films are added between the EWD layers, as shown in Figure 1C.

3.2 Simulation model establishment

An optical model of tri-layer EWD device is built in software to simulate the effect of adding PCLC films on the reflectivity and color gamut of the device. The side view and equiaxial view of the optical model are shown in Figure 3A. To save computing resource, the model is composed of an array of 50 \times 50 pixels. The geometric and optical parameters of each functional layer are set according to the sample in the experiment, where the thickness and refractive index of each layer are shown in Figure 3C. The absorption spectrum of CMY oil and the reflection spectrum of PCLC films are set according to the results in Figures 2B,D. In the simulation model, the reflector used in the model is the standard Lambert diffuse reflective

surface, and the light source is the D65 standard white parallel light source, which shines on the device at an angle of 45°. A monitor is set vertically above the device as a sensor to record the light intensity and color coordinates of the reflected light. By establishing the switching states of different membrane layers, the reflected light intensity and the reflected light color coordinates of the device when displaying six primary colors (namely RGB, CMY, black and white) are simulated and calculated.

3.3 Optical performance characterisation

In order to optically characterize the performance of EWD devices, a system (Figure 3B) was built in the dark room, according to the electronic paper display measurement standard IEC-62679. In the test system, a collimated D65 light source with divergence angle less than 5° and illuminance higher than 65,000 Lux was used to illuminate on the center of the display screen under test. The angle between the lighting direction and the measured EWD device surface is 45°. To measure the brightness and chromaticity coordinates of the six primary colors on EWD device, a colorimeter (Topcon, SR-UL1R) was putted perpendicular to the surface of the EWD device with a measuring distance of 50 cm.

4 Result and discussion

The reflectivity and color gamut of the tri-layer EWD device are measured to evaluate the effect of PCLC films on the optical performance of the EWD device. In principle, the reflectivity of EWD device is defined as the ratio R between the reflectance of the device and the standard reflector, which can be calculated by the following equation:

$$R = \frac{I_{color}}{I_{reflector}} \times 100\% \quad (7)$$

where I_{color} is the intensity of the reflected light of the EWD device under color states, $I_{reflector}$ is the intensity of the reflected light of standard reflector.

Generally, the color gamut refers to the range of colors that the display device can show. For subtractive color mixing implemented by CMY, the color that can be achieved is the area enclosed by a hexagonal shape on the chromaticity map connected by the color coordinates of the CMYRGB six primary colors. The NTSC color gamut coverage of the display G_{EWD} is usually defined as the ratio between the hexagonal area S_{EWD} and the NTSC standard triangle area S_{NTSC} . It can be calculated by following formula:

$$G_{EWD} = \frac{S_{EWD}}{S_{NTSC}} \times 100\% \quad (8)$$

The value of the S_{NTSC} is 0.1582, and the color display gamut of the device can be calculated by testing the chromaticity coordinates of the display in the C, M, Y, R, G, B primary colors in the CIE1931 chromaticity space.

Figure 4A depicts the simulated reflectivity of the color state of the tri-layer EWD device with and without the PCLC films. The experimentally captured reflectivity of the color state is shown in Figure 4B. They indicate that the reflectivity of the device can be improved effectively by using the PCLC films. Moreover, some differences between simulation and experimental results can also be identified, no matter whether the device contains the PCLC films or not. This is mainly caused by the model simplification, as the actual effect is slightly worse than the simulation effect. However, the trend of the change in the simulation and experimental data is consistent with each other, hence we think the results are reliable. Similar differences are also found in the simulated and experimentally captured color gamut, as shown in Figures 4C,D.

As EWD is a type of reflective display technology, the reflectivity which determines the display brightness is an important parameter. It can be seen from both the simulation and experimental results that the reflectivity of the device has been significantly improved by adding the PCLC films. Specifically, the most significant improvement is the reflectivity of the cyan. For cyan display, it is necessary to open the ink of the upper Y and M layers and close the ink of the lower C layer. In such conditions, the red light is absorbed while the blue light and green light are reflected. This is realized by using the two reflective layers of RF-B and RF-G, which help to reflect the blue light and green light subsequently before they go through the tri-layer device. Therefore, the loss of the blue light and green light is greatly minimized, thus significantly improving the reflectivity of cyan. Similarly, the reflectivity of the blue and green has also been significantly improved. Regarding to the blue, it is necessary to absorb the green and red light, while reflect the blue light. This is accomplished by using the RF-B reflective layer to reflect the blue light after it passing through the uppermost device, thus saving the blue light to the greatest extent. For green, it is necessary to absorb the blue and red light, while reflect the green light. It can be seen from Figure 2B that the bottom cyan ink has a certain absorption of green light. Hence, when the RF-G reflective layer does not need to pass through the lowest layer of the device, the green light reflectance is improved more than the blue light. Meanwhile, the results show that the least increase in reflectivity is the red, due to the fact that the cyan ink that regulates the red light is located in the lowest layer, and the red light must pass through the three-layer device anyway, so the presence or absence of RF has little effect on the reflectivity of the red light. Overall, after the addition of PCLC films, the overall reflectivity of the device has been increased by more

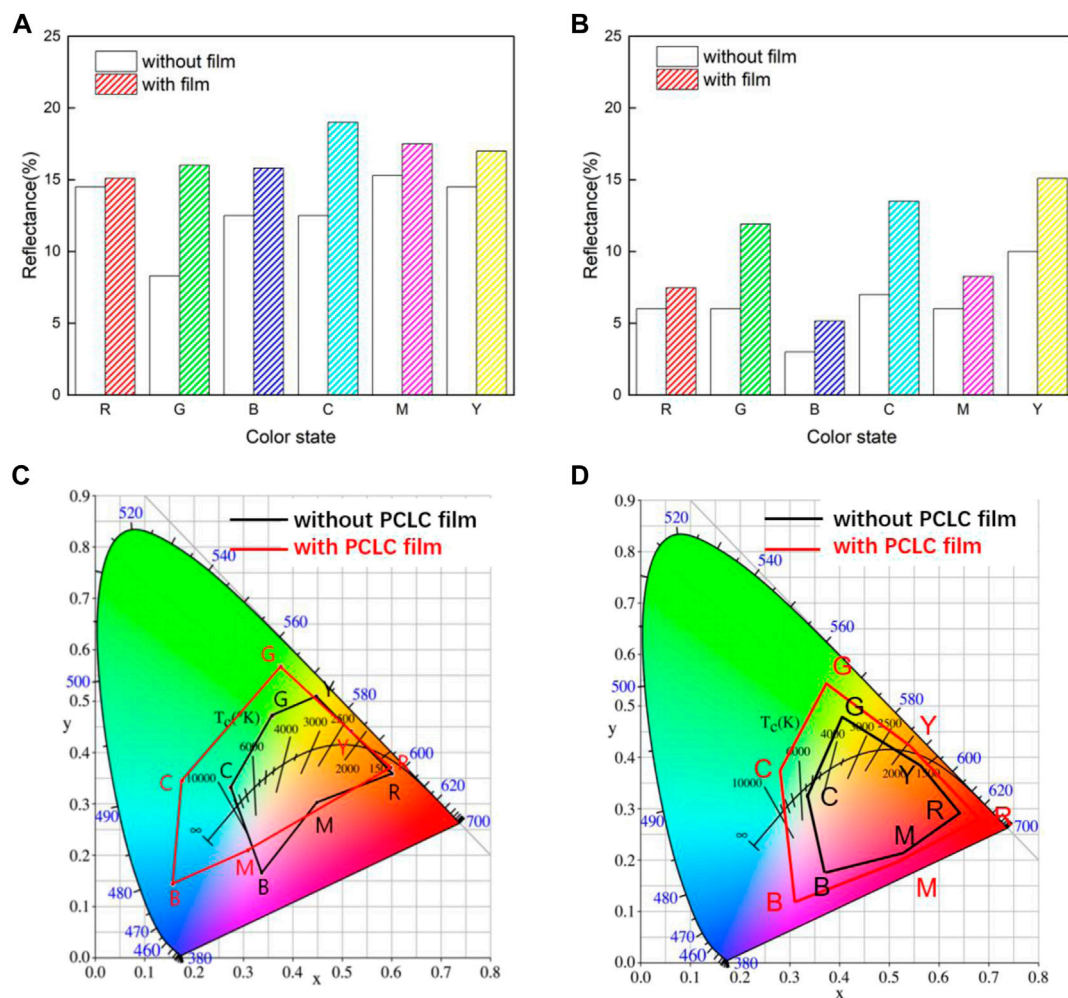


FIGURE 4

Simulation and experimental results of tri-layers full-color EWD device with and without PCLC films: (A) simulation results of reflectivity, (B) experimental results of reflectivity, (C) simulation result of color gamut, (D) experimental result of color gamut.

than 30%, mainly from the increasement of the reflectivity of the blue light and green light. Therefore, by adding a selective reflective layer between the display layers, it is indeed possible to greatly improve the reflectivity of the device by reducing the invalid light loss when light passes through the three layers of the device.

The PCLC films also improves the color gamut of tri-layer EWD device significantly. Without the films, the color gamut of the device is only 32% NTSC in CIE 1931 color space in the simulation and 30% NTSC in the test, which is much lower than the theoretical color gamut that can be achieved through these CMY oils. This can also be attributed to the material absorption caused by the multi-layers structure. Due to the loss of the blue light, the color coordinates of the blue color deviate into to the magenta region. Similarly, due to the loss of the green light, the color coordinates of green color deviate

into yellow region. The low reflectivity of cyan results in color coordinates of cyan color deviate towards the central white region. All these make the color gamut of the device greatly reduced.

With the help of the PCLC films, the EWD device acquires a much wider color gamut up to 60% NTSC in the simulation and 54.1% NTSC in the test, mainly due to the significant increasement in the reflectivity of the blue and green light. It can be inferred that the purity of the color region has also been improved. Moreover, the results also clearly indicate that the green-blue area is much wider. The blue color shifts to the right region and the green color became more distinct, due to the enhanced reflection of the blue and green light. For the cyan, its color coordinates are pulled significantly towards the periphery by the increased reflectivity of blue and green light. For the yellow, magenta and red, the color coordinates are

almost kept unchanged, mainly because the reflectivity of the red is well maintained. Generally, similar trend can be found in both the simulation and experimental results, in spite of slight difference in the shape of the hexagon. This difference mainly exists in the relative position of the magenta, red and blue. In principle, the six corners of the CMY tri-layer EWD device's gamut hexagon should be protruding outward, which matches with the experimental results. However, certain deviation can be identified in the simulation results of the magenta and blue color coordinates, which is attributed to the error in the color coordinates when fitting the CIE with limited number of light bars, the simulation results in the fit CIE.

It can be inferred from the above results that the addition of PCLC films with selective reflection characteristics greatly improves the reflectivity of the blue light and green light, via directly reflecting the blue light and green light without passing through the three layers of EWD devices. Both the reflectivity and the color gamut of the tri-layer EWD device have been significantly improved, which can help to mitigate the problems in the current color EWD display device.

5 Conclusion

We proposed a novel full-color reflective electrowetting display device, consisting of three independent PCLC reflection films that can reflect the red, green and blue circularly polarized light respectively. PCLC films embedded in the device can effectively reduce the reflectance and gamut value. The results of simulation and experiment are in good agreement. It is demonstrated that with the PCLC films, the reflectivity is improved by 20%, while the color gamut is improved by 80%, which is sufficient for the daily display demand of E-paper. The proposed EWD device containing PCLC reflection films provide a new strategy to improve the brightness and color gamut of current EWD device, and is promising for realizing the full-color E-paper display. It is of great significance for the promotion and application of full-color video electro-wetting electronic paper display devices.

Data availability statement

The original contributions presented in the study are included in the article/supplementary material, further inquiries can be directed to the corresponding authors.

Author contributions

All authors contributed to the study conception and design. Conceptualization: XZ and DY; Data curation: BZ, XL and LX; Methodology: XL and HY; Writing-original draft preparation: BZ and XZ; Writing-review and editing: BT and HY; Supervision: Dong Yuan; Funding acquisition: BT and DY.

Funding

This research was funded by National Key R&D Program of China (2021YFB3600602), Science and Technology Program of Guangzhou (Nos. 202201,010351, 2019,050001), Natural Science Foundation of Guangdong Province (Nos. 2020A1515010715, 2021A1515010623), Program for Chang Jiang Scholars and Innovative Research Teams in Universities (No. IRT_17R40), Program for Guangdong Innovative and Entrepreneurial Teams (No. 2019BT02C241). This work also supported by the Guangdong Provincial Key Laboratory of Optical Information Materials and Technology (No. 2017B030301007), Guangzhou Key Laboratory of Electronic Paper Displays Materials and Devices (201705030007) and the 111 Project.

Acknowledgments

We would like to express our thanks to the Science and Technology Program for help identifying collaborators for this work. We also thanks to Guangdong Provincial Key Laboratory of Optical Information Materials and Technology for providing sufficient equipment supplements.

Conflict of interest

The authors declare that the research was conducted in the absence of any commercial or financial relationships that could be construed as a potential conflict of interest.

Publisher's note

All claims expressed in this article are solely those of the authors and do not necessarily represent those of their affiliated organizations, or those of the publisher, the editors and the reviewers. Any product that may be evaluated in this article, or claim that may be made by its manufacturer, is not guaranteed or endorsed by the publisher.

References

- Hayes RA, Feenstra BJ. Video-speed electronic paper based on electrowetting. *Nature* (2003) 425(6956):383–5. doi:10.1038/nature01988
- Feenstra B, Hayes R, Van Dijk R, Boom R, Wagemans M, Giraldo A, et al. (2006). Electrowetting-based displays: bringing microfluidics alive on-screen. in: IEEE International Conference on Micro Electro Mechanical Systems: 22–26 Jan. 2006: Turkey
- Beni G, Hackwood S. Electro-wetting displays. *Appl Phys Lett* (1981) 38(4): 207–9. doi:10.1063/1.92322
- Beni G, Tenan MA. Dynamics of electrowetting displays. *J Appl Phys* (1981) 52(10):6011–5. doi:10.1063/1.329822
- Lippman G. Relations entre les phenomenes electriques et capillaries. *Ann de Chim de Physique* (1875) 5(11):494–549.
- Berge B. Electrocapillarite et mouillage de films isolants par l'eau. *Comptes Rendus De Lacademie Des Sci Paris Serie* (1993) 317(2):157–63.
- Mugele F, Baret J-C. Electrowetting: from basics to applications. *J Phys : Condens Matter* (2005) 17(28):705–74. doi:10.1088/0953-8984/17/28/r01
- Grilli S, Miccio L, Vespini V, Finizio A, De Nicola S, Ferraro P. Liquid micro-lens array activated by selective electrowetting on lithium niobate substrates. *Opt Express* (2008) 16(11):8084–93. doi:10.1364/oe.16.008084
- Mark D, Haeberle S, Roth G, von Stetten F, Zengerle R. Microfluidic lab-on-a-chip platforms: requirements, characteristics and applications. *Chem Soc Rev* (2010) 39(3):1153–82. doi:10.1039/b820557b
- Sur A, Lu Y, Pascente C, Ruchhoeft P, Liu D. Pool boiling heat transfer enhancement with electrowetting. *Int J Heat Mass Transfer* (2018) 120:202–17. doi:10.1016/j.jheatmasstransfer.2017.12.029
- Krupenkin T, Taylor JA. Reverse electrowetting as a new approach to high-power energy harvesting. *Nat Commun* (2011) 2(1):448. doi:10.1038/ncomms1454
- Wu H, Hayes RA, Li F, Henzen A, Shui L, Zhou G. Influence of fluoropolymer surface wettability on electrowetting display performance. *Displays* (2018) 53: 47–53. doi:10.1016/j.displa.2018.02.002
- Dou Y, Tang B, Groenewold J, Li F, Yue Q, Zhou R, et al. Oil motion control by an extra pinning structure in electro-fluidic display. *Sensors* (2018) 18(4):1114. doi:10.3390/s18041114
- Zhou R, Ye Q, Li H, Jiang H, Tang B, Zhou G. Experimental study on the reliability of water/fluoropolymer/ITO contact in electrowetting displays. *Results Phys* (2019) 12:1991–8. doi:10.1016/j.rinp.2019.02.037
- Dou Y, Chen L, Li H, Tang B, Henzen A, Zhou G. Photolithography fabricated spacer arrays offering mechanical strengthening and oil motion control in electrowetting displays. *Sensors* (2020) 20(2):494. doi:10.3390/s20020494
- Kuo SW, Chang YP, Cheng WY, Lo KL, Lee DW, Lee HH, et al. 34.3: Novel development of multi-color electrowetting display. *SID symposium. Dig Tech Pap* (2010) 40(1):483–6.
- Giraldo A, Aubert J, Bergeron N, Li F, Mvd W, Massard R, et al. 34.2: Transmissive electrowetting-based displays for portable MultiMedia devices. *J Soc Inf Disp* (2010) 18(4):317–25. doi:10.1889/jsid18.4.317
- You H, Steckl A. Three-color electrowetting display device for electronic paper. *Appl Phys Lett* (2010) 97(2):023514. doi:10.1063/1.3464963
- Wei-Yuan L, Cheng W, Yung-Hsiang C, Liang C-C. A stacking color electrowetting display for the smart window application. *SID Int Symp Dig Tech Pap* (2011) 42(1):78–81. doi:10.1889/1.3621448
- Yang G, Tang B, Yuan D, Henzen A, Zhou G. Scalable fabrication and testing processes for three-layer multi-color segmented electrowetting display. *Micromachines* (2019) 10(5):341. doi:10.3390/mi10050341



OPEN ACCESS

EDITED BY

Qiang Xu,
Nanyang Technological University,
Singapore

REVIEWED BY

Huilong Liu,
Guangdong University of Technology,
China
Bin Liu,
Sun Yat-sen University, China

*CORRESPONDENCE

Rui Zhou,
zhourei@m.scnu.edu.cn

SPECIALTY SECTION

This article was submitted to Optics and
Photonics,
a section of the journal
Frontiers in Physics

RECEIVED 22 August 2022

ACCEPTED 27 September 2022

PUBLISHED 11 October 2022

CITATION

Jiang H, Qian R, Chen W, Zhou R and
Zhou G (2022), Filling model of oil and
polar liquid for electrowetting displays
based on phase change.
Front. Phys. 10:1024775.
doi: 10.3389/fphy.2022.1024775

COPYRIGHT

© 2022 Jiang, Qian, Chen, Zhou and
Zhou. This is an open-access article
distributed under the terms of the
[Creative Commons Attribution License](https://creativecommons.org/licenses/by/4.0/)
(CC BY). The use, distribution or
reproduction in other forums is
permitted, provided the original
author(s) and the copyright owner(s) are
credited and that the original
publication in this journal is cited, in
accordance with accepted academic
practice. No use, distribution or
reproduction is permitted which does
not comply with these terms.

Filling model of oil and polar liquid for electrowetting displays based on phase change

Hongwei Jiang¹, Rongzhen Qian¹, Wenwen Chen¹, Rui Zhou^{1*}
and Guofu Zhou^{1,2}

¹Guangdong Provincial Key Laboratory of Optical Information Materials and Technology & Institute of Electronic Paper Displays, South China Academy of Advanced Optoelectronics, South China Normal University, Guangzhou, China, ²Academy of Shenzhen Guohua Optoelectronics, Shenzhen, China

Reflective displays have recently attracted more and more attention because of the advantages of low power consumption and eye protection. Among them, electrowetting display (EWD) is the most potential reflective display technology due to its full color and video speed advantages. However, filling models of oil and polar liquids in EWD fabrication were rarely reported. In this paper, a phase change filling model was proposed, and its related equipment was designed and manufactured. The efficiency of phase change filling model has a significant advantage compared to conventional filling models, which can finish the whole process of filling and coupling for 400*500 mm panel within 270 s while the efficiency of other filling models is over 10 min. Since the process of oil filled into the pixels was released into the air environment, the dosing method was significantly enriched, and dosing accuracy was more controllable. The experimental results showed that, a good response time and a high pixel aperture ratio of 31.78 ms and 68.2% can be obtained, respectively.

KEYWORDS

electrowetting display, colored oil, polar liquid, phase change, filling

Introduction

E-paper displays have received widespread attention due to their advantages of lower power consumption and sunlight readability [1–4]. On this basis, the electrowetting display (EWD) has the characteristics of full color and video speed response, which make it become the most potential reflective display technology in the future [5–10]. In 2003, Robert A. Hayes first proposed the typical structure of EWD and published it in Nature [11]. Subsequently, the research activities of EWD won rapid development, more and more universities and research institutes worldwide joined this field.

A typical EWD device mainly includes top and bottom electrodes, a hydrophobic layer, pixel walls mounted on a bottom electrode, mutually incompatible colored oil and transparent polar liquids. The transparent polar liquid plays a role in changing wettability on solid surfaces and pushing oil to spread or shrink, corresponding to a single pixel “on” or “off”. The colored oil plays dual roles of the grayscale switching and color demonstration, which make it the core material in EWDs [12–15].

Therefore, the precise filling of colored oil and polar liquid in EWDs determines its optical performance. Chasing the efficient and uniform filling of colored oil, various filling models have been studied in the EWDs fabrication. The University of Cincinnati started research in EWDs filed since 2005 [16] and proposed an oil filling model based on the interface self-assembly in 2007 [17], which used the advantage of wettability difference between oil and polar liquid on the surface of pixel wall. The speed of this filling model was restricted by the oil spreading rate, which was typically 1 mm/s. So the efficiency of this model was over 10 min for a 400*500 mm panel. Filling results were susceptible to oil-polar liquid interface disturbance and substrate immersion speed. Based on Cincinnati's work, Liquivista proposed a self-assembly filling concept of dosing oil at the three-phase contact line when the polar liquid level rose and intersected with the substrate [18], which reduced oil residue and consumption. However, it failed to overcome the bottleneck of efficiency and accuracy problems of the filling process. In addition, to avoid trapping bubbles in pixels, Liquivista also invented a method for filling oil with a unique bubble-liquid separation structure [19, 20]. The core of the method is to control the ratio of oil to air bubbles in the cavity to achieve the removal of air bubbles trapped in the pixel. This technology has very high requirements for the consistency of filling gap and the precise controllability of oil/bubbles, and the filling efficiency is extremely low. National Chiao Tung University in Chinese Taipei [21] and Advanced Display Technology Co., Ltd. (ADT) in Germany (ADT) [22] made a beneficial attempt to fill oil based on inkjet printing technology, which could achieve an excellent filling consequence for larger pixels. However, the design and manufacture of high-density inkjet printing nozzles and precise oil supply systems are still enormous challenges for the pico-level filling accuracy demand. Recently, Wen Chenyu et al. [23] of Nanjing University reported a capillary-based oil filling model which was similar to the vacuum filling of liquid crystals in the LCD fabrication process. However, it required that the distance between the top and bottom substrates was bigger than 300 μm , which was not conducive to the sealing and mechanical stability of the panel. Considering the risk of residual oil in corners and the gap of display devices, the actual filling effect was not as well as the simulation result.

In this paper, a novel filling model was proposed to achieve filling of oil and polar liquid in sequence, which utilized the differences in freezing points of oil and polar liquid. It creatively solved the limitation that oil always was filled in the polar liquid surroundings. The polar liquid was dosed with one big droplet on the frozen oil surface, then the top and bottom substrates were aligned and coupled. The proposed filling model improved the fabrication efficiency and had a good controllability of oil and polar liquid amount.

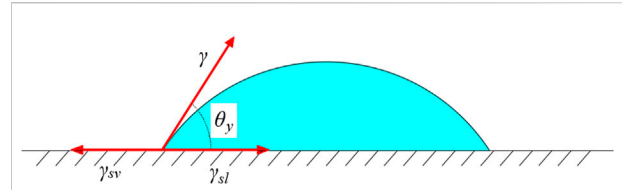


FIGURE 1
Force balance at the droplet contact line.

Principle

Basic principle of electrowetting

Electrowetting (EW) refers to manipulating the movement of a small amount of liquid on solid surfaces by adjusting the surface wettability using electric fields [24, 25]. For a liquid drop in the ambient vapor of a general liquid-vapor system, the angle between the liquid-vapor interface and the solid-liquid interface is known as the contact angle of the liquid. This angle is typically denoted as Young's angle θ_y . The relationship between θ_y and the three interfacial (solid-liquid, solid-vapor, and liquid-vapor) tensions is described by the Young-Dupré Equation as shown in Eq. 1:

$$\cos \theta_y = (\gamma_{sv} - \gamma_{sl})/\gamma \quad (1)$$

Where the droplet phase is marked by "l", the ambient medium by "v", and the electrode is a solid "s". For convenience, "v" is used no matter whether the ambient medium is actually a vapor phase or another condensed immiscible dielectric, such as oil. And for EWOD (electrowetting-on-dielectric), "s" is represented the entire substrate. γ_{sl} , γ_{sv} , and γ are the solid-liquid, solid-vapor, and liquid-vapor interfacial tension, respectively. Details are shown in Figure 1.

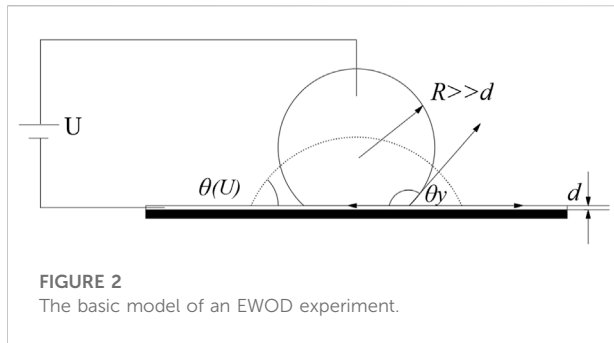
It is assumed that the electrolyte is completely uniform at zero voltage up to the interface. Then, upon applying a potential ϕ_d at the solid surface, the variation of the interfacial energy is given by Eq. 2. Where σ is the charge density in the diffuse layer.

$$\gamma(\phi_d) = \gamma - \int_0^{\phi_d} \sigma(\phi) d\phi \quad (2)$$

For the diffuse layer charge, there will be Eq. 3

$$\gamma(\phi_d) \approx \gamma - \frac{\epsilon \epsilon_0}{2\lambda_D} \phi_d^2 \quad (3)$$

Where λ_D is the thickness of the electric double layer (EDL), ϵ and ϵ_0 are the dielectric constant of the solid and vacuum dielectric constant, respectively. Eq. 3 shows that the interfacial tension of the electrode-electrolyte interface decreases with the increase of the potential difference by applying a voltage. Tensions of other interfaces are not



affected because there is no substantial potential drop across them. Then, the voltage-dependent contact angle can be calculated by inserting Eq. 2 into Young's law, which is shown in Eq. 4.

$$\cos \theta(U) = \frac{\gamma_{sv} - \gamma_{sl}(U)}{\gamma} = \cos \theta_y + \frac{1}{\gamma} \int_0^U \sigma(\phi) d\phi \quad (4)$$

Simply, the applied voltage U is equivalent to the potential difference ϕ_d across the diffuse layer. Eq. 4 can be rewritten as Eq. 5.

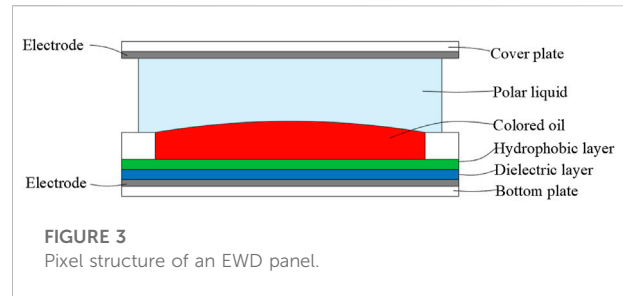
$$\cos \theta(U) = \cos \theta_y + \frac{\epsilon \epsilon_0}{2\lambda_D \gamma} U^2 \quad (5)$$

Eq. 5 is often known as Young-Lippmann (YL) equation. It is a critical equation that relates the electrostatic energy to the wettability. All above is the theory about EW without the dielectric. As for EWOD, the relevant energy is the electrostatic energy in the macroscopic capacitor rather than the free energy of the EDL. The macroscopic capacitor is formed among the liquid, the electrode and the dielectric layer.

Principle of electrowetting device

In the mid-1990s, Bruno Berge and his colleagues [26] promoted the idea of introducing hydrophobic polymer films as insulators between an electrode on the substrate and the fluid. In EW applications, a dielectric coating on the electrode is almost exclusively involved. The aim is to insulate the conductive fluid from the electrode and thereby prevent chemical reactions. This layer contributes to the robustness and reliability of EW. This general structure is shown in Figure 2 and it is often denoted as EWOD to emphasize the presence of the dielectric coating. Where d is the thickness of the dielectric coating layer and R is the drop size of the droplet.

The variation of the macroscopic contact angle in an EWOD before contact angle saturation is described by the Young-Lippmann equation, which is shown in Eq. 6.



$$\cos \theta(U) = \cos \theta_y + \frac{\epsilon \epsilon_0}{2d\gamma} U^2 \quad (6)$$

Eq. 6 is similar to Eq. 5, except that d replaces the thickness of EDL. This leads to the differences between EW without dielectric and EWOD. For EWOD, the ratio in the right part of Eq. 6 is typically four to six orders of magnitude smaller than that in Eq. 5, depending on the properties of the dielectric coating layer. Consequently, the voltage required to achieve a substantial contact angle decrease in EWOD is much higher, which is more suitable for actual applications.

Generally, an essential EWD device is composed of two parallel plates functioning as top/bottom electrodes, polar liquid and a second immiscible colored oil, as shown in Figure 3. The bottom substrate is layered with a conductive layer such as indium tin oxide (ITO), a dielectric layer, and a hydrophobic layer (like Teflon and Cytop). The hydrophobic layer enhances the change in contact angle with electrical actuation and prevents the droplet from sticking. When a certain voltage is applied to the system, the interfacial tension between the polar liquid and the surface of the bottom substrate will be changed.

Device fabrication

Preparation of top and bottom substrates

A patterned ITO panel and TFT-array panel could be selected as the bottom plate, and a non-patterned ITO panel was used for the top plate. The patterned ITO and non-patterned ITO glasses used in this experiment were ordered from Wuhu Token Technology, the thickness of the ITO layer was around 25 nm, and the square resistance was 70–90 Ω/cm^2 . The bottom substrate was composed of a dielectric layer, a hydrophobic layer, and a pixel wall structure. The top substrate had photo-spacers mounted on the ITO surface to control the gap between the top and bottom substrates. The detailed process is shown in Figure 4.

First, the top and bottom plates needed to be cleaned to remove particles and organic contaminants. The dielectric layer was a patterned layer mounted on electrodes and was realized by photolithography. A negative photoresist for dielectric layer was

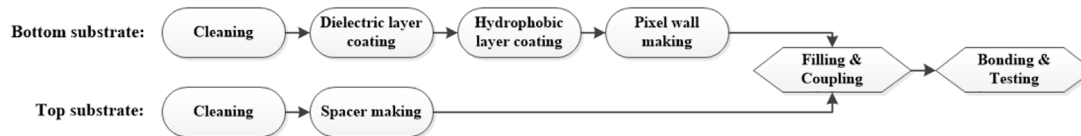


FIGURE 4

Fabrication process of an EWD device.

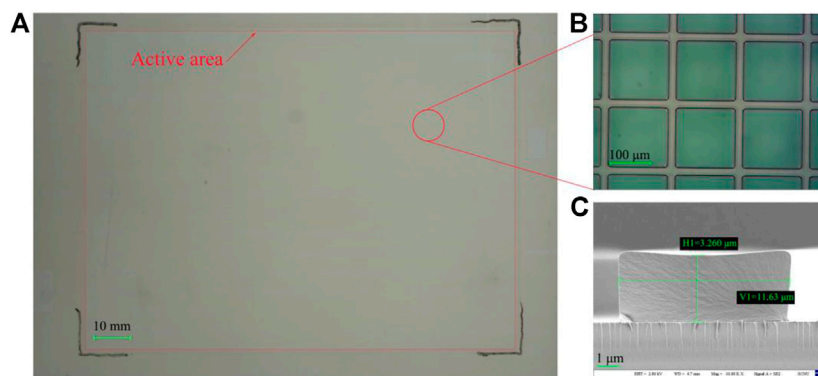


FIGURE 5

The as-prepared bottom substrate. (A) macro photo of bottom substrate was taken by a crammer, and (B) the pixel wall structure was taken under the microscope, the pixel size was $184 \times 184 \mu\text{m}$. (C) Morphology of the pixel wall under the SEM, Pixel wall width was $11.63 \mu\text{m}$ and height was $3.26 \mu\text{m}$, with SEM parameters of EHT = 2.00 KV, WD = 4.7 mm, Mag = 10.00 K X (magnification was 10.00K times), Signal A = SE2.

spin-coated (KW-4A, Institute of Microelectronics, Chinese Academy of Science, China) on the ITO glass surface at 1500 r/min for 1 min and pre-baked (EH20B Lab Tech, China) at 110°C for 1.5 min. Then through exposure ((URE-2000/35, Institute of Optics and Electronics, Chinese Academy of Science) with $30 \text{ mJ}/\text{cm}^2$, post-exposure baking at 110°C for 90 s, development in 238D solution for 90 s, and post-curing at 230°C for 30 min to obtain a $1 \mu\text{m}$ dielectric layer structure. The hydrophobic layer was obtained by one-step screen printing (HD-3050, Dongguan, China). The selected material was DuPont AF1600 solution, the film thickness was 800 nm, and the film thickness uniformity deviation was less than $\pm 5\%$. Due to the hydrophobicity of AF1600, a plasma treatment on hydrophobic layer was carried out to make the following photoresist coating possible. A negative photoresist for pixel wall was coated on the hydrophobic layer by the same spin coater and pre-baked at 110°C for 1.5 min. Then through exposure ($80 \text{ mJ}/\text{cm}^2$), post-exposure baking (110°C , 90 s), development (0.4% KOH, 90 s), and post-curing (185°C , 30 min) to obtain the pixel wall, whose height was $3 \mu\text{m}$ and line width was $11 \mu\text{m}$. Above that, photoresist for dielectric layer and pixel wall were all purchased from Weifang Suintific Technology, and the models were HN-022N and HN-008N,

respectively. Structures on the bottom substrate are shown in Figure 5.

Compared with bottom substrate, the structure on the top substrate was much simpler. There were only photo-spacers, which were realized by photolithography. A negative photoresist was spin-coated on the non-patterned ITO glass surface at 700 r/min for 90 s and pre-baked at 120°C for 8 min. Then through exposure ($1500 \text{ mJ}/\text{cm}^2$), post-exposure baking (120°C , 8 min), development (25°C , 2.38% TMAH, 5 min), and post-curing (185°C , 30 min) to obtain spacers, whose height was around $40 \mu\text{m}$ and diameter was about $30 \mu\text{m}$. The photoresist for photo spacers was purchased from Weifang Suintific Technology, and the models was HN-1903. The spacer shape is shown in Figure 6.

Phase change filling and coupling

In an EWD device, both colored oil and polar liquid are critical to display performance, such as grayscale, contrast, brightness, aperture ratio, response time, etc. Therefore, precisely filling of oil and polar liquid can determine the performance of EWDs.

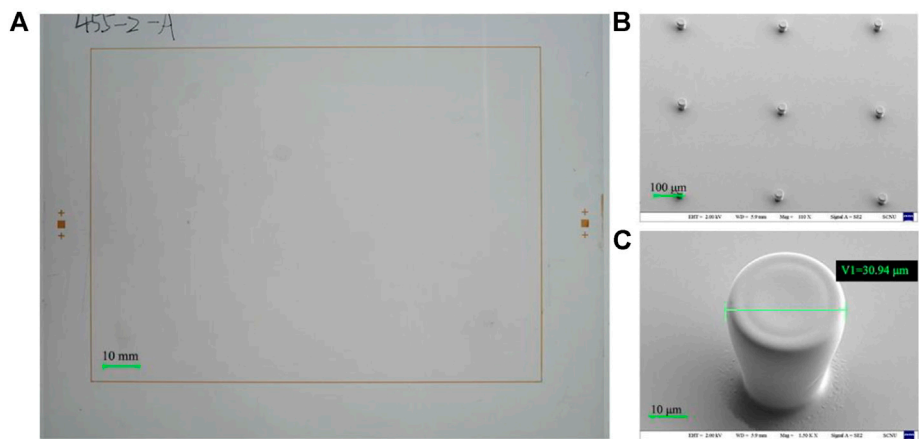


FIGURE 6
The as-prepared top substrate. (A) macro photo of top substrate was taken by a crammer, and (B) the spacer was taken under SEM with the parameters of EHT = 2.00 KV, WD = 5.9 mm, Mag = 110 X, Signal A = SE2. (C) Morphology of a single spacer under the SEM, Pixel wall width was 11.63 μm and height was 3.26 μm, with SEM parameters of EHT = 2.00 KV, WD = 5.9 mm, Mag = 1.50 K X, Signal A = SE2.

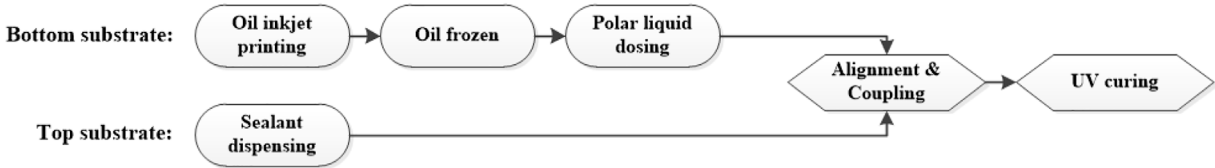


FIGURE 7
Flow chart of phase change filling and coupling.

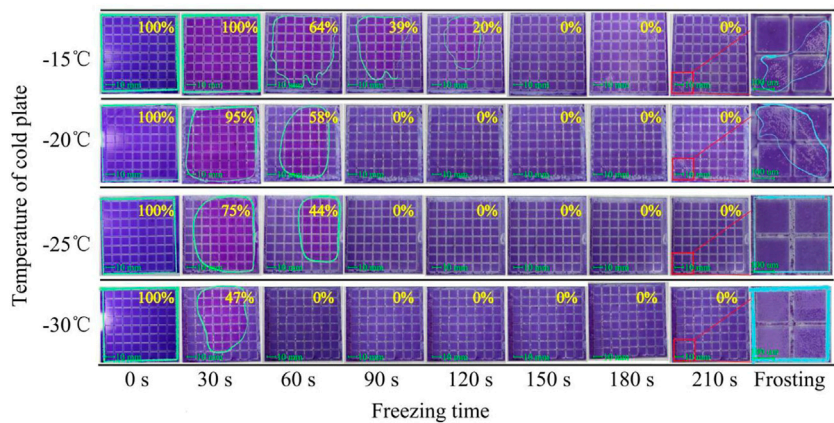


FIGURE 8
Proportions of unphase-changed oil at different temperatures and freezing times.

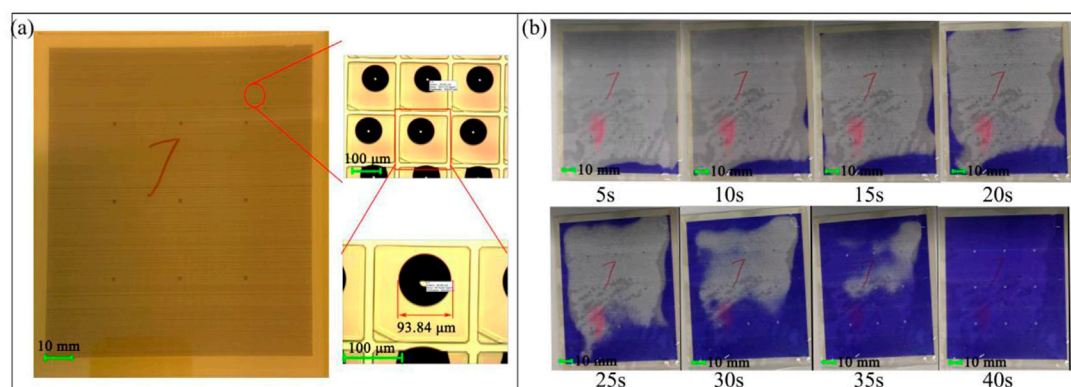


FIGURE 9

(A) Oil filled stage in bottom substrate. Each pixel contained 25 droplets of oil, and the diameter of oil was 93.84 μm . (B) Unfrozen process of solid oil at room temperature.

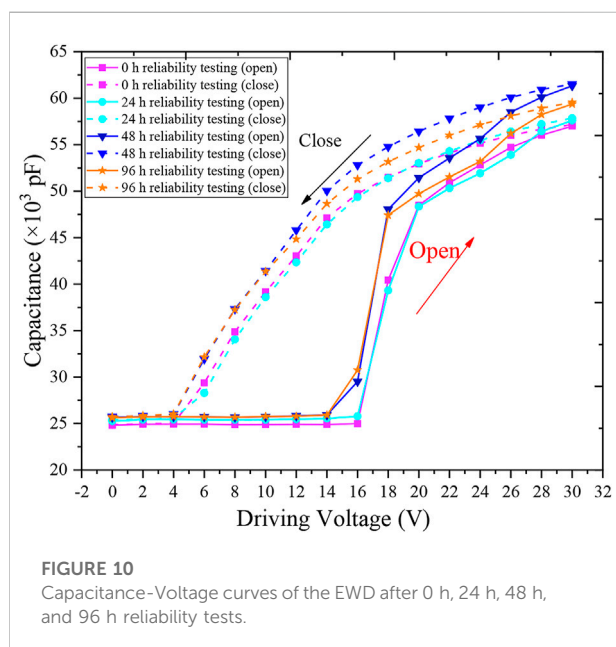


FIGURE 10

Capacitance-Voltage curves of the EWD after 0 h, 24 h, 48 h, and 96 h reliability tests.

In this work, colored oil was printed into pixels by an inkjet printer (PiXDRO TPI IP410, Meyer Burger, Netherlands), and frozen on a cold plate which could reach -40°C . Dodecane was selected as the solvent for oil and the freezing point was about -9.6°C so that oil phase could be frozen very fast. The polar liquid was dripped *via* a dispenser, and its temperature was always controlled under -20°C to prevent melting of the frozen oil phase. The polar liquid was a 1:1 mixed solution of glycerol and ethylene glycol, and the freezing point was around -35°C to ensure that the liquid state could still be maintained in a low-temperature environment. For top substrate, the sealing material was prepared as a box pattern on glass surface by a dispenser,

where the sealing material was UV-curable acrylic resin. Finally, the top and bottom substrates were aligned and bonded together, and the device fabrication was completed along with a UV curing process. The detailed procedure can be seen in Figure 7.

Results and Discussion

Phase change of the colored oil

Since the freezing point of colored oil is -9.6°C , any cooling temperature below -10°C can make the oil phase solid. So various freezing temperatures and freezing times were selected for experimental, as shown in Figure 8. To facilitate the operation, oil was directly coated on the surface of bottom substrates by slit coating.

It can be seen in Figure 8 that there were four temperatures selected for the freezing experiment, which were -15°C , -20°C , -25°C , and -30°C , respectively. The freezing time was from 0 s to 210 s with a step increase of 30 s. When the freezing temperature was -15°C , the oil at the edge of panel began to solidify within 60 s, the color of the solidified oil became lighter. And 64% of unphase-changed oil remained at 60 s as shown in the blue circle. Finally, it took 150 s to complete the phase change of all the oil. When the freezing temperature was reduced to -20°C and -25°C , the oil began to solidify within 30 s and took 90 s to complete the phase change process. The phase change speed at -25°C was a little faster than -20°C , which means the unphase-changed oil at -25°C was less than -20°C within 60 s freezing time as shown in blue circle. When the freezing temperature further decreased to -30°C , it only took 60 s to solidify all the oil. As the freezing temperature decreased, the problem of condensed water would gradually appear. When the temperature was below -30°C , the frosting problem would be so serious that the whole segments were fully covered by frost (as shown in column of frosting defect in

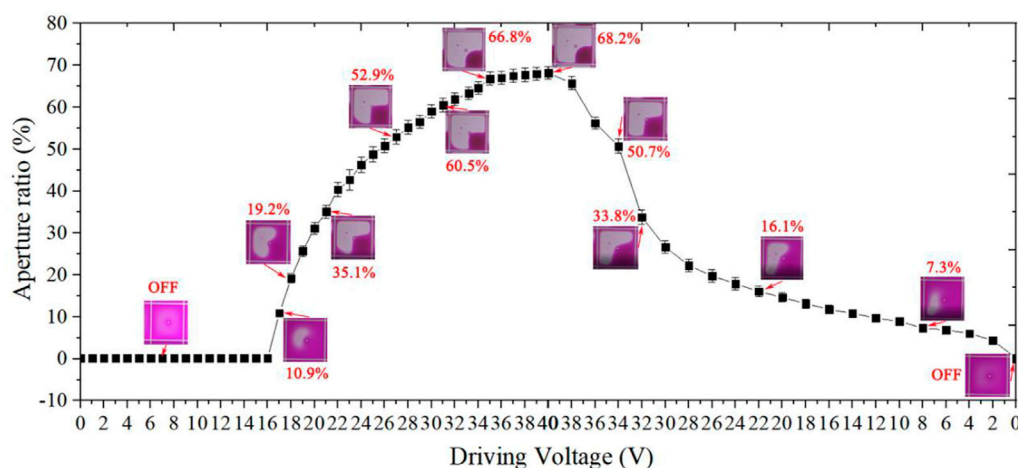


FIGURE 11

Pixel aperture ratio values with different driving voltages.

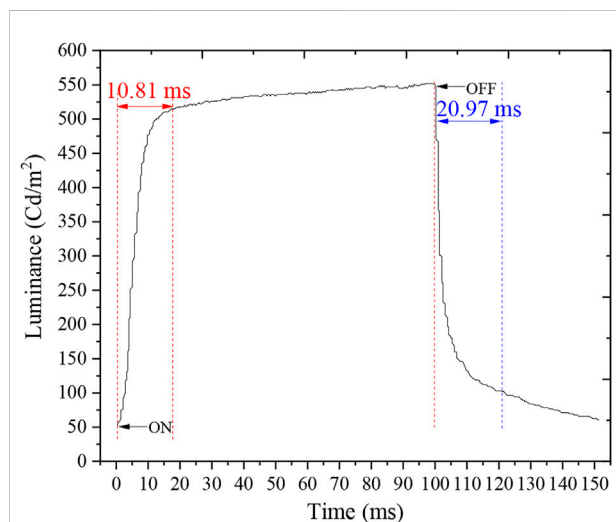


FIGURE 12

Response time at a driving voltage of 30 V.

Figure 8). Thus, it was more appropriate to select the temperature above -20°C as the freezing temperature.

Unfrozen of the solid oil phase

Inkjet printing provides a reliable filling model which precisely controls the volume of oil filled in each pixel. In this work, 25 oil droplets of 10 pL were printed in single pixel. Since the interfacial energy of oil in air was not enough to wet the surface of the hydrophobic layer, the oil droplet formed a shape of a sizeable shrinking droplet in the middle of the pixel, as shown in Figure 9A,

the diameter was about $46.92\text{ }\mu\text{m}$. During the unfrozen process, oil droplets would spread in the pixels. This was also a good indication of when the oil unfrozen process was complete, as shown in Figure 9B, the unfrozen time was 40 s.

As the panel temperature gradually increased, the edge area began to melt at 5 s, and as time went on, the melted area and melting speed also steadily increased. When the unfrozen time exceeded 20 s, the melted area rose rapidly, and nearly 80% of the melted area was completed in the following 20 s.

Performance of EWDs

An entire EWD can be equivalent to a complex series shunt capacitors. Oil movement can cause a change of capacitance values under driving. The contact angle related to the capacitance has been reported in Verheijen and Prins's work [27]. In the "off" state, the pixel capacitance was primarily determined by oil film thickness and it was typically small. In the "on" state, where the capacitance was primarily determined by the thickness of the fluoropolymer insulator ($0.5\text{--}0.8\text{ }\mu\text{m}$), the capacitance increased significantly. Capacitance changes depended on the size of the area from which the oil has been removed (the so-called "aperture ratio"). Because the brightness of EWDs was proportional to the pixel capacitance, the device's performance could be measured through the capacitance value. The EWD was driven and measured by an impedance analyzer (WK6500B, United Kingdom). The Capacitance-Voltage (C-V) data was shown in Figure 10, the capacitance value did not change until the driving voltage reached 16 V. Then the capacitance increased significantly as the voltage increased. It could be known that 16 V was the device's threshold voltage, at which oil film began to rupture and shrink. During the closing process, the capacitance decreased as the voltage

decreased, and the “off” voltage was 4 V. The device closing C-V curve determined the performance of the grayscale. It could be seen from Figure 10 that all closing C-V curves were nearly linear and had an “off” voltage of 4 V, so it proved that the device had good grayscale controllability.

Considering that the oil phase would change during phase transition. In order to confirm that there was no damage to the surface of hydrophobic layer, reliability tests of 24 h, 48 h, and 96 h were also carried out. Assuming that the surface of hydrophobic layer was damaged, the device would be broken down and the capacitance value would change. The repeatability of the C-V curve would be lost after the reliability test. It can be seen from Figure 10 that the threshold voltages were always 16 V and the “off” voltages were always 4 V. The C-V curve had good repeatability, so the phase change process did not damage the hydrophobic layer.

As a reflective display, the brightness of EWDs is critical. It depends on the aperture ratio of pixel, so the maximum aperture ratio of a single pixel will determine the display white state and contrast ratio. The pixel switch was visualized and captured by using a high-speed camera (Phantom MiRO M110, Vision Research) integrated with a microscope (CKX41, Olympus). The pixel remained “off” state until the driving voltage reached 16 V, which was consistent with the C-V curve shown in Figure 10. When the driving voltage was 18 V, the aperture ratio was 10.9%. Then the aperture ratio of pixels increased rapidly as the voltage increased and reached an aperture ratio of 68.2% at 40 V as shown in Figure 11.

Response time is an essential indicator of the EWD. The brightness of the EWD is measured by a colorimeter (Admesy-arges45). The time required to reach 90% of the maximum brightness was calculated as the “on” time (t_{on}). The time required to drop the “off” state was the turn-off time (t_{off}). As shown in Figure 12, t_{on} was 10.81 ms, t_{off} was 20.97 ms while for the Liquevasta filling method reference opening time and closing time were 12 ms and 13 ms, respectively [11]. The response time was 31.78 ms which could realize a 30 fps video play.

Conclusion

In this paper, an EWD based on phase change filling model was proposed. The functional testing proved that the EWD device prepared by this method had good optical performance and video-speed response time. Oil was filled into pixels by inkjet printing to precisely control the amount. The oil’s low-temperature phase change and the separate drip of polar liquid significantly improve fabrication efficiency and controllability. The phase change filling model of oil had good regularity at different temperatures, which provided a theoretical basis for calculation of the filling efficiency. Therefore, this method brings a valuable tool for the industrialization of EWDs.

Data availability statement

The original contributions presented in the study are included in the article/Supplementary Material, further inquiries can be directed to the corresponding author.

Author contributions

HJ contributed to the conception of the study and manuscript preparation; RQ performed the experiment; WC contributed significantly to analysis; RZ made important amendments to the paper; GZ helped perform the analysis with constructive discussions, and approved the final paper to be published.

Funding

This work was supported by National Key R&D Program of China (2021YFB3600601), National Natural Science Foundation of China (No. 22008156), Guangdong Basic and Applied Basic Research Foundation (No. 2021A1515011768), Science and Technology Program of Guangzhou (No. 2019050001, No. 201904020007), Program for Guangdong Innovative and Entrepreneurial Teams (No. 2019BT02C241), Program for Chang Jiang Scholars and Innovative Research Teams in Universities (No. IRT_17R40), Guangdong Provincial Key Laboratory of Optical Information Materials and Technology (Grant No. 2017B030301007), Guangzhou Key Laboratory of Electronic Paper Displays Materials and Devices (201705030007), MOE International Laboratory for Optical Information Technologies and the 111 Project.

Conflict of interest

The authors declare that the research was conducted in the absence of any commercial or financial relationships that could be construed as a potential conflict of interest.

Publisher’s note

All claims expressed in this article are solely those of the authors and do not necessarily represent those of their affiliated organizations, or those of the publisher, the editors and the reviewers. Any product that may be evaluated in this article, or claim that may be made by its manufacturer, is not guaranteed or endorsed by the publisher.

Supplementary material

The Supplementary Material for this article can be found online at: <https://www.frontiersin.org/articles/10.3389/fphy.2022.1024775/full#supplementary-material>

References

- Comiskey B, Albert JD, Yoshizawa H, Jacobson J. An electrophoretic ink for all-printed reflective electronic displays. *Nature* (1998) 394(6690):253–5. doi:10.1038/28349
- Heikenfeld J, Smith N, Dhindsa M, Zhou K, Kilaru M, Hou L, et al. Recent progress in arrayed electrowetting Optics. *Opt Photon News* (2009) 20(1):20. doi:10.1364/OPN.20.1.000020
- Heikenfeld J, Zhou K, Kreit E, Raj B, Yang S, Sun B, et al. Electrofluidic displays using Young–Laplace transposition of brilliant pigment dispersions. *Nat Photon* (2009) 3(5):292–6. doi:10.1038/nphoton.2009.68
- Heikenfeld J, Steckl A. Demonstration of fluorescent RGB electrowetting devices for light wave coupling displays. *J Display Tech* (2004) 5, 302–5.
- Yi Z, Zeng W, Ma S, Feng H, Shen S. Design of driving waveform based on a damping oscillation for optimizing red saturation in three-color electrophoretic displays. *Micromachines* (2022) 12(2):162. doi:10.3390/mi12020162
- Kao WC, Tsai JC. Driving method of three-particle electrophoretic displays. *IEEE Trans Electron Devices* (2018) 3(65):1023–8. doi:10.1109/TED.2018.2791541
- Wang L, Yi Z, Jin M, Shui L, Zhou G. Improvement of video playback performance of electrophoretic displays by optimized waveforms with shortened refresh time. *Displays* (2017) 49:95–100. doi:10.1016/j.displa.2017.07.007
- He W, Yi Z, Shen S, Huang Z, Liu L, Zhang T, et al. Driving waveform design of electrophoretic display based on optimized particle activation for a rapid response speed. *Micromachines* (2020) 11(5):498. doi:10.3390/mi11050498
- Yi Z, Bai P, Wang L, Zhang X, Zhou G. An electrophoretic display driving waveform based on improvement of activation pattern. *J Cent South Univ* (2014) 21(8):3133–7. doi:10.1007/s11771-014-2285-9
- Shen S, Gong Y, Jin M, Yan Z, Xu C, Yi Z, et al. Improving electrophoretic particle motion control in electrophoretic displays by eliminating the fringing effect via driving waveform design. *Micromachines* (2018) 9(4):143. doi:10.3390/mi9040143
- Hayes RA, Feenstra BJ. Video-speed electronic paper based on electrowetting. *Nature* (2003) 425(6956):383–5. doi:10.1038/nature01988
- Chiang Y, Chao Y. Synthesis of dis-azo black dyes for electrowetting displays. *Mater Sci Eng B* (2012) 177(18):1672–7. doi:10.1016/j.mseb.2012.08.011
- Chiang Y, Chao Y. Synthesis and application of oil-soluble red dyes derived from p-n-Alkyl aniline. *Mater Sci Appl* (2014) 5(8):485–90. doi:10.4236/msa.2014.58052
- Lee P, Chiu C, Chang L, Chou P, Lee T, Chang T, et al. Tailoring pigment dispersants with polyisobutylene twin-tail structures for electrowetting display application. *ACS Appl Mater Inter* (2014) 6(16):14345–52. doi:10.1021/am503599k
- Lee P, Chiu C, Lee T, Chang T, Wu M, Cheng W, et al. First fabrication of electrowetting display by using pigment-in-oil driving pixels. *ACS Appl Mater Inter* (2013) 5(13):5914–20. doi:10.1021/am401840b
- Heikenfeld J, Steckl AJ. Intense switchable fluorescence in light wave coupled electrowetting devices. *Appl Phys Lett* (2004) 86(1):011105. doi:10.1063/1.1842853
- Sun B, Zhou K, Lao Y, Heikenfeld J, Cheng W. Scalable fabrication of electrowetting displays with self-assembled oil dosing. *Appl Phys Lett* (2007) 91(1):011106. doi:10.1063/1.2753697
- Schram I, Massard R, Miremont C. *Method of manufacturing an optical display*. US (2011).
- Thomas CA, Babka JP. *Precise fluid dispensing method and device*. US (2010).
- Schmidgall C, Hubertina WWM, Hayes R. *Dispensing method and device for dispensing*. WO (2010).
- Huang YS, Kuo SW, Kuo YS, Chen CY, Lo KL, Cheng WY, et al. Single-layered multi-color electrowetting display by using ink-jet-printing technology and fluid-motion prediction with simulation. *J Soc Inf Disp* (2011) 19(7):488–95. doi:10.1889/JSID19.7.488
- Andriy B, Frank B, Jürgen R, Karlheinz B. Production considerations for bistable droplet driven electrowetting displays. *SID Int Symp Dig Tech Pap* (2012) 43(2):846–9. doi:10.1002/j.2168-0159.2012.tb05918.x
- Wen CY, Ren J, Xia J, Gu T. Self-assembly oil-water perfusion in electrowetting displays. *J Display Technol* (2013) 9(2):122–7. doi:10.1109/JDT.2012.2236641
- Mugele F, Heikenfeld J. *Electrowetting: Fundamental principles and practical applications[M]*. Hoboken, New Jersey, United States: John Wiley & Sons (2018).
- Mugele F, Baret JC. Electrowetting: From basics to applications. *J Phys : Condens Matter* (2005) 17(28):R705–74. doi:10.1088/0953-8984/17/28/R01
- Berge B. Electrocapillarity and wetting of insulator films by water. *Comptes Rendus de l'Academie des Sci - Ser Math* (1993) 317:157–63.
- Verheijen H, Prins M. Contact angles and wetting velocity measured electrically. *Rev Scientific Instr* (1999) 70(9):3668–73. doi:10.1063/1.1149976



OPEN ACCESS

EDITED BY

Qiang Xu,
Nanyang Technological University,
Singapore

REVIEWED BY

Enguo Chen,
Fuzhou University, China
Lelun Jiang,
Sun Yat-sen University, China

*CORRESPONDENCE

Pengfei Bai,
baipf@scnu.edu.cn

SPECIALTY SECTION

This article was submitted to Optics and Photonics,
a section of the journal
Frontiers in Physics

RECEIVED 31 August 2022

ACCEPTED 26 September 2022

PUBLISHED 12 October 2022

CITATION

Li S, Xu Y, Zhan Z, Liu L and Bai P (2022),
A high integration electrowetting
displays system based on AC
driving model.
Front. Phys. 10:1033076.
doi: 10.3389/fphy.2022.1033076

COPYRIGHT

© 2022 Li, Xu, Zhan, Liu and Bai. This is
an open-access article distributed
under the terms of the [Creative
Commons Attribution License \(CC BY\)](#).
The use, distribution or reproduction in
other forums is permitted, provided the
original author(s) and the copyright
owner(s) are credited and that the
original publication in this journal is
cited, in accordance with accepted
academic practice. No use, distribution
or reproduction is permitted which does
not comply with these terms.

A high integration electrowetting displays system based on AC driving model

Shixiao Li, Yijian Xu, Zhiyu Zhan, Linwei Liu and Pengfei Bai*

Guangdong Provincial Key Laboratory of Optical Information Materials and Technology & Institute of Electronic Paper Displays, South China Academy of Advanced Optoelectronics, South China Normal University, Guangzhou, China

As a representative of new reflective display technology, the electrowetting display (EWD) has been widely accepted for its good advantages in power consumption control and display contrast. Because of charge trapping and contact angle hysteresis, static images cannot be maintained and afterimage phenomenon occurs, respectively. These problems seriously affect the EWDs display effect. In order to improve the video display effect of EWDs, an alternating current (AC) driving model was proposed in this paper. Firstly, a high integration EWDs system was built with Xilinx field programmable gate array (FPGA). Secondly, an asymmetric intermediate frequency (IF) AC driving model was proposed to eliminate the afterimage of the video. Finally, the optimized driving method was applied to the EWDs system to achieve a high-smooth display output. The experimental results showed that the problem of afterimage and the problem of static image preserving display were effectively solved. Compared with the traditional AC driving waveform, the maximum reflected luminance of the proposed method was increased by 14%, and the refresh rate of EWDs could reach 60 Hz.

KEYWORDS

high integration, electrowetting display (EWD), intermediate frequency (IF), asymmetric, alternating current (AC)

1 Introduction

Video information acquisition has become one of the important sources for people's daily life. The emergence of technologies such as liquid crystal displays (LCD), Organic Light-Emitting Diode (OLED), and electrophoretic paper displays (EPD) provides more convenience for information interaction [1–3]. In addition to the size and resolution of display devices, people have higher requirements, and reading comfort is gradually concerned. Because of the reflective display, the electronic paper display has the advantages of paper reading experience and low power consumption and is soon widely used. As a representative of the reflective display, EPD enters people's field of vision in the form of electronic tags, electronic books, electronic notebooks, etc. Currently, the response speed of EPD is still too slow to play video smoothly [4]. The EWD is expected to become a new member of the display family due to its fast response speed, and

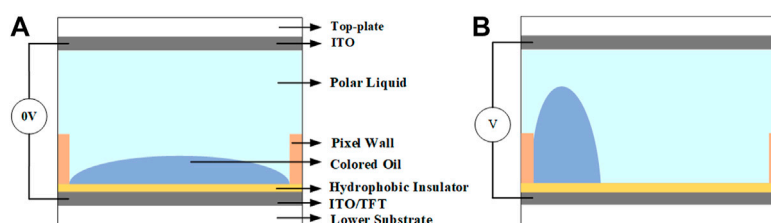


FIGURE 1

Side view of an EWD pixel structure, the pixel is equivalent to an "off" state. (A) Pixel is equivalent to an "off" state. (B) Pixel is equivalent to an "on" state.

paper-like reflective display [5]. As a result, many scholars have paid attention to EWDs for obtaining better paper-like display and video display performance in recent years.

The EWD technology was first proposed in 1981 and successfully applied in 2003 [6, 7]. In recent years, a pulse width modulated (PWM) square wave has been used as the EWDs drive waveform [4]. However, this driving waveform could cause some defects such as contact angle hysteresis [8], oil splitting [9], and charge trapping problems [10]. The contact angle hysteresis problem, which caused the afterimage phenomenon when video playing, had a bad effect on the display performance in EWDs. In order to solve the problem, the alternating current (AC) driving signal was replaced by a direct current (DC) signal [11, 12]. But a symmetrical AC signal could bring about a reduction in the aperture ratio. Therefore, it was very necessary to design a reliable AC driving method. The oil backflow phenomenon occurs when a DC drive signal is continuously supplied due to the charge trapping. The oil backflow could be related to three-phase contact lines formed by oil, water, and hydrophobic insulators [13, 14]. The reset signal was introduced into the AC driving waveform to reduce the oil backflow problem [15, 16]. However, the addition of a reset signal caused a flicker problem in the video display. In order to verify the effectiveness of the EWDs driver in video playback, the design of the video display system was particularly critical. Yang designed a portable EWDs driving system that could display complex images [17]. Qian designed a real-time dynamic display system of electrowetting, which could be connected to computer signals to realize dynamic real-time display in EWDs [18]. However, the system structure was complex, and excessive the system on a chip (SOC) led to an increase in system power consumption. Therefore, it is very important to design an EWDs system with high integration.

This paper made three contributions. Firstly, a highly integrated EWDs system was designed with a high refresh rate, which could be used for the validation study of driving signals. Secondly, an asymmetric intermediate frequency (IF) AC driving method was proposed to solve the problem of afterimage

and maintain images during video playback. Finally, the optimized driving scheme was applied to the EWDs system. Compared with the traditional DC driving model, the asymmetric IF AC driving model had a better driving display capability in terms of the video display.

2 Principles

2.1 Principles of EWDs

Each pixel of EWDs is primarily composed of a top-plate, an indium tin oxide glass (ITO), polar liquid (NaCl solution), colored oil, pixel wall, a hydrophobic insulation layer, a lower substrate, as shown in Figure 1A [19]. An EWD is essentially an optical switch [20, 21]. It changes the wettability of the conducting liquid on the hydrophobic insulating layer by applying a voltage between the top and bottom ITO. When there is no driving voltage, the polar liquid cannot wet the surface, the oil tile on the hydrophobic insulating layer, the pixel is equivalent to an "off" state, as shown in Figure 1A. When the voltage is applied, oil is moved to a pixel corner under the action of electric field force, and the polar liquid will be moved above the hydrophobic layer. The contact angle between the polar liquid and the hydrophobic insulating layer decreases, and the aperture ratio increases. The pixel will show the color of the substrate, and the pixel is equivalent to the "on" state, as shown in Figure 1B. The Young-Lippmann equation is the basic theory of electrowetting technology [22], the relationship between oil contact angle and voltage can be obtained by the Young-Lippmann, as shown in Eq. 1.

$$\cos \theta = \cos \theta_0 + \frac{1}{2} \frac{\epsilon_0 \epsilon_r}{d \gamma_{lg}} V^2 \quad (1)$$

$$V_{bd} = \sqrt{\frac{2(1 - \cos \theta_0) \gamma_{lg}}{\frac{1}{4\pi k} \frac{\epsilon_{oil} S_{oil}}{h} + \frac{\epsilon_r S_{pix}}{d}}} \sim \sqrt{d} \quad (2)$$

Where V denotes the driving voltage, θ is the oil-solid interface contact angle, θ_0 is the equilibrium contact angle between the polar liquid and the hydrophobic insulating layer, d is the thickness of the hydrophobic insulating layer, γ_{lg} indicates interfacial tension between oil and polar liquids. ϵ_0 Indicates vacuum dielectric constant and ϵ_r represents the dielectric constant of the hydrophobic insulating layer, ϵ_{oil} is the dielectric constant of oil, k is the electrostatic constant, h is the thickness of the oil, V_{bd} is the breakdown threshold voltage of the insulating layer, S_{oil} is the area of the oil that shrinks to the corner of the pixel, S_{pix} represents the area of the pixel. It can be seen from Eq. 2 [23], which can adjust the aperture ratio by improving the driving voltage waveform, thereby affecting the breakdown threshold voltage of the insulating layer. It is easy to break through the hydrophobic insulation layer if the voltage is too high, which can cause damage to EWDs pixels [24].

When the porosity increases with the increase of the voltage, the contact angle is called advancing angle. On the contrary, when the aperture ratio decreases as the voltage decreases, the contact angle is called receding angle at the same driving voltage and the difference between the forward and backward angles is the contact angle hysteresis in EWDs [11]. The square waveform is applied during the driving process to keep the aperture ratio, this method can not only shorten the response time but also improved the oil splitting [25]. When the driving voltage increases to a maximum, the oil will be shrunk completely in corners, the aperture ratio cannot be larger. When a constant voltage is applied, the contracted oil cannot be kept in a stable state due to charge trapping, and oil backflow could be caused due to an imbalance between Laplace pressure and Maxwell pressure at the three-phase contact line [26]. The aperture ratio is less affected by oil backflow, the value of aperture ratio can be calculated by Eq. 3.

$$A = \left[1 - \frac{S_{oil}}{S_{pix}} \right] \times 100\% \quad (3)$$

$$\cos \theta = 1 - \frac{C(V - V_T)^2}{2\gamma_{lg}} \quad (4)$$

Where A is the aperture ratio. The effect of oil backflow caused by charge trapping can also be reduced by the reset signal and AC waveform [15, 26]. The relationship between the Lippmann contact angle and the driving voltage can be determined by Eq. 4, [23, 27]. Where V_T is the potential generated by the charge trapping, C is the capacitance of the pixel, the capacitance value of pixel C can be calculated by Eq. 5, [23]. By changing the driving voltage waveform and adjusting the voltage duty ratio, the oil-solid interface contact angle can be controlled, and the gray-scale display of EWDs can be directly affected. As can be seen from Eq. 4, the value range of θ is larger under AC driving waveform than DC driving waveform, the relationship between voltage and θ

with AC drive is worth further study. The relationship between the contact angle and the voltage can also be expressed by the following Eq. 6, γ_{sl} , γ_{sg} represents the surface tension of the solid-liquid, and solid-gas interface respectively [15].

$$C = \frac{1}{4\pi k} \left(\frac{\epsilon_{oil} S_{oil}}{h} + \frac{\epsilon_r S_{pix}}{d} \right) \quad (5)$$

$$\cos \theta = \frac{\gamma_{sg} - \gamma_{sl} + \epsilon_0 \epsilon_r V^2 / 2d}{\gamma_{lg}} \quad (6)$$

2.2 Principles of EWDs driving model

2.2.1 Highly integrated EWDs driving system

As shown in Figure 2, a highly integrated EWDs system needed FPGA to complete signal acquisition and processing, and complete EWDs driving. Firstly, the personal computer (PC) signal was received by the FPGA through the high-definition multimedia interface (HDMI) interface, then the time minimized differential signal (TMDS) was converted into a red-green-blue (RGB) signal, and finally the RGB signal was converted into corresponding driving signals and output to an EWD.

This system realized the conversion of TMDS in FPGA, and could adapt to input signals of any resolution, which provided convenience for EWD. In addition, an adaptive resolution signal output function was added to the system, which could be adapted according to different sizes of EWDs.

A ZYNQ 7010 chip was used by the EWDs system as the control processing chip of the system. This chip integrated a feature-rich dual core ARM based processing system (PS) and a Xilinx programmable logic (PL). As shown in Figure 3, the EWDs system consisted of a power module, a core control module, an EWD, and a base board. The base board had rich interfaces which connected various modules. In addition, there were two HDMI interfaces on the base board, which realized the input and output of HDMI signals. The power module could output +20 V, -20 V, +15 V, -15 V, +5 V, and +3.3 V to provide power for each module. An LCD with a resolution of 800×480 was used as an output device to display the RGB signal converted by the FPGA, which was used as a signal monitor. A single-color EWD with a resolution of 640×480 was used as the testing screen of this system. Because the driving signal had the same effect on EWDs of each color channel, this system chose a single-color EWD as the testing device. The core control module consisted of ZYNQ 7010, flash memory, static random-access memory (SRAM), and low dropout regulator (LDO). As shown in Figure 3, the highly integrated display system consisted of HDMI interfaces, a power module, an LCD, an FPGA module, and an EWD. The data conversion functions and display driver functions were completed on the FPGA.

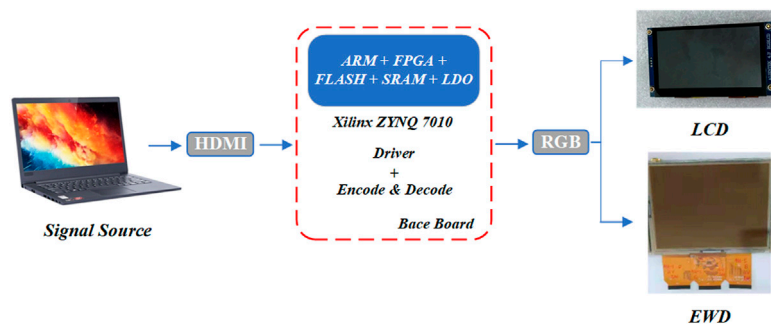


FIGURE 2

Schematic diagram of the driving system for the EWD. HDMI signal is directly converted into RGB signal by the system and output to an LCD and an EWD.

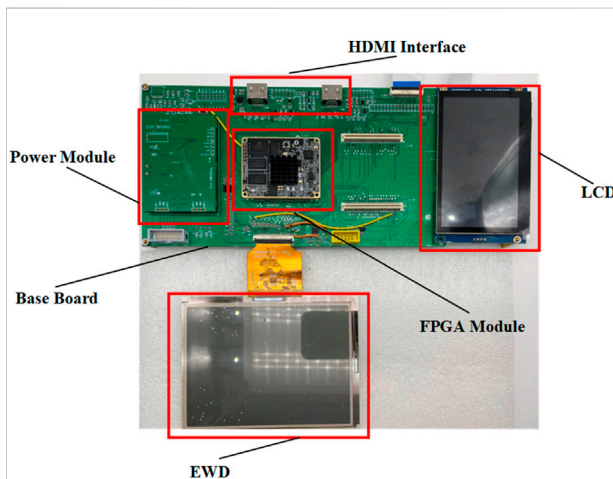


FIGURE 3

A physical figure of the driving system for EWDs.

2.2.1.1 TMDS conversion

The TMDS was converted and decoded using the PL part, and the display function was implemented in the PS part. The TMDS conversion part was mainly composed of a ZYNQ7 processing system module, a video direct memory access (VDMA), a video timing controller (VTC), a stream to video out, and a digital visual interface (DVI) to an RGB video decoder.

The TMDS was converted to a RGB signal for providing data to EWDs. Display functions included a cropping mode and an adaptive resolution mode. As shown in Figure 4, it is an EWD in different display modes. As shown in Figure 4A, this is an EWD in a cropping mode, and Figure 4C is the enlarged detail of Figure 4A. Part of the computer signal is displayed on the EWD. Figure 4B shows an EWD in an adaptive resolution mode, and Figure 4D is the enlarged detail

of Figure 4B, showing the whole content of the computer signal. In the cropping mode, the signal input by PC was directly cropped and displayed. And then, the EWD cropped into an 800×480 image and output to the display module.

Since the EWD and LCD resolutions were inconsistent, the display signal needed to be further converted to synchronize the display. In the case of 800×480 resolution, the image signal was further cropped to 640×480 resolution and output to the EWD. The LCD directly received signals with a resolution of 800×480 . The EWD refresh rate was 60 Hz in cropping mode, and the EWD refresh rate was 30 Hz in adaptive resolution mode, which was determined by the input source refresh rate and the driver chip.

The adaptive resolution method was calculated by PS, the maximum input resolution was $1920 \times 1,080$, and the output minimum resolution was 480×272 . In this experiment, the input resolution was $1,280 \times 720$, and the output resolution was 800×480 . The bilinear interpolation was adopted by adaptive resolution mode to achieve picture scaling. As shown in Figure 5, four pixels Q_{11} , Q_{12} , Q_{21} , Q_{22} adjacent to the pixel P . The value of pixels can be calculated by (Eqs. 5–9) [28].

$$f(x_{R1}, y_{R1}) = \frac{x_2 - x}{x_2 - x_1} f(x_1, y_1) + \frac{x - x_1}{x_2 - x_1} f(x_2, y_1) \quad (7)$$

$$f(x_{R2}, y_{R2}) = \frac{x_2 - x}{x_2 - x_1} f(x_2, y_1) + \frac{x - x_1}{x_2 - x_1} f(x_2, y_2) \quad (8)$$

$$f(x_P, y_P) = \frac{y_2 - y}{y_2 - y_1} f(x_{R1}, y_{R1}) + \frac{y - y_1}{y_2 - y_1} f(x_{R2}, y_{R2}) \quad (9)$$

Where $f(x, y)$ is the pixel value at the (x, y) point.

2.2.1.2 EWD signal conversion

This system adopted the driver chip of ULTRACHIP Company, which integrated modules such as a source controller, a gate controller and a memory. The thin film

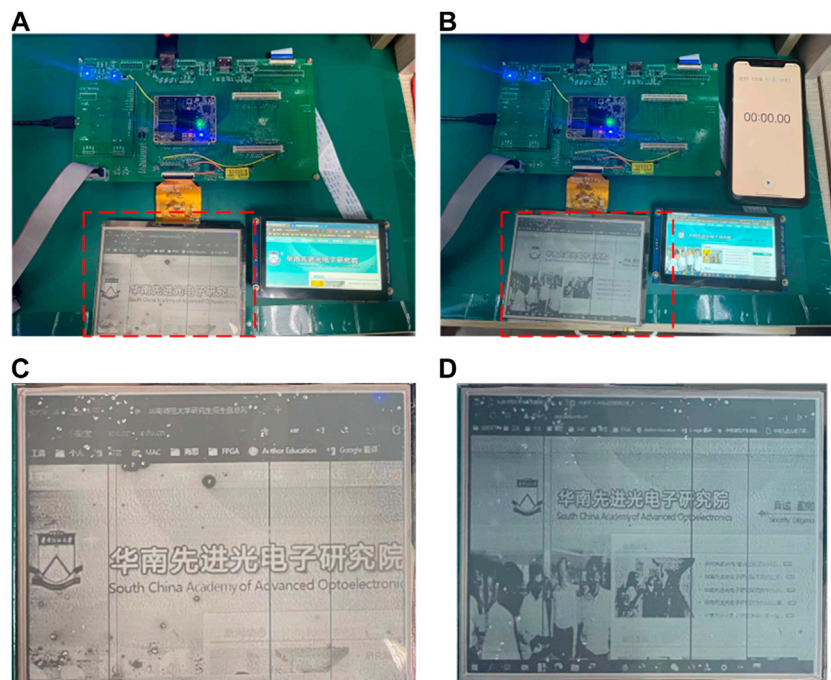


FIGURE 4

An EWD in different modes. (A) The EWD in the cropping mode. (B) The EWD in the adaptive resolution mode. (C) Is the enlarged detail of (A). (D) Is the enlarged detail of (B).

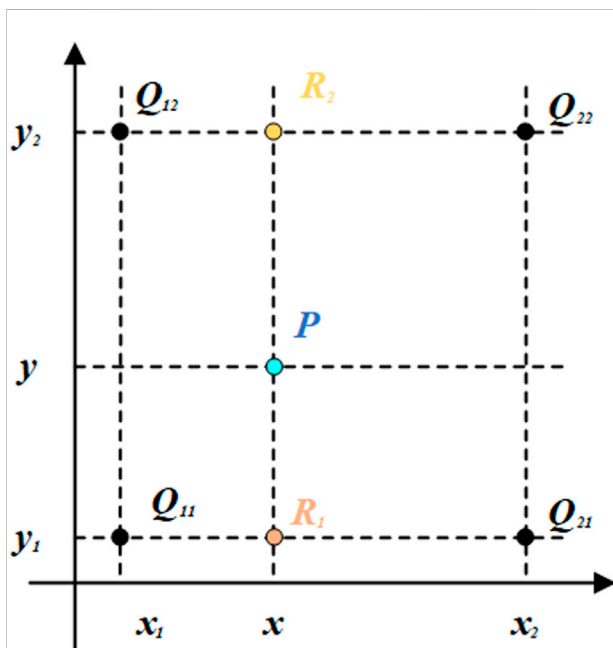


FIGURE 5

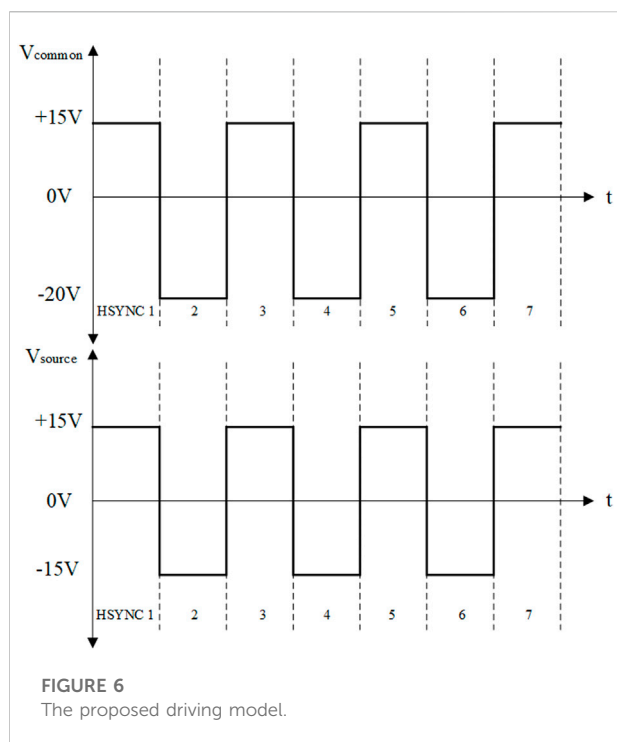
Bilinear interpolation algorithm.

transistor electrowetting displays (TFT-EWD) underlying voltage driving is controlled by a TFT controller with a gate and a source. The pixel voltage was controlled by source and gate controllers [29].

In order to reduce the occupancy of FPGA resources and reduce the low latency of the display, the instant transfer method was adopted. A line of 24-bit data was split into three lines of 8-bit data corresponding to the color data of red (R), green (G), and blue (B) channels. In our experiments, only one channel of color data was extracted as the test-driving display signal. A row of 8-bit data was written into the first input first output (FIFO), and then, the loading was ready, the data was read out from the FIFO and transmitted to the source controller as source data. Source data cooperated with gate control signals to control EWDs. Instant transport and ping-pong operations use two blocks of memory to alternately input and output data, reducing the consumption of SRAM resources [30].

2.2.2 Asymmetric intermediate frequency AC driving model

The oil backflow phenomenon occurs when a DC driving signal was continuously supplied due to the trapped charge. Yi summarized the advantages of unbalanced AC driving waveform,



and the reset signal played an important role in suppressing oil backflow [31]. However, the appearance of the reset signal caused flickers. An asymmetric intermediate frequency AC driving scheme was proposed in this paper to solve this problem. In this paper, the frequency of the AC driving waveform was increased to realize the charge switching to maintain the state of oil, to achieve the effect of maintaining grayscales. It was known in several literatures that oil was millisecond-level responsive [32–34]. Therefore, the transformation of the driving signal was carried out at the frequency of microsecond level by us. Through experimental tests, it was found that the aperture ratio of the forward voltage was greater than the

aperture ratio of the negative voltage under the same voltage [15]. Therefore, the aperture ratio obtained by adjusting the negative voltage was consistent with the aperture ratio of the positive voltage.

As shown in Figure 6, V_{common} is the horizontal synchronizing driving signal to common electrode, V_{source} is the TFT source driving signal. Horizontal synchronization driving signal was used for refresh, odd-numbered lines are driven by +15 V voltage, and even-numbered lines were driven by -20 V. The V_{source} driving voltage waveform remains +15 V and -15 V. Replacing the frame refresh method with the line refresh method could increase the frequency of AC driving, which could make the charge in oil respond quickly, and inhibit the oil backflow effectively.

3 Results and discussion

In order to test the validity of the driving waveform, two test platforms were built. Figure 7A was a luminance test platform for testing the reflectivity of EWDs. Figure 7B was the aperture rate test platform. (a) was a computer for receiving and processing data. (b) was a colorimeter for detecting EWDs reflected luminance. (c) was an EWD screen. (d) was an EWD driving system. (e) was a microscope for observing the EWDs pixel structure.

In order to evaluate which DC driving signal has the best display consistency, we tested the aperture ratios under four DC driving waveforms. The EWD switched between “on” and “off” every second interval. As shown in Table 1 and Figure 8, in the case of the maximum value, the aperture ratio at +15 V was 12.33% larger than that of -15 V, and in the case of the average value, the aperture ratio at +15 V was 9.71% larger than -15 V. In the case of the maximum value, the aperture ratio at +20 V was 13.62% larger than -20 V. In the case of the average value, the aperture ratio at +20 V was 8.13% larger than that -20 V. It could be seen from Table 1 that the average value of -20 V in the “on” state and “off” state was close to +15 V, so the asymmetric AC driving was feasible.

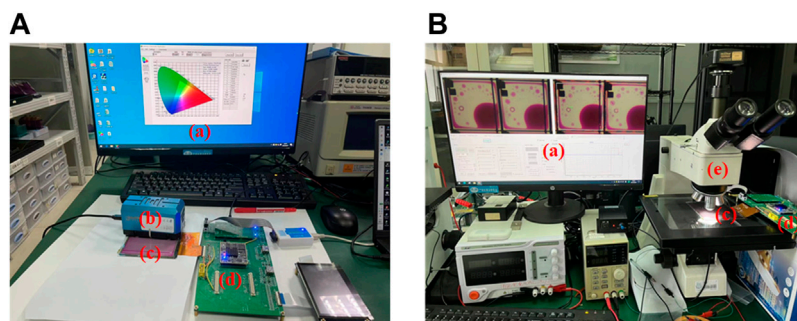
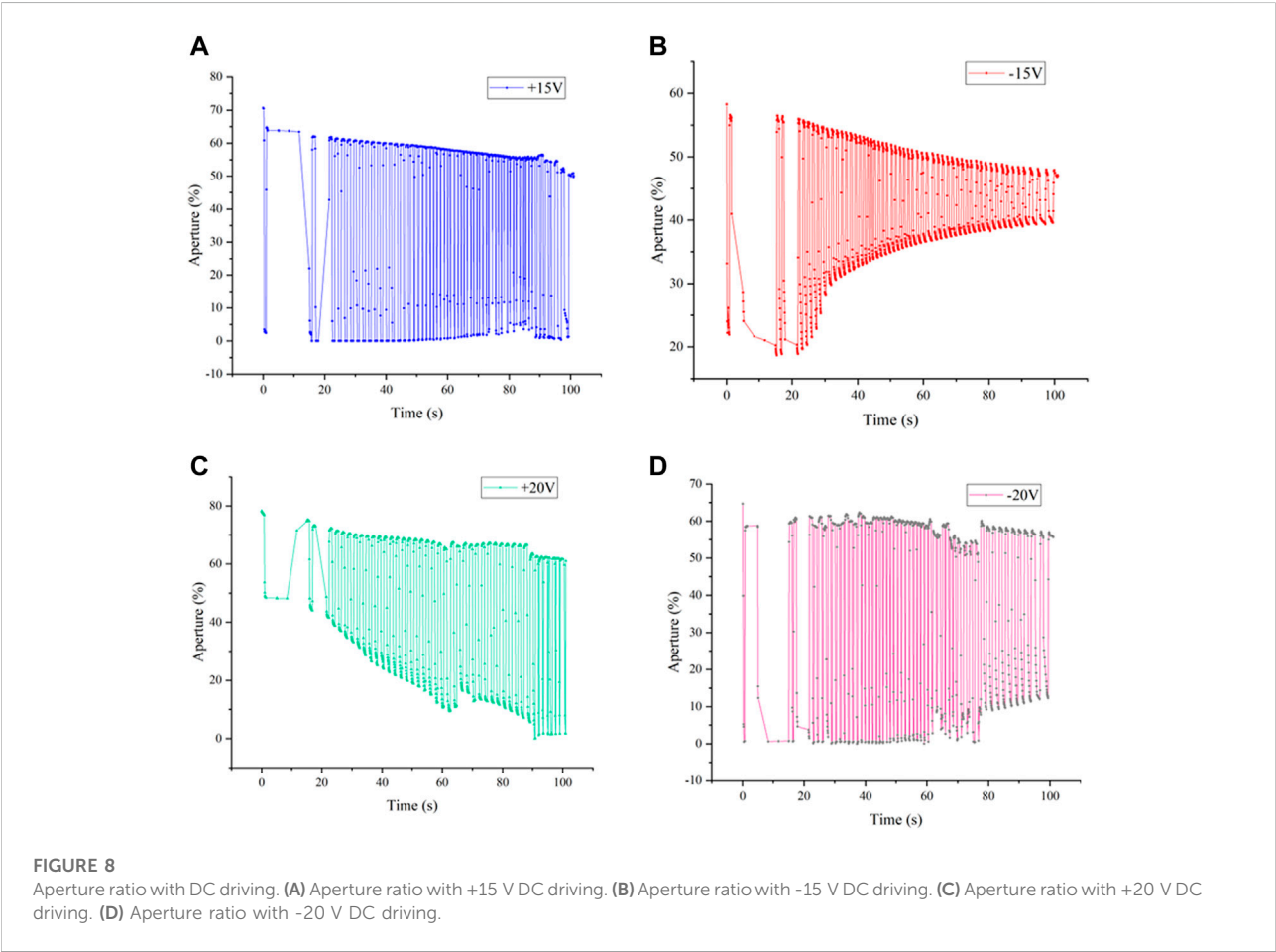


FIGURE 7

Experimental platforms for driving EWDs. (A) A luminance test platform. (B) An aperture test platform. (a) A computer (b) A colorimeter (c) An EWD (d) An EWD driving system (e) A microscope.

TABLE 1 The aperture ratio of different voltages in different states.

	“On” state maximum (%)	“Off” state minimum (%)	“On” state average (%)	“Off” state average (%)
+15 V	70.62	0	58.79	20.33
-15 V	58.29	18.71	49.08	34.25
+20 V	78.3	0	67.62	25.66
-20 V	64.68	0	59.49	21.54



In order to demonstrate the feasibility of asymmetric AC driving, the EWD aperture ratio experiment by AC driving was carried out. As could be seen from Figure 9C, the +20 V and -15 V asymmetric AC driving combination was not feasible. It could be seen from Figure 9 that the asymmetrical AC driving composed of +15 V and -20 V had the largest difference in aperture ratio when the same signal was provided. It was proved that the +15 V and -20 V asymmetric AC driving combination had a higher contrast in the image display process than other combinations.

In the reflected luminance test experiment, the display characteristics of the four combinations of driving waveforms were also different. It could be seen from Figure 10 that the maximum luminance of the asymmetric voltage driving waveform could reach 60.67 absorbance unit (a.u.) in the “on” state under the condition of +15 V and -20 V, and the minimum luminance was 43.69 a. u. In “off” state. Compared with driving waveforms under other voltages, the difference in luminance between the “on” state and the “off” state of the +15 V and -20 V driving waveform was the largest. The average luminance of the +15 V and -15 V driving waveform was lower than that of the

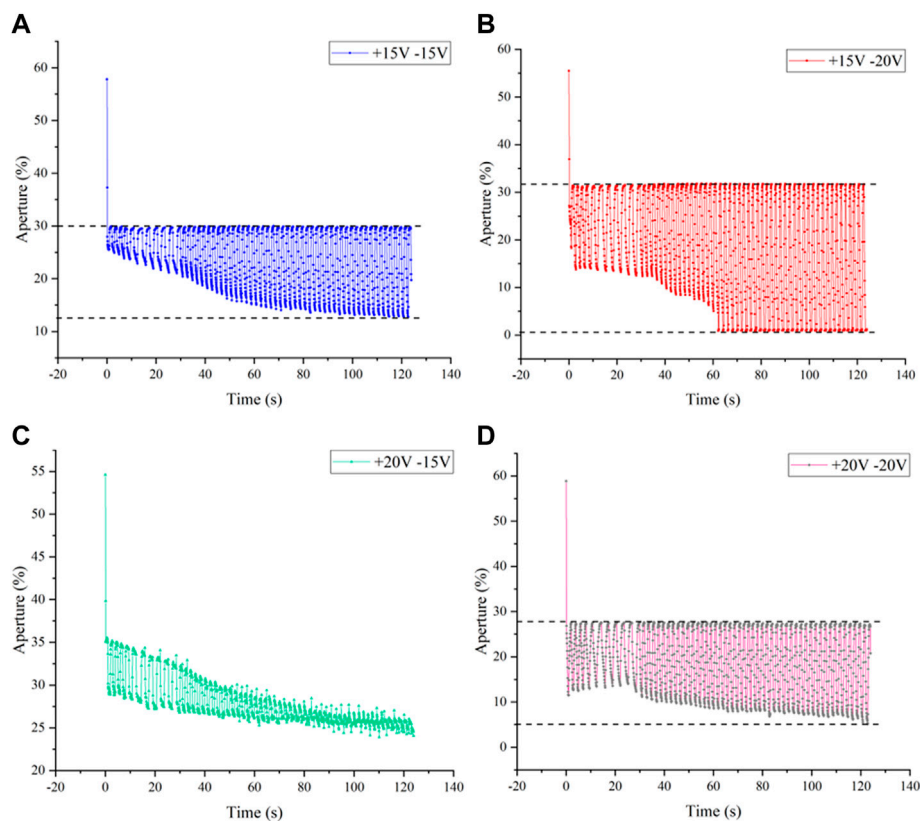


FIGURE 9

Aperture ratio with AC driving. (A) Aperture ratio with AC driving composed of +15 V and -15 V. (B) Aperture ratio of AC driving composed with +15 V and -20 V. (C) Aperture ratio with AC driving composed of +20 V and -15 V. (D) Aperture ratio with AC driving composed of +20 V and -20 V.

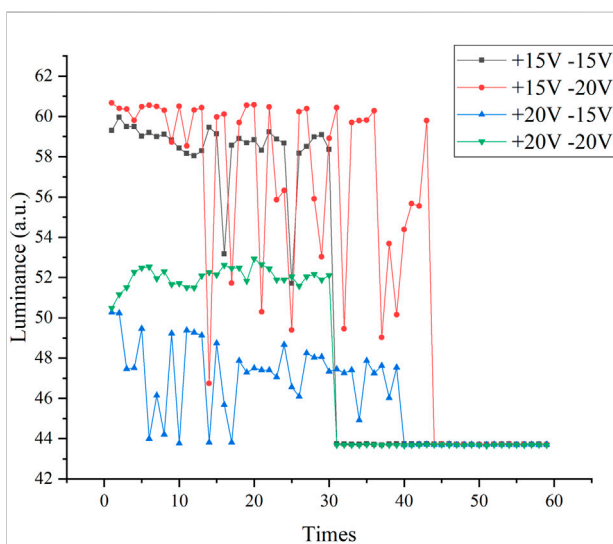


FIGURE 10

Reflected luminance of different driving voltage waveforms.

+15 V and -20 V driving waveform. The driving waveform of +20 V and -15 V had the worst performance, and the maximum luminance could only reach 50.27 a. u. Compared with the traditional symmetrical driving waveform composed of +20 V and -20 V, the maximum luminance of the waveform of +15 V and -20 V was increased by 14%. The large jitter in the reflected luminance in Figure 10 could be caused by the reaction time of oil.

It could be seen from Figure 11 that the display image of the combination of +15 V and -20 V asymmetric AC driving had a higher display effect than other combinations, and image details were richer and the image was clearer. As shown in Figure 11B, compared with Figure 11A, Figure 11C, and Figure 11D, the details of the image marked by the red box in Figure 11B were clearer, and more details could be displayed. Compared with the DC driving waveform, as shown in the image of the area marked by the blue circle in Figure 11, the texture of Figure 11E displayed by the DC driving waveform was best, the overall contrast of the picture was higher, and the displayed content and quality would be better.

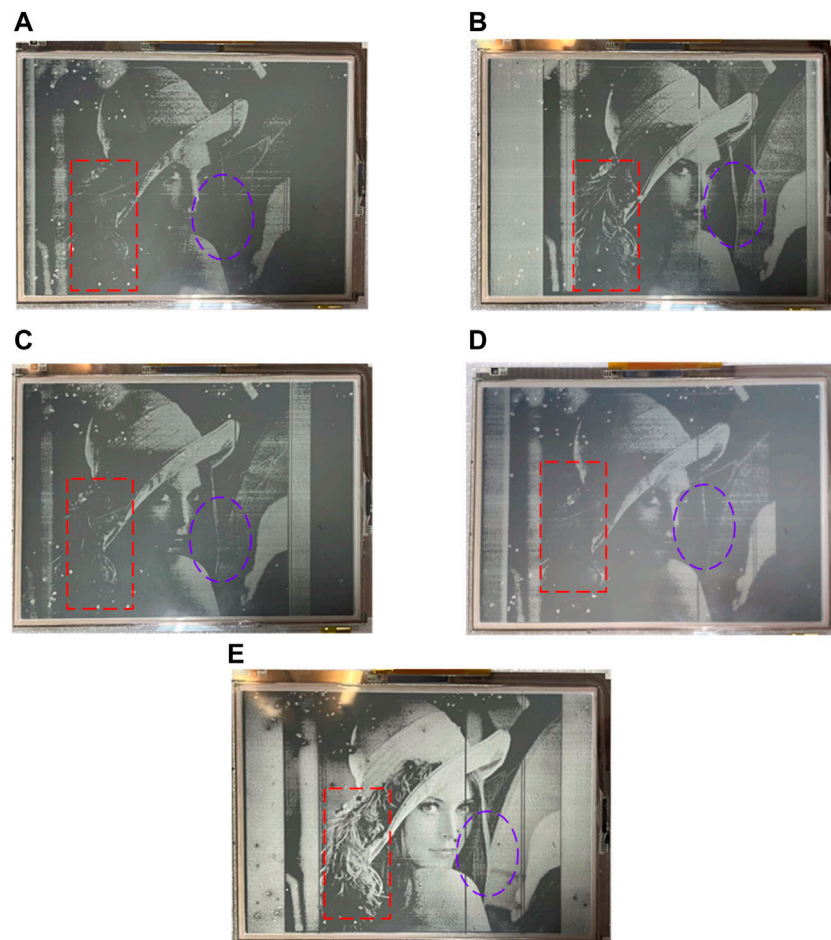


FIGURE 11

The picture of 'Lena' displayed on the EWD. (A) Displayed with the AC driving composed of +15 V and -15 V. (B) Displayed with the AC driving composed of +20 V and -20 V. (C) Displayed with the AC driving composed of +20 V and -15 V. (D) Displayed with the AC driving composed of +20 V and -20 V. (E) Displayed with the +15 V DC driving signal.

In order to prove the influence of AC frequency on the display effect, we tested the influence of the AC driving waveform at different frequencies on EWDs. An asymmetrical AC driving waveform of +15 V and -20 V was used by this frequency test experiment. The test video is a 1-min video of a block moving back and forth. In order to get a better display effect, the output resolution and refresh rate were set to 800×480 and 60 Hz respectively. According to the LCD data sheet, it was known that the LCD line scan period was about 31 μ s. The driving frequency test was carried out in three cases where the signal was inverted every 10 lines, the signal was inverted every 30 lines, and the signal was inverted every 120 lines. The corresponding driving frequencies were 1639 Hz, 543 Hz, and 133 Hz. As shown in Figure 12, with the DC driving waveform, an obvious afterimage phenomenon could be observed in EWDs. In the case of 133 Hz and 543 Hz

AC driving waveform, there were obvious horizontal stripes on EWDs. In the case of the 1,639 Hz AC driving waveform, the horizontal stripe phenomenon disappeared completely, and the contrast ratio was higher.

The afterimage problem in EWDs was solved by the proposed method. As shown in Figure 13, when the video was played to 1 minute, the traditional method had an obvious video afterimage problem. The video sticking problem and flickering problem were effectively solved by the asymmetric IF AC driving model in this paper.

As shown in Figure 14, there were a lot of dead pixels and dead source lines on the screen. The EWD preparation process and production quality were the main factors affecting the current display, resulting in the appearance of dead pixels and abnormal vertical stripes, which affect the overall appearance.



FIGURE 12
Asymmetric AC driving results at different frequencies.

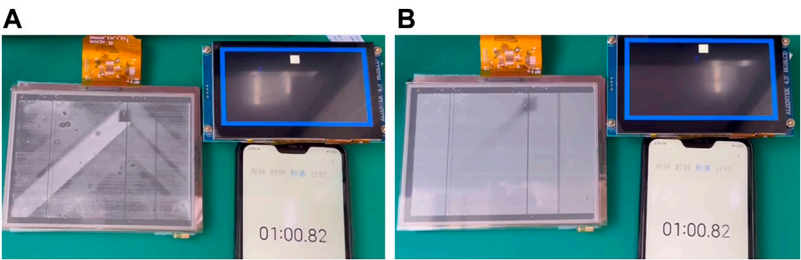
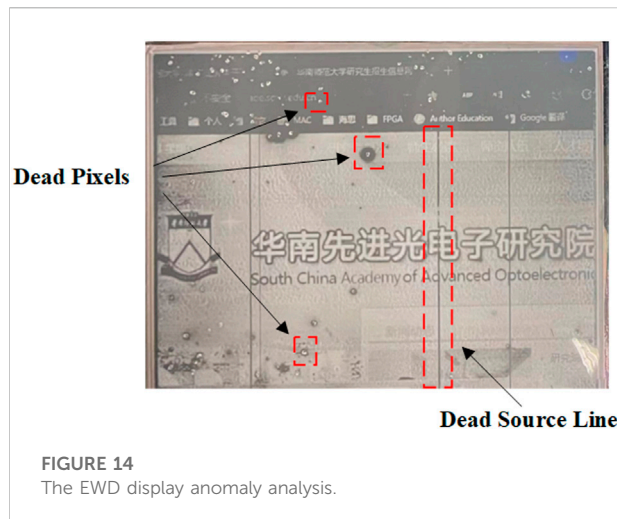


FIGURE 13
The EWD video display with different methods. **(A)** Traditional method (DC driving waveform). **(B)** Asymmetric IF AC driving model (Proposed method).



4 Conclusion

In this paper, an IF asymmetric signal model was designed based on AC driving model. The model was different from the conventional model in that it used the asymmetric signal of IF. It could effectively avoid the afterimage phenomenon that occurs when playing video, and the phenomenon of picture disappearance when playing static images. In addition, a highly integrated EWDs display system was designed for this model, which could display the picture transmitted by the PC in real-time through the HDMI interface. Finally, the asymmetric IF AC driving model was tested in the EWDs display system to prove its validity of the asymmetric IF AC driving model. This paper provided a reliable test solution for EWDs display drivers.

Data availability statement

The raw data supporting the conclusions of this article will be made available by the authors, without undue reservation.

Author contributions

SL wrote the manuscript and performed the experiments YX assisted in manuscript revision and experimental discussion ZZ

References

- Guo Y, Tang B, Yuan D, Bai P, Li H, Yi Z, et al. 3.1: Invited paper: Electrowetting display: Towards full-color video reflective display. *SID Symp Dig Tech Pap* (2021) 52(S2):59–63. doi:10.1002/sdtp.15020
- Chen E, Lin J, Yang T, Chen Y, Zhang X, Ye Y, et al. Asymmetric quantum-dot pixelation for color-converted white balance. *ACS Photon* (2021) 8(7):2158–65. doi:10.1021/acsp Photonics.1c00596
- Hu X, Cai J, Liu Y, Zhao M, Chen E, Sun J, et al. Design of inclined omnidirectional reflector for sidewall-emission-free micro-scale light-emitting diodes. *Opt Laser Tech* (2022) 108335. doi:10.1016/j.optlastec.2022.108335
- Yi Z, Shui L, Wang L, Jin M, Hayes RA, Zhou G. A novel driver for active matrix electrowetting displays. *Displays* (2015) 37:86–93. doi:10.1016/j.displa.2014.09.004
- Li W, Wang L, Henzen A. A multi waveform adaptive driving scheme for reducing hysteresis effect of electrowetting displays. *Front Phys* (2020) 8. doi:10.3389/fphy.2020.618811
- Beni G, Hackwood S. Electro-wetting displays. *Appl Phys Lett* (1981) 38(4):207–9. doi:10.1063/1.92322
- Hayes RA, Feenstra BJ. Video-speed electronic paper based on electrowetting. *Nature* (2003) 425(6956):383–5. doi:10.1038/nature01988

Assist in experimental discussions LL Review the revised manuscript PB Review the revised manuscript.

Funding

This research was supported by National Key R&D Program of China (No. 2021YFB3600603), Program for Guangdong Innovative and Entrepreneurial Teams (No. 2019BT02C241), Science and Technology Program of Guangzhou (No. 2019050001), Program for Chang Jiang Scholars and Innovative Research Teams in Universities (No. IRT_17R40), Guangdong Provincial Key Laboratory of Optical Information Materials and Technology (No. 2017B030301007), Guangzhou Key Laboratory of Electronic Paper Displays Materials and Devices (No. 201705030007) and the 111 Project.

Conflict of interest

The authors declare that the research was conducted in the absence of any commercial or financial relationships that could be construed as a potential conflict of interest.

Publisher's note

All claims expressed in this article are solely those of the authors and do not necessarily represent those of their affiliated organizations, or those of the publisher, the editors and the reviewers. Any product that may be evaluated in this article, or claim that may be made by its manufacturer, is not guaranteed or endorsed by the publisher.

Supplementary material

The Supplementary Material for this article can be found online at: <https://www.frontiersin.org/articles/10.3389/fphy.2022.1033076/full#supplementary-material>

8. Gao J, Mendel N, Dey R, Baratian D, Mugele F. Contact angle hysteresis and oil film lubrication in electrowetting with two immiscible liquids. *Appl Phys Lett* (2018)(20) 203703. doi:10.1063/1.5034510
9. Bansal S, Sen P. Effect of electrowetting induced capillary oscillations on coalescence of compound droplets. *J Colloid Interf Sci* (2018) 530:223–32. doi:10.1016/j.jcis.2018.05.090
10. Ounnunkad K, Patten HV, Velický M, Farquhar AK, Brooksby PA, Downard AJ, et al. Electrowetting on conductors: Anatomy of the phenomenon. *Faraday Discuss* (2017) 199(0):49–61. doi:10.1039/C6FD000252H
11. Wang L, Zhang H, Li W, Li J, Yi Z, Wan Q, et al. Driving scheme optimization for electrowetting displays based on contact angle hysteresis to achieve precise gray-scales. *Front Phys* (2021) 9. doi:10.3389/fphy.2021.655547
12. Li F, Mugele F. How to make sticky surfaces slippery: Contact angle hysteresis in electrowetting with alternating voltage. *Appl Phys Lett* (2008)(24) 244108. doi:10.1063/1.2945803
13. Yi Z, Zhang H, Zeng W, Feng H, Long Z, Liu L, et al. Review of driving waveform for electrowetting displays. *Front Phys* (2021) 9. doi:10.3389/fphy.2021.728804
14. Mukherjee S, Smith N, Goulding M, Topping C, Norman S, Liu Q, et al. A first demonstration and analysis of the biprimary color system for reflective displays. *J Soc Inf Disp* (2014) 22(2):106–14. doi:10.1002/jsid.225
15. Zhang T, Deng Y. Driving waveform design of electrowetting displays based on a reset signal for suppressing charge trapping effect. *Front Phys* (2021) 9. doi:10.3389/fphy.2021.672541
16. Lin S, Zeng S, Qian M, Lin Z, Guo T, Tang B. Improvement of display performance of electrowetting displays by optimized waveforms and error diffusion. *J Soc Inf Disp* (2019) 27(10):619–29. doi:10.1002/jsid.790
17. Yang G, Liu L, Zheng Z, Henzen A, Xi K, Bai P, et al. A portable driving system for high-resolution active matrix electrowetting display based on fpga. *J Soc Inf Disp* (2019) 28(3):287–96. doi:10.1002/jsid.854
18. Qian M, Lin S, Zeng S, Lin Z, Guo T, Tang B. Real-time dynamic driving system implementation of electrowetting display. *Opto-Electronic Eng* (2019) 46(6):180623–19. doi:10.12086/oee.2019.180623
19. Wu H, Hayes RA, Li F, Henzen A, Shui L, Zhou G. Influence of fluoropolymer surface wettability on electrowetting display performance. *Displays* (2018) 53:47–53. doi:10.1016/j.displa.2018.02.002
20. Duan MZ, Hayes RA, Zhang X, Zhou GF. A reflective display technology based on electrofluidics. *Appl Mech Mater* (2014) 670:976–81. doi:10.4028/www.scientific.net/amm.670-671.976
21. Roques-Carnes T, Hayes RA, Schlangen LJM. A physical model describing the electro-optic behavior of switchable optical elements based on electrowetting. *J Appl Phys* (2004) 96(11):6267–71. doi:10.1063/1.1810192
22. Seveno D, Blake TD, De Coninck J. Young's equation at the nanoscale. *Phys Rev Lett* (2013) 111(9):096101. doi:10.1103/PhysRevLett.111.096101
23. Zeng W, Yi Z, Zhao Y, Zeng W, Ma S, Zhou X, et al. Design of driving waveform based on overdriving voltage for shortening response time in electrowetting displays. *Front Phys* (2021) 9. doi:10.3389/fphy.2021.642682
24. Dou Y, Chen L, Li H, Tang B, Henzen A, Zhou G. Photolithography fabricated spacer arrays offering mechanical strengthening and oil motion control in electrowetting displays. *Sensors (Basel)* (2020) 20(2):494. doi:10.3390/s20020494
25. Long Z, Yi Z, Zhang H, Lv J, Liu L, Chi F, et al. Toward suppressing oil backflow based on a combined driving waveform for electrowetting displays. *Micromachines (Basel)* (2022) 13(6):948. doi:10.3390/mi13060948
26. Liu L, Wu Z, Wang L, Zhang T, Li W, Lai S, et al. Clinical features of hepatocellular carcinoma with Hepatitis B virus among patients on Nucleos(t) ide analog therapy. *Infect Agent Cancer* (2020) 15:8. doi:10.1186/s13027-020-0277-y
27. Verheijen HJJ, Prins MWJ. Reversible electrowetting and trapping of charge: Model and experiments. *Langmuir* (1999) 15(20):6616–20. doi:10.1021/la990548n
28. Zhu J, Cheng M, Wang Q, Yuan H, Cai Z. Grape leaf black rot detection based on super-resolution image enhancement and deep learning. *Front Plant Sci* (2021) 12:695749. doi:10.3389/fpls.2021.695749
29. Yi Z, Liu L, Wang L, Li W, Shui L, Zhou G. A driving system for fast and precise gray-scale response based on amplitude-frequency mixed modulation in tft electrowetting displays. *Micromachines (Basel)* (2019) 10(11):732. doi:10.3390/mi10110732
30. Li Y, Gang J. Development of art and culture creative industry using fpga and dynamic image sampling. *Wireless Commun Mobile Comput* (2021) 2021:1–7. doi:10.1155/2021/6639045
31. Liu L, Bai P, Yi Z, Zhou G. A separated reset waveform design for suppressing oil backflow in active matrix electrowetting displays. *Micromachines (Basel)* (2021) 12(5):491. doi:10.3390/mi12050491
32. Yi Z, Liu L, Wang L, Li W, Shui L, Zhou G. A driving system for fast and precise gray-scale response based on amplitude-frequency mixed modulation in tft electrowetting displays. *Micromachines* (2019) 10(11):732. doi:10.3390/mi10110732
33. Yi Z, Feng W, Wang L, Liu L, Lin Y, He W, et al. Aperture ratio improvement by optimizing the voltage slope and reverse pulse in the driving waveform for electrowetting displays. *Micromachines* (2019) 10(12):862. doi:10.3390/mi10120862
34. Yi Z, Huang Z, Lai S, He W, Wang L, Chi F, et al. Driving waveform design of electrowetting displays based on an exponential function for a stable grayscale and a short driving time. *Micromachines (Basel)* (2020) 11(3):313. doi:10.3390/mi11030313



OPEN ACCESS

EDITED BY

Feng Chi,
University of Electronic Science and
Technology of China, China

REVIEWED BY

Qingming Chen,
Sun Yat-sen University, China
Liming Liu,
University of Electronic Science and
Technology of China, China

*CORRESPONDENCE

Hailing Sun,
hailing.sun@m.scnu.edu.cn

SPECIALTY SECTION

This article was submitted to Optics and
Photonics, a
section of the journal
Frontiers in Physics

RECEIVED 05 September 2022

ACCEPTED 10 October 2022

PUBLISHED 21 October 2022

CITATION

Zhang T, Guo Y, Deng Y and Sun H
(2022), An extensible driving model for
multiple grayscales colorful
electrowetting displays.
Front. Phys. 10:1037224.
doi: 10.3389/fphy.2022.1037224

COPYRIGHT

© 2022 Zhang, Guo, Deng and Sun. This
is an open-access article distributed
under the terms of the [Creative
Commons Attribution License \(CC BY\)](#).
The use, distribution or reproduction in
other forums is permitted, provided the
original author(s) and the copyright
owner(s) are credited and that the
original publication in this journal is
cited, in accordance with accepted
academic practice. No use, distribution
or reproduction is permitted which does
not comply with these terms.

An extensible driving model for multiple grayscales colorful electrowetting displays

Taiyuan Zhang¹, Yuanyuan Guo², Yong Deng² and Hailing Sun^{1*}

¹Guangdong Provincial Key Laboratory of Optical Information Materials and Technology & Institute of Electronic Paper Displays, South China Academy of Advanced Optoelectronics, South China Normal University, Guangzhou, China, ²Shenzhen Guohua Optoelectronics Technology Co., Ltd., Shenzhen, China

As a new type of reflective display technology with paper-like display performance, electrowetting display (EWD) can realize ultra-low power consumption, wide viewing angle and fast response speed. In order to apply the EWD to the large-size display field, an extensible driving model for multiple grayscales colorful EWDs was proposed in this paper. The proposed driving model consisted of a grayscale model, a colorful display model and an extensible driving model. With the grayscale model and the colorful display model, the driving waveform of the colorful grayscale display was designed based on limited output voltage levels of a general-purpose graphic driver chip. And then, the extensible driving model was used to realize the large-size display large-scale display based on a matrix of small-size EWD panels. In addition, an experimental platform, which was composed of the display panel and the driving board with a data interface, was designed based on the proposed models. Experimental results showed that it could realize an 18-bit colorful dynamic display on the extended display matrix with a resolution of 48*16. It was indicated that the display matrix could be used for multiple grayscales and colorful dynamic displays by applying the proposed driving models. The research has brought about a way of enlarging the size of the EWD, which is conducive to broadening the scope of application of EWDs.

KEYWORDS

electrowetting display (EWD), driving model, multiple grayscales, driving waveform, dynamic display

Introduction

With a fast response speed, and electrical reproducibility, electrowetting on dielectrics (EWOD) [1] was increasingly used in microsystems. In particular, it has attracted a lot of attention in the areas of digital microfluidics (DMF) [2–4], lab-on-chip [5, 6], micro-lens [7–9], and EWDs [10]. As a novel type of reflective display technology [11], the EWD has ultra-low power consumption [12] and broad viewing angle. In addition, the EWD does not cause a series of environmental pollution problems. In the past few years, the EWD has made numerous achievements in the fields of display materials [13], driving waveforms [14–16] and component designs [17]. These achievements would be

beneficial for the implementation of commercial products or applications, such as E-readers, mobile phones and other mobile terminal devices. However, limited by the current manufacturing process conditions, it is difficult to produce large-size EWD panels which could accommodate the requirements of outdoor billboards and other application scenarios.

In terms of the manufacturing process, a full-color reflective electrowetting displays with diagonals larger than 6 was presented [18]. At the same time, there were many studies on electrowetting grayscale display, color display and video playback. For an active-matrix display, a large range of brightness levels was obtained by using a limited number of grayscales [19]. In addition, a driving scheme was proposed for obtaining multiple grayscales and quick response on a 6-in. SVGA EWD [20]. A portable driving scheme which could display 4-bit grayscale dynamic video was realized by using an active matrix electrowetting display [21]. What's more, the optimization of driving waveform [22] is one of the important ways to improve the display performance of electrophoretic displays (EPDs), as well as the EWDs. Research on optimization of driving waveforms [23], response time [24, 25] and display performance provided a guarantee for grayscale display and video refresh for large-size EWD panels in outdoor scenarios. However, these studies were based on small-scale EWDs in indoor application scenarios.

In order to apply EWDs to outdoor advertisement and other fields requiring large-size displays, an extensible driving model for multi-color EWDs based on digital multiplex (DMX) protocol was provided in this paper. The proposed driving schema consisted of a device cascading section and an EWD driving section. In the device cascading section, a Cortex-M3 processor was used as the host controller to parse the image data frame by frame from the DMX protocol. In the driving section, each EWD panel was driven by a dot matrix liquid crystal graphic column driver chip. According to the parsed image data, the control signal for the driver chip was generated by the host controller to display target images.

Principles

Principles of EWDs

For EWDs, the structure of pixel consists of glass substrate, indium tin oxide (ITO), hydrophobic insulating layer, pixel wall, colored oil, and conductive liquid. The contact angle of the colored oil on the insulating layer can be controlled by the external electric field applied between a common electrode and a pixel electrode. The relationship between the contact angle and the applied electric field can be described by Young-Lippmann equation [26] which is shown in Equation 1.

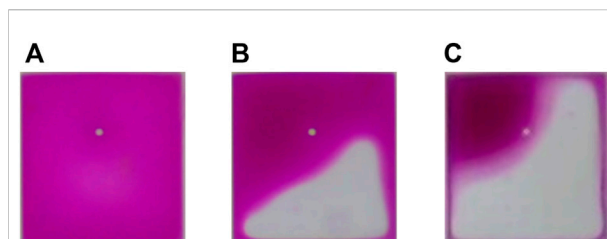


FIGURE 1

The state of pixels under different applied electric fields. (A) When no electric field is applied, the pixel shows the color of oil film. (B,C) are "on" states of a pixel when an electric field is applied. (C) When a maximum voltage is applied, the pixel approaches the most transparent state and the color of the white substrate is displayed.

$$\cos\theta = \cos\theta_0 + \frac{\epsilon_0\epsilon_r V^2}{2d\sigma} \quad (1)$$

Where θ_0 is the initial solid-liquid interface contact angle, θ is the contact angle when the external voltage V is applied. ϵ_0 is the absolute dielectric constant. ϵ_r and d are the relative permittivity and thickness of the dielectric layer, respectively. σ is the interfacial tension between the colored oil and the conductive liquid.

Under the action of the electric field, the original equilibrium state in the liquid system may be broken by the change of external electrical field, thus making the droplet on the insulating substrate to deform or displace. When no electric field is applied between the common electrode and the pixel electrode, oil droplets spread naturally into an oil film on the hydrophobic insulating layer. At this point, the pixel is covered with colored oil film to form an "off" state when viewed from the above. When a certain electric field is applied, the oil film is shrunk to a corner of a pixel. Then, a transparent "on" state is formed at this situation. The pixel state under different applied electric fields is shown in Figure 1. By adjusting the applied electrical field, pixels are in different "on" states, grayscales can be obtained. The degree of "on" states depends on the external voltage applied to the pixel electrodes. The small white point in the pixel is an extra pinning structure (EPS) [27], which is used to guide the oil contraction direction and accelerate the switching on process.

Grayscale model

In EWDs, the degree of colored oil spreading depends on the contact angle according to Young-Lippmann equation. Hence, a grayscale display can be obtained by varying the applied external voltage to change the aperture ratio of pixels. The aperture ratio can be defined as the ratio of the aperture area to the total area of a pixel grid. When the applied voltage is between the breaking

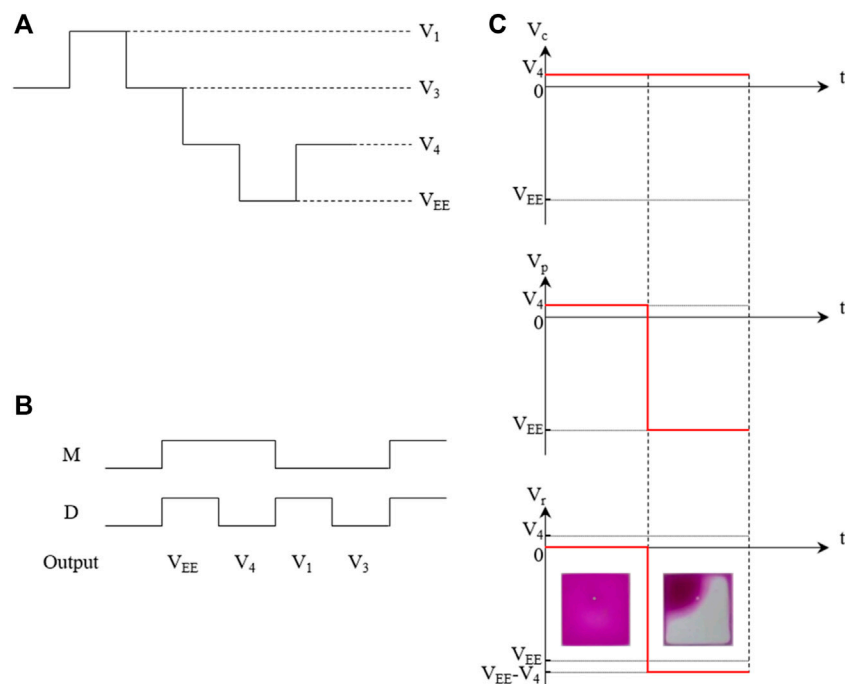


FIGURE 2

The relationship between various voltages. (A) Different power supply voltage levels for the display driver. (B) Selection of the output voltage level. (C) The relationship between pixel state and the voltage applied to the pixel electrode and the common electrode at the time t .

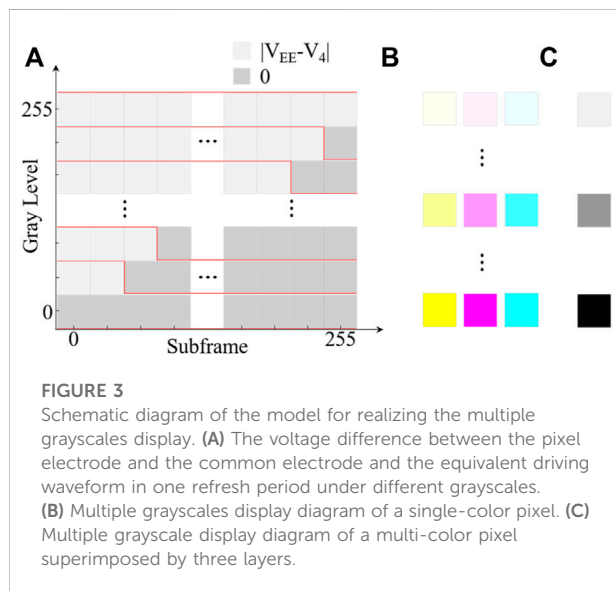


FIGURE 3

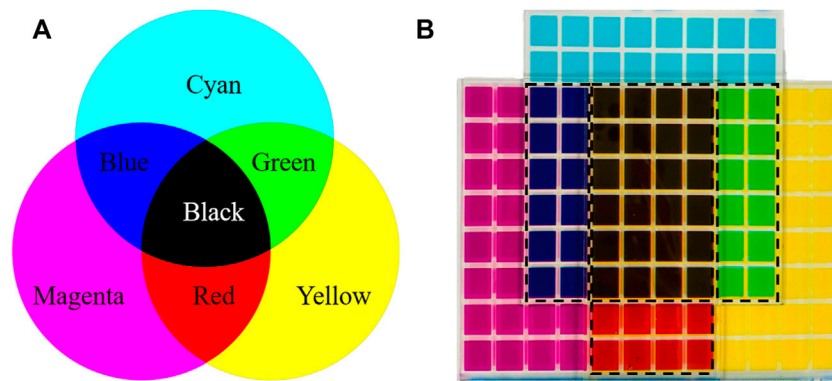
Schematic diagram of the model for realizing the multiple grayscales display. (A) The voltage difference between the pixel electrode and the common electrode and the equivalent driving waveform in one refresh period under different grayscales. (B) Multiple grayscales display diagram of a single-color pixel. (C) Multiple grayscale display diagram of a multi-color pixel superimposed by three layers.

voltage and the maximum voltage, the aperture ratio will increase with the increase of voltage. When the applied voltage is between the breaking voltage and the maximum voltage, the opening ratio will increase with the increase of voltage. However, the relationship between the opening ratio and the driving voltage

is nonlinear. Therefore, it is necessary to adjust the opening ratio through a well-controlled voltage to achieve more accurate grayscale levels. Most general-purpose graphic driver chips are capable of providing limited voltage levels. For example, HD66204FTL is a dot matrix liquid crystal graphic display column driver with 80-channel outputs. And each channel can output one of the four voltage levels V_1 , V_3 , V_4 or V_{EE} , as shown in Figure 2A, depending on the combination of the M signal and display data D, as shown in Figure 2B.

As shown in Figure 2C, if the common electrode voltage V_c is fixed at V_4 , and the state of the pixel can be switched by changing the pixel electrode voltage V_p . When the voltage V_p is V_4 , the voltage difference V_r between the pixel electrode and the common electrode is 0. At this point, the pixel can remain “off” state. If the voltage V_p is V_{EE} , and then the voltage difference V_r is $V_{EE} - V_4$. At this situation, the pixel can switch to the “on” state.

A model for multiple grayscale display based on two voltage levels is presented in Figure 3. In the proposed model, the driving cycle of each pixel was divided into 256 subframes. The visual display of the functional relationship is shown in Figure 3A. In addition, Figure 3A also shows actual driving waveforms applied to the pixel in one driving cycle for each grayscale. Figure 3B and Figure 3C show the grayscale display diagrams of single-color and multi-color pixel, respectively.

**FIGURE 4**

Subtractive primary color system. (A) Schematic diagram of three primary colors and their mixing effects in the subtractive primary color system. (B) The subtractive primary color system in EWDs.

In the one driving cycle, the common electrode voltage V_c can be described by Formula 2. The pixel electrode voltage V_p is determined by Formula 3.

$$V_c = V_4 \quad (2)$$

$$V_p(g, f) = \begin{cases} V_4, & 0 < g < f \leq 255 \text{ or } g = 0 \\ V_{EE}, & 0 < f \leq g \leq 255 \end{cases} \quad (3)$$

In Formula 3, g represents the target grayscale for the pixel, and f denotes the index of the current subframe. When f is greater than or equal to g , V_{EE} should be applied to the pixel electrode to turn on the pixel, otherwise V_4 should be applied to the pixel electrode to turn off the pixel. When the target grayscale is 0, the V_4 should be applied to the pixel electrode throughout the driving period to ensure that the pixel is not activated. According to Formula 2 and Formula 3, the effective voltage V_a applied to the pixel electrode in one driving period can be calculated by Formula 4.

$$V_a(g) = \begin{cases} 0, & g = 0 \\ \frac{1}{256} \sum_{i=0}^g |V_{EE} - V_4|, & 0 < g \leq 255 \end{cases} \quad (4)$$

It can be seen from Formula 4 that 256 different voltage levels are generated based on V_{EE} and V_4 by the proposed grayscale model. The voltage applied to the pixel electrode can be seen as a function of the grayscale and the index of the subframe.

Colorful display model

In contrast to the active light-emitting display technology, the subtractive primary color system was adopted by EWDs. First of all, this is because the EWD is a reflective technology, and the EWD panel does not emit light. Secondly, the subtractive primary color system is conducive to reducing the

loss of light energy in the three-layer stack structure of EWD. As shown in Figure 4A, the subtractive primary color system contains three primary colors: yellow, cyan and magenta. Figure 4B shows the display of yellow, cyan and magenta panels and the display effect after being superposition.

When primary colors are mixed in different proportions, other colors in the color system can be displayed. In the colorful EWD panel, the proportion of each primary color in the mixture is controlled by the grayscale of the pixel. For three primary colors of EWD panels, they have different response curves of aperture ratio with voltage. As a result, they cannot be driven to the same grayscale level by the same voltage. Therefore, a lookup table (LUT) containing the voltage levels corresponding to all grayscales should be built for each color of the panel. Assuming that an 18-bit colorful display is to be implemented, the LUT for three color panels can be defined by Formula 5 ~ Formula 7.

$$C = [c_1, c_2 \cdots c_{63}, c_{64}]^T \quad (5)$$

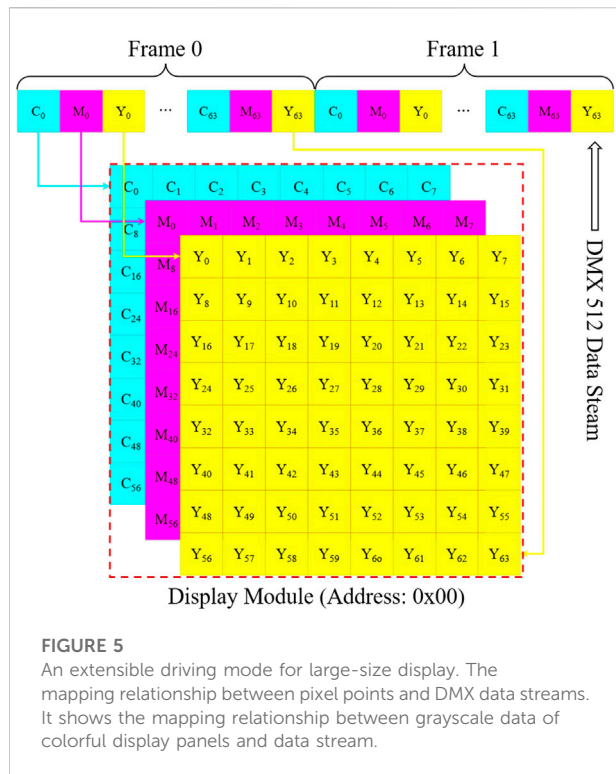
$$M = [m_1, m_2 \cdots m_{63}, m_{64}]^T \quad (6)$$

$$Y = [y_1, y_2 \cdots y_{63}, y_{64}]^T \quad (7)$$

Where C , M and Y represent the LUT of the cyan panel, magenta panel and yellow respectively. Elements c_i , m_i and y_i ($1 \leq i \leq 64, i \in N$) in LUTs represent the driving voltage corresponding to the 64 grayscales. For the cyan panel, the grayscale matrix I_C of a 64-grayscale image with 8 rows and 8 columns can be expressed as Formula 8.

$$I_c = \begin{bmatrix} g_{11} & \cdots & g_{18} \\ \vdots & \ddots & \vdots \\ g_{81} & \cdots & g_{88} \end{bmatrix} \quad (8)$$

Where elements g_{mn} ($1 \leq m \leq 8, 1 \leq n \leq 8, m, n \in N$) represent the grayscale of pixels located at m rows and n columns in



the cyan panel. According to the LUT of the cyan panel, the driving voltage matrix V_c can be calculated by Formula 9. And driving voltage matrixes of the other two color panels can also be calculated in this way.

$$V_c = \begin{bmatrix} c_{g11} & \cdots & c_{g18} \\ \vdots & \ddots & \vdots \\ c_{g81} & \cdots & c_{g88} \end{bmatrix} \quad (9)$$

Extensible driving model

In the extensible driving model, every single colorful panel with the data interface is assigned a module address by an address encoder. With the proposed extensible driving model, the colorful panels can be organized in an orderly manner by the address to achieve large-size displays. Figure 5 shows a schematic diagram of the proposed model. The colorful display module is composed of cyan, magenta and yellow panels. The colorful EWD panel used in the model can be regarded as an image with three channels cyan, magenta and yellow. Each pixel of the module needs 3 bytes of data. The data can be obtained using mature data protocols such as DMX. As shown in Figure 5, the mapping relationship between the grayscale of the pixel in a

certain position and the data stream can be described by Formula 10.

$$G[i, j, k, a] = D[a * 192 + 3 * (8 * i + j) + k] \quad (10)$$

In Formula 10, a represents the address of the current display module, matrix G represents the grayscale data of the display panel. D represents the data stream. The coordinate system is established with the upper left of the panel as the origin, i and j represent the row number and column number of the pixel. Values of k are 0, 1, and 2, which respectively represent cyan panel, magenta panel and yellow panel.

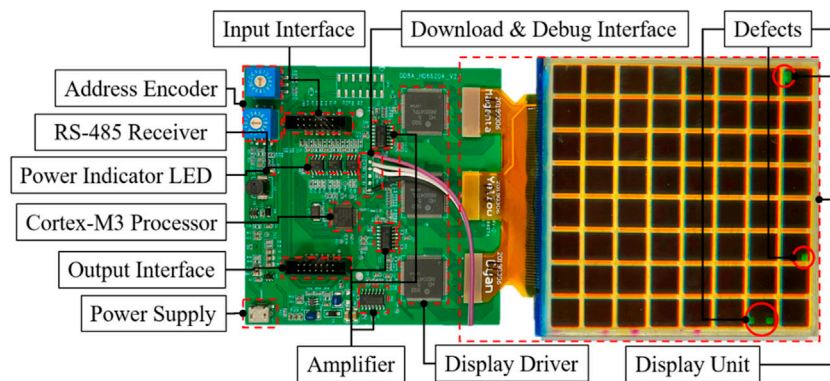
Experimental results and discussions

Experimental platform

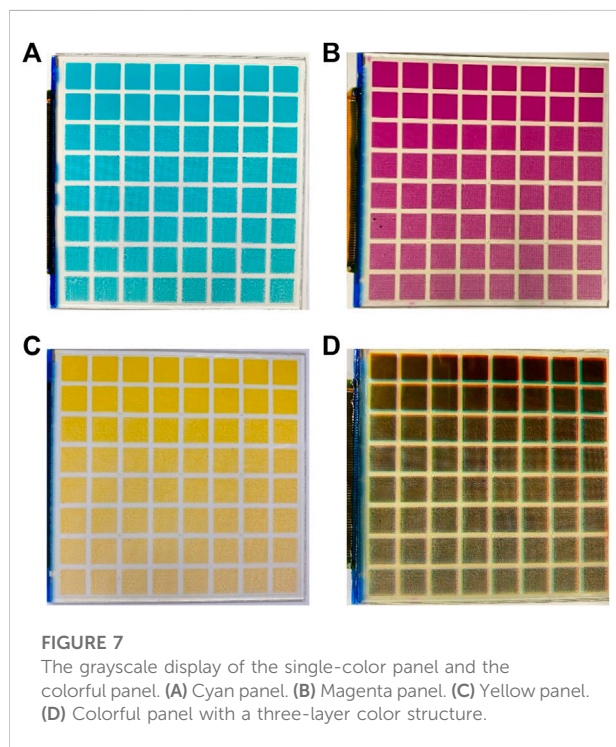
The experimental platform was mainly composed of a colorful display module and a driving board, which is shown in Figure 6. The colorful display module was composed of three-color panels cyan, magenta and yellow. In the driving section, in order to establish the mapping relationship between the grayscales of pixel and data stream, an address code was assigned to each display module via an address encoder. The Cortex-M3 processor would acquire the graphic data corresponding to the pixel according to the obtained device address. And then, the image data was converted into a control signal for display drivers to drive three panels. The output of the amplifier provided input reference voltages for display drivers. And the final output of the display driver depended on the control signal.

The input interface and output interface not only provided an access to data streams but also could be used to provide power for the display module. The display module could also be powered directly through the USB port by accessing an external power supply. To simplify wire connections between display modules, either of the two methods of power supply could be selected flexibly. Yellow, magenta and cyan panels were laminated together to form a display unit for color display. Each color panel contained a pixel matrix with 8 rows and 8 columns.

In the driving board, the Cortex-M3 processor played a very important role in the driving system. Consequently, the design of the program had a direct impact on the display performance of panels. The program could be divided into three parts according to the function of the program: the main program and two interrupt service programs. In the main function, the general-purpose input-output (GPIO), timer, direct memory access (DMA), universal asynchronous receiver transmitter (UART) and other peripherals were initialized in the device startup phase. It was also necessary to enable a timer interruption and a DMA interruption to wait for interrupts. Then, the program entered the main loop to continuously update the DMA buffer based on the received DMX data. When the interrupt was triggered, the program entered the

**FIGURE 6**

The architecture and details of the experimental platform. The experimental platform consisted of a driving board and a display unit. The driving board provided input and output interfaces for DMX signals for the expansion of the display module. It was also responsible for controlling the output voltage applied to pixel electrodes based on the received image data. The display unit had a three-layer color structure. Each panel of the display unit was driven by a graphic driver chip.

**FIGURE 7**

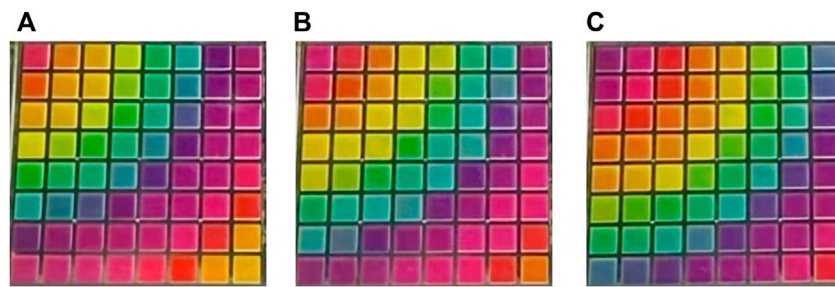
The grayscale display of the single-color panel and the colorful panel. (A) Cyan panel. (B) Magenta panel. (C) Yellow panel. (D) Colorful panel with a three-layer color structure.

interrupt service runtime (ISR) entry to execute the interrupt service function. Since the DMX data received by the display module was address-dependent, the timer interrupts service function was used to read the device address periodically at a frequency of once per second. In addition, based on our

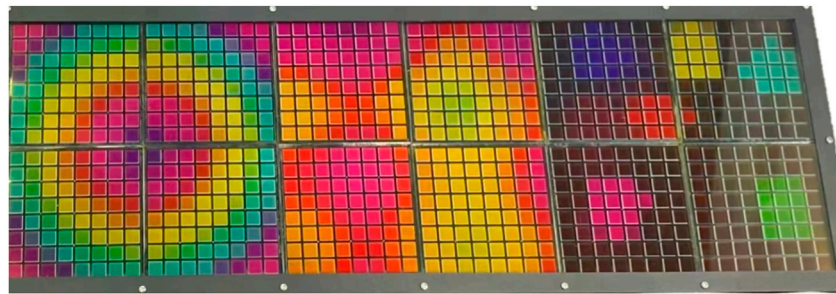
previous research on charge trapping [28], a periodic reset signal was introduced to suppress the impact of oil backflow [29] caused by charge trapping. And the reset signal was also generated in the timer interrupt function. In the external interrupt function of GPIOs, the PA7 pin was used to detect the mark after break (MAB) signal and BREAK signal in the DMX protocol to determine the start and end point of the DMX data. And then the complete DMX data was transferred to the image buffer *via* DMA.

Grayscale display

In Figure 7, panels with eight rows and eight columns were used in the experiment. Sixty-four different voltage levels generated according to the grayscale model were applied to pixel electrodes. As can be seen from experimental results, both the single-color panel and the colorful panel showed several obvious grayscales. It was indicated that the required voltage level for grayscale display could be equivalent to just two different voltage levels with the proposed grayscale model. It should be noted that the voltage difference should be as close as possible to the driving voltage of the EWD panel. If the difference between two voltages was too low, the aperture ratio of the pixel could not reach the maximum, or even the pixel could not be opened at all. Conversely, if the difference between the two voltages was too high, it may cause permanent damage to the pixel structure. Limited by the upper limit and the non-linear characteristics of the aperture ratio, it was difficult to achieve 256 level grayscale display as expected.

**FIGURE 8**

The colorful dynamic display of the EWD panel. In the experiment, a dynamic picture of color gradient was played on the panel, (A), (B,C) were colorful images displayed on the EWD panel at different moments in dynamic display.

**FIGURE 9**

The colorful image displayed on the extended EWD is composed of a dozen display modules.

Colorful dynamic display

When the grayscale of pixels in each single-color panel was controlled according to the grayscale model, the three-color panels were superimposed together to form a colorful display based on the subtractive primary color system. In Figure 8, the colorful image displayed on the EWD panel at a different moment in the dynamic display was displayed. Images of displayed scenes were generated by the host software such as DMX controller software. And then, the data stream of images was transferred to display modules *via* the input interface. Finally, display driver chips were controlled by the driving board to generate the desired driving waveform in real time according to the color display model. In this way, dynamically changing colorful images were constantly displayed on the EWD panel.

Large-size display

In Figure 9, the image displayed on the extended EWD was one of figures contained in the dynamic scene. The extended display was a

display matrix assembled by twelve display modules. The current resolution of the extended screen was 48×16 . Of course, it was also possible to assemble a higher resolution extended screen with more display modules according to the mentioned driving model. The images displayed on the screen were updated in real-time according to scenes created in advance with the DMX controller software.

Conclusion

In this paper, the grayscale model, colorful display model and extensible model were proposed based on a small-size EWD panel. By applying the proposed display models and the driving model, the grayscale display, 18-bit colorful dynamic display and large-size display were realized on the experimental platform. In addition, the reset signal was introduced into the proposed models to improve the display performance. The proposed driving schema has the advantages of simple implementation, low cost, and high scalability due to a mature communication protocol and a common EWDs panel, and it could be applied to other types of display fields.

Data availability statement

The raw data supporting the conclusions of this article will be made available by the authors, without undue reservation.

Author contributions

TZ contributed to the conceptualization, investigation, experiment, data analyses and wrote the manuscript. YG performed a part of experiment and the data analyses. YD helped perform the analysis with constructive discussions. HS contributed to the conception, funding acquisition, resources and supervision. All authors discussed the results and contributed to the final version of the manuscript.

Funding

This research was funded by the National Key Research and Development Program of China (No. 2021YFB3600601), Science and Technology Program of Guangzhou (No. 2019050001), Program for Guangdong Innovative and Entrepreneurial Teams (No. 2019BT02C241), National Natural Science Foundation of China (Nos. 22008156, 12004119), Guangdong Provincial Key Laboratory of Optical Information Materials and

Technology (No. 2017B030301007), Guangzhou Key Laboratory of Electronic Paper Displays Materials and Devices (201705030007), MOE International Laboratory for Optical Information Technologies and the 111 Project.

Conflict of interest

YG and YD were employed by the Company Shenzhen Guohua Optoelectronics Technology Co., Ltd.

The remaining authors declare that the research was conducted in the absence of any commercial or financial relationships that could be construed as a potential conflict of interest.

Publisher's note

All claims expressed in this article are solely those of the authors and do not necessarily represent those of their affiliated organizations, or those of the publisher, the editors and the reviewers. Any product that may be evaluated in this article, or claim that may be made by its manufacturer, is not guaranteed or endorsed by the publisher.

References

- Berge B. Electrocapillarity and wetting of insulator films by water. *Comptes Rendus de l'Academie des Sci - Ser Math* (1993) 317:157–63.
- Gong J, Kim C. All-electronic droplet generation on-chip with real-time feedback control for ewod digital microfluidics. *Lab Chip* (2008) 8(6):898–906. doi:10.1039/b717417a
- Samiei E, Tabrizian M, Hoorfar M. A review of digital microfluidics as portable platforms for lab-on a-chip applications. *Lab Chip* (2016) 16(13):2376–96. doi:10.1039/c6lc00387g
- Feng H, Yi Z, Yang R, Qin X, Shen S, Zeng W, et al. Designing splicing digital microfluidics chips based on polytetrafluoroethylene membrane. *Micromachines* (2020) 11(12):1067. doi:10.3390/mi11121067
- Srinivasan V, Pamula V, Fair R. An integrated digital microfluidic lab-on-a-chip for clinical diagnostics on human physiological fluids. *Lab Chip* (2004) 4(4):310–5. doi:10.1039/b403341h
- Torabinia M, Asgari P, Dakarapu U, Jeon J, Moon H. On-chip organic synthesis enabled using an engine-and-cargo system in an electrowetting-on-dielectric digital microfluidic device. *Lab Chip* (2019) 19(18):3054–64. doi:10.1039/C9LC00428A
- Yang S, Krupenkin T, Mach P, Chandross E. Tunable and latchable liquid microlens with photopolymerizable components. *Adv Mater* (2003) 15(11):940–3. doi:10.1002/adma.200304745
- Berge B. Liquid lens technology: Principle of electrowetting based lenses and applications to imaging. In: Proceedings of the 18th IEEE International Conference on Micro Electro Mechanical Systems; 30 January 2005 - 03 February 2005; Miami Beach, FL, USA (2005). p. 227–30. doi:10.1109/MEMSYS.2005.1453908
- Hu X, Zhang S, Qu C, Zhang Q, Lu L, Ma X, et al. Ionic liquid based variable focus lenses. *Soft Matter* (2011) 7(13):5941–3. doi:10.1039/C1SM05585B
- Hayes R, Feenstra B. Video-speed electronic paper based on electrowetting. *Nature* (2003) 425(6956):383–5. doi:10.1038/nature01988
- Bai P, Hayes R, Jin M, Shui L, Yi Z, Wang L, et al. REVIEW of PAPER-LIKE display technologies (invited review). *Prog Electromagnetics Res* (2014) 147:95–116. doi:10.2528/PIER13120405
- Li W, Wang L, Zhang T, Lai S, Liu L, He W, et al. Driving waveform design with rising gradient and sawtooth wave of electrowetting displays for ultra-low power consumption. *Micromachines* (2020) 11(2):145. doi:10.3390/mi11020145
- Lee P, Chiu C, Lee T, Chang T, Wu M, Cheng W, et al. First fabrication of electrowetting display by using pigment-in-oil driving pixels. *ACS Appl Mater Inter* (2013) 5(13):5914–20. doi:10.1021/am401840b
- Chen Y, Chiu Y, Lee Y, Liang C. 56.3: A charge trapping suppression method for quick response electrowetting displays. *SID Symp Dig* (2010) 41(1):842–5. doi:10.1889/1.3500607
- Zhang T, Deng Y. Driving waveform design of electrowetting displays based on a reset signal for suppressing charge trapping effect. *Front Phys* (2021) 9:672541. doi:10.3389/fphy.2021.672541
- Yi Z, Zhang H, Zeng W, Feng H, Zhang C, Liu L, et al. Review of driving waveform for electrowetting displays. *Front Phys* (2021) 9:728804. doi:10.3389/fphy.2021.728804
- Yi Z, Feng H, Zhou X, Shui L. Design of an open electrowetting on dielectric device based on printed circuit board by using a parafilm M. *Front Phys* (2020) 8:193. doi:10.3389/fphy.2020.00193
- Feenstra J, Schram I, Evans M, Vermeulen P, Cometti C, Weert M, et al. 33.2: Large size full-color ereader displays based on electrowetting. *SID Symp Dig* (2012) 41(1):480–3. doi:10.1889/1.3500499
- Dijk R, Feenstra B, Hayes R, Camps I, Boom R, Wagemans M, et al. 68.3: Gray scales for video applications on electrowetting displays. *John Wiley & Sons, Ltd* (2012) 37(1):1926–9. doi:10.1889/1.2433427

20. Chiu Y, Liang C, Chen Y, Lee W, Chen H, Wu S. Accurate-gray-level and quick-response driving methods for high-performance electrowetting displays. *J Soc Inf Disp* (2011) 19(11):741. doi:10.1889/jsid19.11.741
21. Zhi J, Wei N, Lin W, Xie S, Zhou G. Portable multi-gray scale video playing scheme for high-performance electrowetting displays. *J Soc Inf Disp* (2016) 24(4-6): 345–54. doi:10.1002/jsid.444
22. Yi Z, Zeng W, Ma S, Feng H, Zeng W, Shen S, et al. Design of driving waveform based on a damping oscillation for optimizing red saturation in three-color electrophoretic displays. *Micromachines* (2021) 12(2):162. doi:10.3390/mi12020162
23. Lai S, Zhong Q, Sun H. Driving waveform optimization by simulation and numerical analysis for suppressing oil-splitting in electrowetting displays. *Front Phys* (2021) 9:720515. doi:10.3389/fphy.2021.720515
24. Yi Z, Huang Z, Lai S, He W, Wang L, Chi F, et al. Driving waveform design of electrowetting displays based on an exponential function for a stable grayscale and a short driving time. *Micromachines* (2020) 11(3):313. doi:10.3390/mi11030313
25. Zeng W, Yi Z, Zhao Y, Zeng W, Zhou G, Zhou X, et al. Design of driving waveform based on overdriving voltage for shortening response time in electrowetting displays. *Front Phys* (2021) 9:642682. doi:10.3389/fphy.2021.642682
26. Wikramanayake E, Bahadur V. Characterization of oscillation amplitude of contact angle during ac electrowetting of water droplets. *J Phys Commun* (2020) 4(6):065016. doi:10.1088/2399-6528/ab9ea1
27. Dou Y, Tang B, Groenewold J, Li F, Yue Q, Zhou R, et al. Oil motion control by an extra pinning structure in electro-fluidic display. *Sensors* (2018) 18(4):1114. doi:10.3390/s18041114
28. Wu H, Dey R, Siretanu I, Ende D, Shui L, Zhou G, et al. Electrically controlled localized charge trapping at amorphous fluoropolymer–electrolyte interfaces. *Small* (2019) 16(2):1905726. doi:10.1002/smll.201905726
29. Chevalliot S, Dhindsa M, Kuiper S, Heikenfeld J. Experimental validation of the invariance of electrowetting contact angle saturation. *J Adhes Sci Technol* (2012) 26:1909–30. doi:10.1163/156856111X599580



OPEN ACCESS

EDITED BY

Qiang Xu,
Nanyang Technological University,
Singapore

REVIEWED BY

Li Wang,
Zhongshan Polytechnic, China
Lielin Wang,
Southwest University of Science and
Technology, China
Li Chen,
Xi'an Jiaotong University, China

*CORRESPONDENCE

Minqiang Liu,
liuminqiang22@gscaep.ac.cn,
Xianguo Xu,
xgxu@163.com

SPECIALTY SECTION

This article was submitted to Optics and
Photonics,
a section of the journal
Frontiers in Physics

RECEIVED 03 September 2022

ACCEPTED 17 October 2022

PUBLISHED 28 October 2022

CITATION

Liu M, Xu X, Zeng C and Xiong C (2022),
A study on the influence of dose rate on
total ionizing dose effect of anti-fuse
field programmable gate array—The
irradiation damage is attenuated at low
dose rate.
Front. Phys. 10:1035846.
doi: 10.3389/fphy.2022.1035846

COPYRIGHT

© 2022 Liu, Xu, Zeng and Xiong. This is
an open-access article distributed
under the terms of the [Creative
Commons Attribution License \(CC BY\)](#).
The use, distribution or reproduction in
other forums is permitted, provided the
original author(s) and the copyright
owner(s) are credited and that the
original publication in this journal is
cited, in accordance with accepted
academic practice. No use, distribution
or reproduction is permitted which does
not comply with these terms.

A study on the influence of dose rate on total ionizing dose effect of anti-fuse field programmable gate array—The irradiation damage is attenuated at low dose rate

Minqiang Liu*, Xianguo Xu*, Chao Zeng and Cen Xiong

Institute of Electronic Engineering, China Academy of Engineering Physics, Mianyang, China

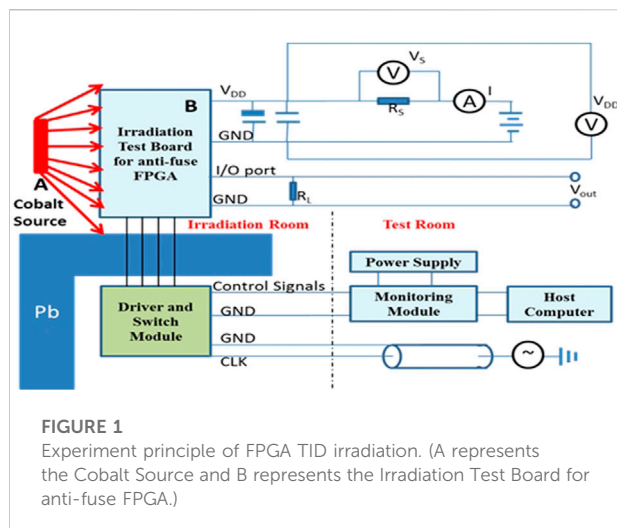
The TID (total ionizing dose) *in-situ* experiments of LC1020B, an anti-fuse FPGA (Field Programmable Gate Array) device, were designed and carried out under different dose rates, and the influence of dose rate on the TID effect of FPGA was studied. The experimental results show that: 1) the TID irradiation failure of the FPGA under different dose rates has nothing to do with the input voltage parameter exceeding the standard. 2) with the decrease of cobalt source irradiation dose rate [171, 26.83, and 2.68 mGy(Si)/s], the TID effect failure dose threshold [168, 229, and 334 Gy(Si), respectively] of the FPGA gradually increased, showing obvious attenuation of low dose rate damage. Theoretical analysis suggests that, compared with the space charge limitation effect, the oxide charge annealing effect plays a dominant role, and longer irradiation time is beneficial to the oxide charge annealing. And based on the experimental data, an FPGA TID analytical model with power consumption current as the damage characterization parameter is established, which lays a foundation for scientific evaluation of radiation effect of anti-fuse FGAs.

KEYWORDS

anti-fuse FPGA, dose rate, TID effect, power consumption current, annealing

Introduction

BECAUSE the electronic devices used in aerospace electronic system will be bombarded by high-energy particles when they work in the radiation environment, their working parameters and service life will inevitably be affected, and system failure or even accidents may be caused in serious cases [1, 2]. FPGA (Field Programmable Gate Array) has a wide application in satellite [3] and other aerospace fields [4] because of its high reliability, strong performance, good flexibility, low power consumption and short development cycle. During the early 1970s, radiation hardened CMOS integrated circuits began to be developed [5]. The international research on the TID effect of FPGA has been carried out in the 1990s [6], and a profound understanding of the test methods [7], sensitive parameters [8], failure law



[9] and simulation model [10] of the TID effect of FPGA devices has been obtained. And a large number of experimental data on TID effect of FPGA have been accumulated [11].

Previous research shows that TID experimental results obtained by different researchers for samples of the same type differs from each other as a result of the different dose rates utilized, sometimes the difference is very great [12, 13]. Therefore, some researchers have carried out targeted studies about the influence of dose rate on the TID effect of MOS devices [14], analyzed the influence of dose rate on the sensitive electrical parameters of MOS devices [15], and found the damage enhancement effect of low dose rate [16]. However, for complex digital devices such as anti-fuse FPGA, there is still a lack of scientific understanding about the influence of dose rate on TID effect of FPGA.

In this paper, for a typical anti-fuse FPGA sample, the power consumption current was selected as its TID effect sensitive parameter and the functional failure dose was selected as the failure threshold. The degradation of electrical properties of FPGA devices under different irradiation dose rates was studied. The phenomenon of low dose rate attenuation was found, and the underlying physical mechanism was considered to be the oxide charge annealing effect. Based on the experimental data, the TID effect analysis model of FPGA power consumption current is established, which lays a foundation for the scientific evaluation of TID radiation effect of anti-fuse FGAs.

Experimental design

Experiment principle

The principle of FPGA TID irradiation experiment under different dose rates is shown in Figure 1. In terms of the realization of the irradiation dose rate, the cobalt source is located at a fixed position. Based on the inverse ratio of the irradiation dose

rate to r^2 (r is the distance between A and B), different irradiation dose rates [171, 26.83, and 2.68 mGy(Si)/s] can be achieved by adjusting the spatial distance between FPGA test board B and cobalt source A (the unit of dose rate was subsequently abbreviated as mGy/s). In order to avoid errors, the locations of different dose rate should be confirmed by dose calibration. In terms of electrical parameters testing, FPGA uses the *in-situ* testing method, the input voltage V_{DD} is measured by the voltage feedback test method, and the power consumption current I ($I = V_s/R_s$) is measured in the FPGA power supply line by the resistance sampling method. In terms of functional testing, the driver and switch module of the FPGA radiation effect detection equipment are placed in a lead chamber shielding the cobalt source radiation to eliminate the influence of test equipment irradiation degradation on the reliability of experimental results, and the clock signal CLK is connected to the driver and switch module to ensure the integrity of the clock signal. FPGA function execution and output signal V_{out} monitoring are controlled by the host computer.

Experimental sample

The experimental sample is an anti-fuse FPGA LC1020B, and its electrical characteristics test conditions specify that the input voltage V_{DD} should be 4.5–5.5 V, and the operating temperature should be -55°C – 125°C . The number of samples is 3, as shown in Table 1.

Experimental layout and configuration

In order to avoid the irradiation damage of experimental testers and high-value electronic equipment, the *in-situ* cobalt source irradiation experiment is carried out through the anti-fuse FPGA radiation effect detection equipment. The experimental layout is shown in Figure 2, and the experimental configuration is listed in Table 2.

Experimental instruments and equipment

The irradiation source, anti-fuse FPGA radiation effect detection equipment, and general electrical parameter test instruments involved in the experiment and their related parameters are listed in Table 3.

Experimental process and results

Irradiation experiment of anti-fuse field programmable gate array at 26.83 and 171 mGy/s dose rate

Two LC1020B anti-fuse FGAs (numbered 101# and 102#, respectively) from the same lot were selected as the experimental

TABLE 1 Total ionizing dose irradiation sample.

Name and type	The device number	Note
Anti-fuse FPGA LC1020B	101#, 102#, 103#	VDD = 5 V, fCLK = 2 MHz

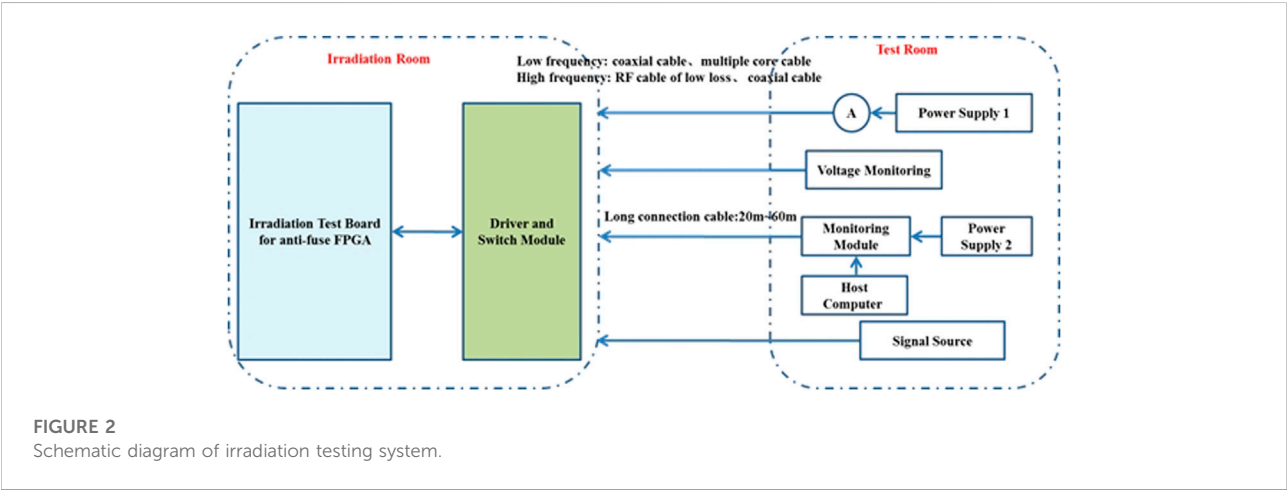


TABLE 2 Experimental configuration.

Configuration name	Configuration requirement
Input/Output bias	The bias condition is: 1) Power supply voltage: 5 V; 2) I/O port load resistance: 5 kΩ
Function program	The anti-fuse FPGA sample function program adopts the general function program, and the utilization rate of the hardware resource (logic gates) of the anti-fuse FPGA reaches 97.5%
Clock configuration	The clock frequency is 2 MHz, and an external signal generator is used to provide the clock signal, which is transmitted to the global clock port through a coaxial long connection cable
Temperature	Room temperature 25°C
Power supply voltage test	The power supply voltage of the FPGA under test is measured by the long-wire voltage feedback test method to ensure that the bias voltage applied to the FPGA through the long-wire transmission meets the specified requirements
Power consumption current test	The power consumption current I ($I = V_S/R_S$) is measured in the FPGA power supply line by the resistance sampling method before, during and after the irradiation experiment
Functional signal test	FPGA function execution and output signal V_{out} monitoring are controlled by the host computer. The output signal V_{out} is transmitted to the test room through a long coaxial cable, and the digital oscilloscope is used to show the function waveform (level and time sequence of the periodic square wave voltage waveform) before, during and after the irradiation experiment

samples. The initial power supply voltage was set at about 5 V, and the irradiation dose rate was 171 and 26.83 mGy/s, respectively. The experimental data of the power supply voltage, power consumption current and function of the sample changing with the irradiation dose are listed in Table 4.

As can be seen from Table 4, no matter which dose rate is used to carry out experiment, the power supply current of the anti-fuse FPGA device increases with the increase of the irradiation dose, and the power supply voltage decreases with the increase of the irradiation dose (the current increases, the voltage drop on the long connection cable increases, so the

input voltage of the sample decreases). When the dose rate is 171 mGy/s, the FPGA failure dose threshold is 168 Gy, and the failure current threshold is 24.3 mA; when the dose rate is 26.83 mGy/s, the FPGA failure dose threshold is 229 Gy, and the failure current threshold is 27.6 mA. From what was said above, the lower the dose rate, the larger the failure dose threshold.

However, since the operating voltage range of the sample is 4.5–5.5 V, and the bias voltage has dropped to 4.295 or 4.211 V when the sample fails, the possibility of sample failure caused by the decrease of input voltage cannot be excluded.

TABLE 3 The experimental instruments and equipment.

Name and type	Relevant parameter
Co-60 γ -ray Source (Belonging to the Institute of nuclear physics and chemistry, China academy of engineering physics)	The experimental conditions of different dose rate in the range of $(10^{-4}-1)$ Gy(Si)/s can be realized by spatial distance adjustment and lead chamber shielding. The irradiation field is calibrated by ferrous sulfide dosimeter
Anti—fuse FPGA radiation effect detection device (Belonging to the Institute of electronic engineering, China academy of engineering physics)	The physical picture of the detection equipment is shown in Figure 3. It mainly includes the irradiation test board, driver and switch module, monitoring module, host computer and relevant test connection cable, etc., which can realize real-time measurement of FPGA function
Rod Schwarz digital oscilloscope RTO 1044	Bandwidth 4 GHz
Universal dual channel 160 MHz pulse signal source DG4162	Output frequency 160 MHz
Dual channel + fixed 5 V output power supply GPC-3030DG	Adjustable voltage 0–30 V
Agilent desktop digital multi-meter 30411A	Test accuracy 1 μ V at 1 V

TABLE 4 Irradiation results of anti-fuse FPGA.

Sample	Dose rate	Power supply voltage/V	Power consumption current/mA	Function	Dose/Gy
The threshold of FPGA failure dose D_{thres} is 229 Gy					
Name: LC1020B Number: 102#	26.83 mGy/s	5.013	4.57	Normal	0
		5.011	4.49	Normal	50
		4.996	5.92	Normal	100
		4.904	15.0	Normal	150
		4.803	25.0	Normal	200
		4.790	26.1	Normal	228
		4.782	27.6	Normal	229
		4.211	75.2	Abnormal	230
The threshold of FPGA failure dose D_{thres} is 168 Gy					
Name: LC1020B Number: 101#	171 mGy/s	4.998	4.49	Normal	0
		5.004	4.53	Normal	50
		4.947	11.3	Normal	100
		4.841	22.9	Normal	150
		4.839	23.1	Normal	158
		4.831	24.3	Normal	168
		4.295	86.1	Abnormal	169

Irradiation experiment of anti-fuse field programmable gate array at 2.68 mGy/s dose rate

In order to exclude the possibility of sample failure caused by the decrease of input voltage, another LC1020B anti-fuse FPGA (No. 103#) from the same lot was selected as the experimental sample. The 4.2 V bias power supply voltage test was conducted on the sample before irradiation, and it was found that the sample

could work normally. During irradiation, the initial power supply voltage of the experimental sample was set as 5.5 V, and the dose rate of irradiation was 2.68 mGy/s. The experimental data of the power supply voltage, power consumption current and function of the sample changing with the irradiation dose are listed in Table 5.

As can be seen from Table 5, when the sample fails, the input voltage is 4.568 V, which excludes the factor that the input voltage parameter exceeds the standard and causes the FPGA

TABLE 5 Irradiation result of anti-fuse FPGA at 2.68 mGy/s dose rate.

Sample	Dose rate	Power supply voltage/V	Power consumption current/mA	Function	Dose/Gy
The threshold of FPGA failure dose D_{thres} is 334 Gy					
Name: LC1020B Number: 103#	2.68 mGy/s	5.459	4.68	Normal	0
		5.460	4.72	Normal	50
		5.456	5.02	Normal	100
		5.426	8.18	Normal	150
		5.343	16.23	Normal	200
		5.241	26.31	Normal	250
		5.191	31.28	Normal	300
		5.170	32.98	Normal	334
		4.568	33.76	Abnormal	335
		4.556	91.56	Abnormal	336

failure. Under the condition of 2.68 mGy/s dose rate, the failure dose threshold of FPGA is 334 Gy, and the failure current threshold is 32.98 mA.

As can be seen from Table 4 and Table 5, no matter which dose rate is used to carry out irradiation experiment, the power consumption current of the anti-fuse FPGA increases with the increase of irradiation dose. The lower the irradiation dose rate, the greater the failure dose threshold and failure current threshold of the FPGA.

Analysis of experimental results

Based on the above experimental results, it takes 2,077 min for 2.68 mGy/s irradiation to reach the FPGA failure dose threshold of 334 Gy; it takes 167 min for 26.83 mGy/s irradiation to reach the FPGA failure dose threshold of 229 Gy; it only takes 16 min for 171 mGy/s irradiation to reach the FPGA failure dose threshold of 168 Gy. Within the dose rate range of this experiment, the power consumption current of the FPGA experimental samples increases with the increase of irradiation dose, and irradiation dose rate is lower, failure dose threshold and failure current threshold of FPGA is higher. There is apparent damage mitigation phenomenon for lower dose rate irradiation, in other words, the irradiation dose rate is lower, the FPGA is more resistant to radiation.

Through the above experimental phenomenon and law analysis, the following understandings are obtained:

- 1) Within the dose rate range of this experiment, it is speculated that, for the TID effect of FPGA samples, the influence of space charge field at different dose rates on the trapping charge generation at the interface is not the dominant effect

mechanism, but the annealing effect of oxide charge at room temperature with time is the dominant effect mechanism.

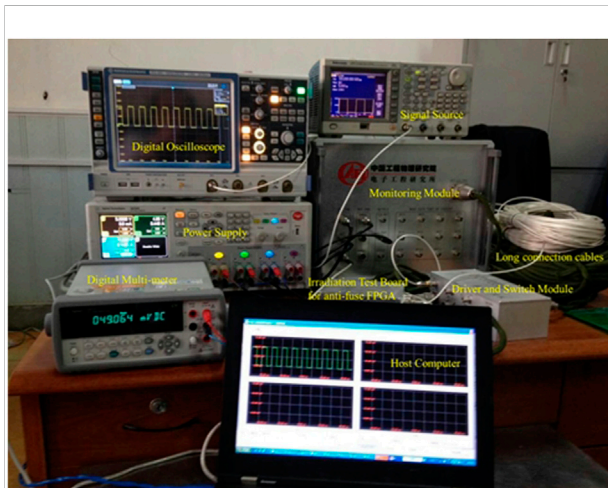
- 2) When the FPGA fails due to 26.83 and 171 mGy/s irradiation, the input voltage is 4.2–4.3 V, and the voltage value is out of standard tolerance (<4.5 V); When the FPGA fails due to 2.68 mGy/s irradiation, the input voltage is 4.568 V and the voltage was not out of standard tolerance (>4.5 V). Therefore, it was recognized that the failure of FPGA sample was not caused by the input voltage out of standard tolerance. The 4.2 V bias supply voltage test of the sample before irradiation also proved this point.
- 3) When the irradiation accumulative dose is small, the power consumption current of the anti-fuse FPGA increases slowly; when the accumulative dose reaches a certain threshold, the power consumption current increases sharply and the FPGA fails immediately. The main reason is that the isolated transistor circuit has a side effect of the TID effect, which results in enhanced leakage current, longer opening time and larger opening transient value.

Total ionizing dose effect model of anti-fuse field programmable gate array

For digital integrated circuits, the threshold voltage of MOSFET is changed by TID irradiation, so the power consumption current increases obviously. When the power consumption current increases to a specific value, a function failure occurs, that is, the output high level signal instantly “disappears.” Since the increase of power consumption current

TABLE 6 The values of parameter at different dose rate.

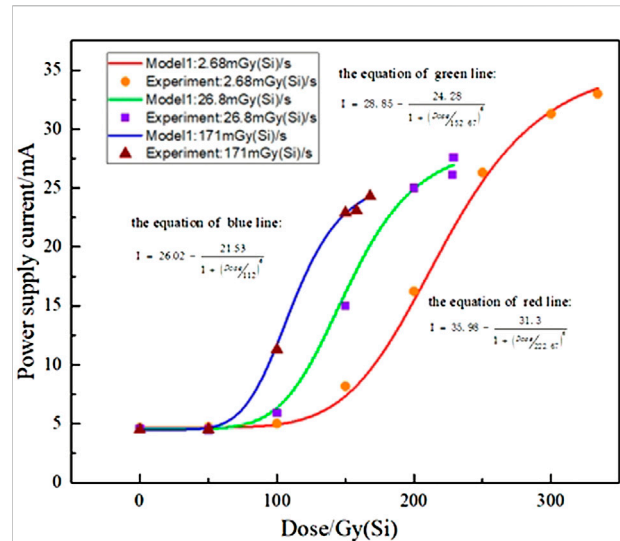
Dose rate	a (mA)	I ₀ (mA)	D _{thres} (Gy)	Dose scope
2.68 mGy/s	35.98	4.68	334	≤334 Gy
26.8 mGy/s	28.85	4.57	229	≤229 Gy
171 mGy/s	26.02	4.49	168	≤168 Gy

FIGURE 3
Physical connection diagram of detection equipment.

is the sum of the contributions of all MOS units such as storage, control and drive unit, and the instantaneous “disappearance” of output signal is mostly caused by the function loss of a certain MOS unit, which is usually caused by the threshold voltage degradation to a specific level. So power consumption current of anti-fuse FPGA is selected as the sensitive electrical parameter for TID effect model.

The correlation model of FPGA power consumption current and radiation dose is established based on the experimental data of power consumption current at different irradiation doses, which can characterize the irradiation degradation characteristics of FPGAs.

Based on the experimental data of different dose points at different dose rate (2.68, 26.8, and 171 mGy/s), the form and parameters of the numerical analytical model representing irradiation degradation characteristics of FPGAs were determined by data analysis, as shown in Eqs 1, 2, where a is the dose-rate correlation parameter; I_0 is the initial current; D_{thres} is the threshold of FPGA failure dose; Dose is the irradiation dose received by the FPGA device; DoseRate is the irradiation dose rate of FPGA device.

FIGURE 4
Experiment and Simulation results of FPGA TID effect.

$$I = a + \frac{I_0 - a}{1 + \left(\frac{\text{Dose}}{\frac{1}{3} \times D_{thres}}\right)^6} \quad (1)$$

$$a = 26 + \frac{10}{1 + \left(\frac{\text{DoseRate}}{20}\right)^3} \quad (2)$$

The values of parameter in Eqs 1, 2 are listed in Table 6.

The 100 or 200 Gy FPGA experimental data obtained based on the experiment were put into the FPGA irradiation experimental degradation analytical model, as shown in Figure 4. The experimental data and numerical prediction results were basically consistent within the allowable error range.

Conclusion

The experimental study on TID effects under different dose rates for anti-fuse FPGA LC1020B was carried out, and the following conclusions were obtained:

- 1) Within the dose rate range of this experiment, the lower the dose rate, the higher the failure dose threshold of the anti-fuse FPGA, that is, the lower the dose rate, the more radiation resistant. It is speculated that the underlying physical mechanism is the dominant effect of oxide charge annealing in FPGA devices at room temperature.
- 2) The observed failure of the anti-fuse FPGA has nothing to do with the insufficiency of input power supply voltage parameter.

In addition, an analytical degradation model of TID effect of the anti-fuse FPGA is established based on experimental data. The model can be used to rapidly predict the degradation degree of FPGA performance at different irradiation doses of specific

dose rates, which lays a foundation for scientific evaluation of radiation effect of anti-fuse FPGAs.

Data availability statement

The raw data supporting the conclusion of this article will be made available by the authors, without undue reservation.

Author contributions

ML, XX, and CZ designed the research, conducted the literature review, experiment and wrote this manuscript. All authors contributed to the literature review, discussion of the results and edited the manuscript.

References

- Swift G, Katz R. An experimental survey of heavy ion induced dielectric rupture in Actel Field Programmable Gate Arrays (FPGAs). *IEEE Trans Nucl Sci* (1996) 43: 967–72. doi:10.1109/23.510741
- Lee D. *Modeling the reliability of highly scaled field-programmable gate arrays in ionizing radiation*. [Los Angeles, (CA)]: University of Southern California (2016). [dissertation/doctoral thesis].
- Quinn H. Radiation effects in reconfigurable FPGAs. *Semicond Sci Technol* (2017) 32:044001. doi:10.1088/1361-6641/aa57f6
- Wang JJ, Katz RB, Sun JS, Cronquist BE, McCollum JL, Speers TM, et al. SRAM based re-programmable FPGA for space applications. *IEEE Trans Nucl Sci* (1999) 46:1728–35. doi:10.1109/23.819146
- Hughes HL, Benedetto JM. Radiation effects and hardening of MOS technology: Devices and circuits. *IEEE Trans Nucl Sci* (2003) 50:500–21. doi:10.1109/TNS.2003.812928
- Clark SD, Bings JP, Maber MC, Williams MK, Alexander DR, Pease RL. Plastic packaging and burn-in effects on ionizing dose response in CMOS microcircuits. *IEEE Trans Nucl Sci* (1995) 42:1607–14. doi:10.1109/23.488756
- Bricas G, Tsiligiannis G, Touboul A, Boch J, Maraine T, Saigne F. FPGA benchmarking structures dedicated to TID parametric degradation evaluation. *IEEE Trans Nucl Sci* (2022) 69:1453–60. doi:10.1109/TNS.2022.3180107
- Lentaris G, Maragos K, Soudris D, Di Capua F, Campajola L, Campajola M, et al. TID evaluation system with on-chip electron source and programmable sensing mechanisms on FPGA. *IEEE Trans Nucl Sci* (2019) 66:312–9. doi:10.1109/TNS.2018.2885713
- Gingrich DM, Buchanan NJ, Chen L, Liu S. Ionizing radiation effects in EPF10K50E and XC2S150 programmable logic devices. *IEEE Radiat Effects Data Workshop* (2002) 1:41. doi:10.1109/REDW.2002.1045530
- Mikkola EO, Vermeire B, Parks HG, Graves R. VHDL-AMS modeling of total ionizing dose radiation effects on CMOS mixed signal circuits. *IEEE Trans Nucl Sci* (2007) 54:929–34. doi:10.1109/TNS.2007.903185
- Katz R, LaBel K, Wang JJ, Cronquist B, Koga R, Penzin S, et al. Radtadiaon effects on current field programmable technologies. *IEEE Trans Nucl Sci* (1997) 44: 1945–56. doi:10.1109/23.658966
- Baoping H, Guizhen W, Hui Z, Jiancheng G, Yinong L, Hui J. Predicting NMOS device radiation response at different dose rates in gamma-ray environment. *Acta Phys Sin* (2003) 52:188–91. doi:10.7498/aps.52.188
- Shaneyfelt MR, Schwank JR, Fleetwood DM, Winokur PS. Effects of irradiation temperature on MOS radiation response. *IEEE Trans Nucl Sci* (1998) 45:1372–8. doi:10.1109/23.685209
- Chen D, Pease R, Kruckmeyer K, Forney J, Phan A, Carls M, et al. Enhanced low dose rate sensitivity at ultra-low dose rates. *IEEE Trans Nucl Sci* (2011) 58: 2983–90. doi:10.1109/TNS.2011.2171720
- Wang Q, Liu H, Wang S, Fei C, Zhao D, Chen S, et al. Total ionizing dose effect of gamma rays on H-gate PDSOI MOS devices at different dose rates. *NUCL SCI TECH* (2017) 28:151–7. doi:10.1007/s41365-017-0295-7
- Hiemstra DM, Shi S, Yang Z, Chen L. Total dose performance at high and low dose rate of a CMOS, low dropout voltage regulator showing enhanced low dose rate sensitivity. 2021. *IEEE NSREC* (2021) 1:1–3. doi:10.1109/TNS.2011.2171720

Conflict of interest

The authors declare that the research was conducted in the absence of any commercial or financial relationships that could be construed as a potential conflict of interest.

Publisher's note

All claims expressed in this article are solely those of the authors and do not necessarily represent those of their affiliated organizations, or those of the publisher, the editors and the reviewers. Any product that may be evaluated in this article, or claim that may be made by its manufacturer, is not guaranteed or endorsed by the publisher.



OPEN ACCESS

EDITED BY
Qiang Xu,
Nanyang Technological University,
Singapore

REVIEWED BY
Jun Zheng,
Bohai University, China
Zelong He,
Yangtze Normal University, China

*CORRESPONDENCE
Lian-Liang Sun,
balac@126.com

SPECIALTY SECTION
This article was submitted
to Optics and Photonics,
a section of the journal
Frontiers in Physics

RECEIVED 17 September 2022
ACCEPTED 28 October 2022
PUBLISHED 14 November 2022

CITATION
Sun L-L and Liu J (2022), Andreev
reflection mediated by Majorana zero
modes in T-shaped double
quantum dots.
Front. Phys. 10:1046802.
doi: 10.3389/fphy.2022.1046802

COPYRIGHT
© 2022 Sun and Liu. This is an open-
access article distributed under the
terms of the [Creative Commons
Attribution License \(CC BY\)](https://creativecommons.org/licenses/by/4.0/). The use,
distribution or reproduction in other
forums is permitted, provided the
original author(s) and the copyright
owner(s) are credited and that the
original publication in this journal is
cited, in accordance with accepted
academic practice. No use, distribution
or reproduction is permitted which does
not comply with these terms.

Andreev reflection mediated by Majorana zero modes in T-shaped double quantum dots

Lian-Liang Sun^{1*} and Jia Liu²

¹College of Science, North China University of Technology, Beijing, China, ²School of Science, Inner Mongolia University of Science and Technology, Baotou, China

We theoretically study the Andreev reflection processes in T-shaped double quantum dots (TDQDs) in terms of the nonequilibrium Green's function technique. It is considered that one of the TDQDs is coupled to the Majorana zero modes (MZMs) prepared at the ends of a topological superconductor nanowire and simultaneously to one metallic and one superconductor lead. Our numerical results show that the in-gap state originated from the proximity effect due to the superconductor lead being sensitive to the existence of MZMs. The local density of states (LDOS) of the spin-up electrons, which are directly coupled to the MZMs, has a Fano antiresonance at the in-gap state. Meanwhile, the local density of the spin-down electrons, which are free from hybridization to the MZMs due to the helical property of the latter, has a Lorentzian resonance at the same state. The differential Andreev conductance of both the spin directions exhibits Fano-type resonance but with different tails' directions. The in-gap state is also significantly influenced by the energy level and coupling strength of the other side-coupled dot, as well as the MZM–MZM interaction.

KEYWORDS

in-gap states, Majorana zero modes, Andreev differential conductance, double quantum dot, Fano effect

1 Introduction

Recent developments in nano-fabrication techniques have enabled the implementation of hybrid devices composed of different materials, such as semiconductor quantum dots (QDs) and metallic or superconductor leads [1–5]. The most important aspect of interest in such a system is the construction of quantum bits relying on the Andreev bound states [6, 7], which are superpositions of the QDs' energy levels and Bogoliubov states in the superconductor leads. In some earlier work, systems with one or multiple QDs connected to one metallic and one superconductor lead were intensively studied, taking the electron–electron interaction that is responsible for the Coulomb blockade and Kondo effects into consideration [3, 8–10]. In macroscopic structures, it is known that the Coulomb interaction between electrons will suppress local pairing and then enhance intersite superconductivity through mechanisms such as spin-exchange processes. However, the relationship between the Coulomb interaction and local pairing is quite difficult to be uncovered, either theoretically or experimentally. Fortunately, this limitation can be

overcome in nanoscale structures by varying the isolated energy levels or interaction strength between electrons. These will change the charge transport and result in a controllable adjustment of the Kondo effect and the opposite case determined by the electron pairing on the QDs. There was also some work concerning joint influences of the quantum interference and proximity effect on electronic transport in multiple QDs, such as T-shaped double quantum dots (TDQDs) sandwiched between one conducting and one superconducting lead [9, 11–13]. It was found that in the subgap regime, i.e., when the external bias voltage is smaller than the energy gap of the superconductor lead [9, 10], the electron transfer is determined by the anomalous Andreev reflections when an electron entering into the dot from the metallic lead is converted into the Cooper pair accompanied by the simultaneous reflection of a hole back to the metallic lead. The transmittance of this Andreev reflection is promising in detecting on-dot pairing induced by the proximity effect and the quantum interference, as well as the Coulomb blockade or Kondo effects. In the presence of on-dot pairing due to the superconductor lead, the quantum interference processes are doubled as compared to similar structures without the superconductor lead. In particular, for TDQD systems, the side-coupled QD induces resonance or antiresonance at particular dot levels controllable by the gate voltage. As a result of it, the Fano effect emerges on the condition that the coupling strength between the two dots is much weaker than that between the dot and the metallic lead [9]. With increasing inter-dot coupling strength, the Fano-type resonance disappears and finally evolves into the Lorentzian resonance due to spreading out of the on-dot pairing from the central dot to the side-coupled dot.

Recent theoretical and experimental works have proved that Majorana zero modes (MZMs) may emerge as exotic quasiparticles at opposite ends of one-dimensional topological superconductors. The MZMs were first predicted in the Kitaev chain of the p-wave superconductor as the degenerate ground state obeying non-Abelian statistics [14, 15]. They are protected by the topological gap and are robust against local perturbations, which makes them promising in fault-tolerant quantum computation [15–17]. Since the spinless Kitaev chain and p-wave superconductor are rare in nature, various theoretical and experimental schemes were then subsequently proposed, such as the hybridized one-dimensional semiconductor–superconductor nanowire under a large enough magnetic field, which is usually called a Majorana nanowire [2, 18]. A p-wave superconductor is realized from the s-wave superconductor due to the proximity effect, given that the semiconductor nanowire has a strong Rashba-type spin-orbit coupling. Unlike the MZMs in the Kitaev chain, others prepared at the ends of the Majorana wire are spinful and may interact with electrons of both the spin directions. To detect the MZMs invasively, researchers also proposed to couple the MZMs to QDs sandwiched between metallic leads [18, 19]. Some interesting phenomena were then found, such as half of the quantum value of the electron conductance [19] and sign reversion of the thermopower [20–22]. There were also some

works concerning MZMs hybridized to QDs with metallic and superconductor leads [23–25]. It was found that in the absence of the intradot Coulomb interaction, there is destructive (constructive) interference for spin-up (spin-down) electrons at the in-gap states. Such an interference effect, combined with the MZMs, exerts significant influence on the transport processes and can be inferred from the local density of states (LDOS) of the QDs and the in-gap Andreev conductance.

In the present article, we study transport through TDQDs side-coupled to the Majorana nanowire having one metallic and one superconductor lead. We concentrate on the influences of the MZMs on the LDOS and Andreev differential conductance within the in-gap regime. Our numerical results show that the LDOS of the spin-up electrons which are directly coupled to the MZMs have an asymmetrical Fano line shape. However, the spin-down electrons that are not directly hybridized to the MZMs have a Lorentzian line shape at the same state. Both spin-up and spin-down differential Andreev conductances have Fano-type resonance at the in-gap state but with different directions of the tails in the line shape. The direct hybridization between the MZMs and side-coupled dots will significantly change the Fano effect.

2 Model and methods

The system is composed of TDQDs connected to one metallic and one superconductor lead, and a nanowire hosting MZMs can be modeled by the following Hamiltonian [9, 10, 19]:

$$H = H_{TDQD} + H_N + H_S + H_T + H_{MZMs}, \quad (1)$$

in which the Hamiltonian for the TDQDs in the absence of the intradot Coulomb interaction is $H_{TDQD} = \sum_{i,\sigma} \epsilon_{di} d_{i\sigma}^\dagger d_{i\sigma} + (t_c d_{1\sigma}^\dagger d_{2\sigma} + H.c.)$. The creation (annihilation) operator $d_{i\sigma}^\dagger$ ($d_{i\sigma}$) is for an electron with the energy level ϵ_{di} ($i = 1, 2$ individually for the central and side-coupled dots) and spin- σ with t_c the coupling strength between electrons on different dots. The Hamiltonian $H_N = \sum_{k\sigma} \epsilon_{kN} c_{kN\sigma}^\dagger c_{kN\sigma}$ is for the normal metallic lead coupled to the central dot with $c_{kN\sigma}^\dagger$ ($c_{kN\sigma}$) creating (annihilating) an electron of momentum k and energy ϵ_{kN} . The superconductor lead is represented by $H_S = \sum_{k\sigma} \epsilon_{kS} c_{kS\sigma}^\dagger c_{kS\sigma} + \sum_k (\Delta c_{kS\uparrow}^\dagger c_{-kS\downarrow}^\dagger + \Delta^* c_{-kS\downarrow} c_{kS\uparrow})$ with the isotropic energy gap Δ . In the present work, we focus our attention on the deep subgap regime $|\epsilon| \ll \Delta$, and then, the Hamiltonian of the superconductor lead is replaced by the creation and annihilation of Cooper pairs [9, 10].

$$H_{Cooper} = \Gamma_S (d_{1\uparrow}^\dagger d_{1\downarrow}^\dagger + d_{1\downarrow} d_{1\uparrow}), \quad (2)$$

where $\Gamma_S = \sum_k |V_{kS}|^2 \delta(\epsilon - \epsilon_{kS})$ denotes the line-width function of the central dot and the superconductor lead with V_{kS} the electron's tunneling amplitude contained in the Hamiltonian for tunneling between the central dot and the leads $H_T = \sum_{k\sigma, \beta=N,S} (V_{k\beta} c_{k\beta\sigma}^\dagger d_{1\sigma} + H.c.)$. The replacement of the

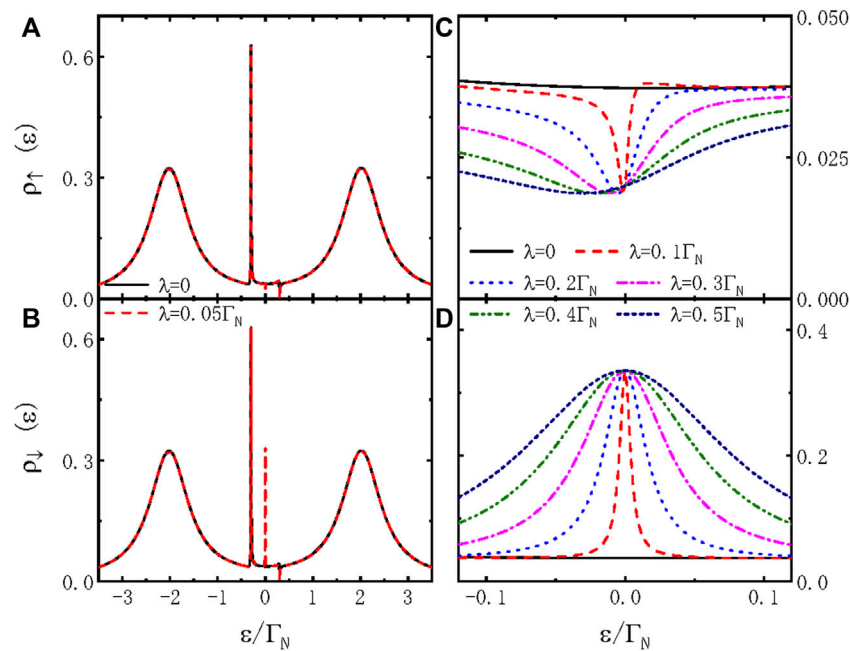


FIGURE 1

(Color online) Spin-dependent LDOS ρ_σ varying with respect to the electron energy ε for different values of dot-MZM hybridization strength λ . The tunneling strength between the central dot and the side-coupled dot is fixed as $t_c = 0.2\Gamma_N$. The energy levels of the two dots are $\varepsilon_{d1} = 0$ and $\varepsilon_{d2} = 0.3\Gamma_N$, respectively. Direct hybridization between the MZMs is $\varepsilon_M = 0$.

complex function of the superconductors by a constant line-width function is called the atomic superconducting limit, which can be seen in [9]. The last term in Eq. 1 represents the MZMs at the ends of the nanowire coupled to the central dot and is given by [19]

$$H_{MZMs} = i\delta_M \eta_1 \eta_2 + \sum \lambda (d_{1\uparrow} - d_{1\downarrow}^\dagger) \eta_1, \quad (3)$$

in which δ_M is the interaction strength between the MZMs with operators satisfying $\eta_j = \eta_j^\dagger$ ($j = 1, 2$) and $\{\eta_i, \eta_j\} = \delta_{ij}$. λ is for hybridization between the MZM and the spin-up electrons on the central dot. Here, we calculate the physical quantities related to transport processes, such as the LDOS and the Andreev differential conductance, with the help of the nonequilibrium Green's function technique. By using the equation of the motion technique and Dyson's equation method, Green's function is obtained in the following form [9, 19, 26]:

$$\mathbf{G}^{-1} = \begin{pmatrix} g_{1,\uparrow}^{-1} + i\Gamma_N/2 & 0 & 0 & -\Gamma_S/2 & -\lambda & -\lambda \\ 0 & \tilde{g}_{1,\uparrow}^{-1} + i\Gamma_N/2 & \Gamma_S/2 & 0 & \lambda & \lambda \\ 0 & \Gamma_S/2 & g_{1,\downarrow}^{-1} + i\Gamma_N/2 & 0 & 0 & 0 \\ -\Gamma_S/2 & 0 & 0 & \tilde{g}_{1,\downarrow}^{-1} + i\Gamma_N/2 & 0 & 0 \\ -\lambda & \lambda & 0 & 0 & g_M^{-1} & 0 \\ -\lambda & \lambda & 0 & 0 & 0 & \tilde{g}_M^{-1} \end{pmatrix}, \quad (4)$$

where Green's function of electrons on the TDQDs free from the interaction between the leads and the MZMs is given by $g_{1,\sigma}^r =$

$1/[\varepsilon - \varepsilon_{d1} + t_c^2/(\varepsilon - \varepsilon_{d2})]$ and that of the hole is $\tilde{g}_{1,\sigma}^r = 1/[\varepsilon + \varepsilon_{d1} + t_c^2/(\varepsilon + \varepsilon_{d2})]$. Similarly, the electron and hole Green's function of the MZMs are individually given by $g_M^r = 1/(\varepsilon - \delta_M)$ and $\tilde{g}_M^r = 1/(\varepsilon + \delta_M)$. The LDOS is thus obtained by $\rho_{\uparrow(1)} = -(1/\pi)\text{Im}G_{11(33)}(\varepsilon)^r$, and the Andreev differential conductance at zero temperature is $G_{A\uparrow(1)} = \Gamma_N^2 |G_{23(14)}(\varepsilon)^r|^2$ [9].

3 Results and discussion

In this section, we present numerical results by choosing the coupling strength between the central dot and the metallic lead $\Gamma_N \equiv 1$ as an energy unit with fixed $\Gamma_S = 4\Gamma_N$. Such a choice of the line-width functions enables the transport processes through the system to be dominated by on-dot pairing arising from the interaction between the dot and the superconductor lead [9, 10]. Otherwise, for $\Gamma_S \ll \Gamma_N$, the electronic states are determined by the Kondo effect arising from the Coulomb repulsion between the spin-up and spin-down electrons, which is neglected in the present paper. Figure 1 presents the spin-dependent LDOS as a function of electron energy ε for different values of dot-MZM coupling strength λ . For $\lambda = 0$, the spin-up LDOS in Figure 1A shows the typical four-peak structure. The peaks formed at the effective quasiparticle states $\varepsilon = \pm \sqrt{\varepsilon_{d1}^2 + (\Gamma_S/2)^2}$ originate from the on-dot pairing by the proximity effect of the superconductor lead. The width of the two peaks is determined by the value of Γ_N ,

whereas their distance in energy is Γ_S , which also indicates the particle-hole splitting of the quasiparticle states [9]. For the present chosen parameters ($\varepsilon_{d1} = 0$), the two states (corresponding peaks in the LDOS) are exactly at $\varepsilon = \pm\Gamma_N/2$. The other pair of peaks emerge at $\varepsilon = \pm\varepsilon_{d2}$ due to the quantum interference effect resulting from the side-coupled dot. These two peaks correspond to the Fano resonance at $-\varepsilon_{d2}$ and antiresonance at $+\varepsilon_{d2}$, respectively. It is worth noting that if the central dot is coupled to two metallic leads, there is just one Fano structure located at ε_{d2} , which can be found in some previous works [27].

Turning on the coupling between the spin-up electrons on the central dot and one mode of the MZMs formed at the ends of the nanowire ($\lambda \neq 0$), a dip (peak) emerges in the spin-up (spin-down) LDOS when the electrons' energy ε is aligned to the Fermi energy in the normal metallic lead $\mu = 0$ (see the red lines in Figures 1A,B). Such a result is the consequence of the combined effect of MZMs and the on-dot pairing due to the superconductor lead. There are two new features in the present TDQDs with one metallic and one superconductor lead as compared to the case of the TDQDs coupled to two normal metallic leads. First, the zero-energy LDOS develops a dip other than a peak that occurred in the latter case. This is due to the combined effects of the quantum interference from the side-coupled dot and on-dot pairing from the superconductor lead. Second, if the spin-down electrons are decoupled from the MZMs, a resonant peak emerges at $\varepsilon = 0$ for nonzero λ . The interaction between the spin-up and spin-down electrons can be understood by examining the off-diagonal elements of the self-energy. If the central dot is coupled to both metallic leads, the spin-down electrons will not be influenced by the MZMs, and the LDOS is solely determined by the quantum interference effect due to the side-coupled dot. The present result is interesting for both detecting the existence of the MZMs and distinguishing electrons of the different spin components, provided there is hybridization between the central dot and the MZMs. As was mentioned previously, searching for the detection scheme for the MZMs is still an important issue in current condensed matter physics. The phenomenon found here may provide a new feasible way for the aforementioned task. With increasing λ , the widths of the dip (peak) in spin-up (spin-down) LDOS become wider with a fixed value of $\rho_{\uparrow(\downarrow)}(\varepsilon = 0)$. Meanwhile, the spin-up and spin-down LDOS remain in the asymmetrical Fano-type and Lorentzian line shape, respectively.

Combined functions of the MZMs, quantum interference, and proximity effect can also be studied by measuring the tunneling current through the system. In Figure 2 we show the dependence of the differential Andreev conductance $G_{A\sigma}(V) = dI_{A\sigma}/dV$ at zero temperature on the bias voltage V . Only a relative narrow bias regime covering the in-gap quasiparticle peak is presented. The quasiparticle peaks at $eV = \pm\sqrt{\varepsilon_{d1}^2 + (\Gamma_S/2)^2}$ are similar to those in Figure 1 and then are neglected. For $\lambda = 0$, the Andreev differential conductance of the two spin components is the same, and they have a pair of

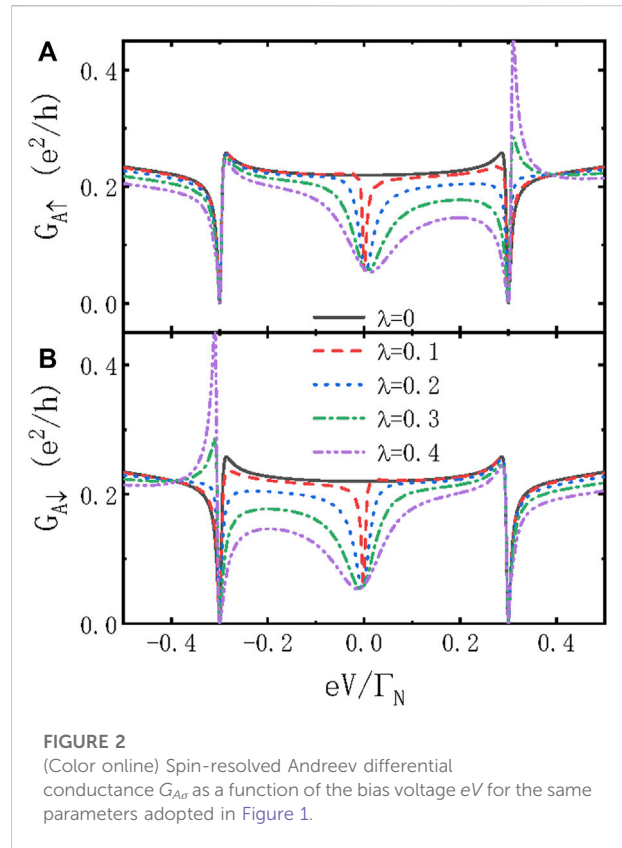


FIGURE 2
(Color online) Spin-resolved Andreev differential conductance $G_{A\sigma}$ as a function of the bias voltage eV for the same parameters adopted in Figure 1.

Fano-type resonance at $eV = \pm\varepsilon_{d2}$ but with different directions of the tail [9]. For this simple case, the Andreev differential conductance can be expressed as $G_{A\sigma} = G_{0\sigma}(x + q)^2/(x^2 + 1) + G_{1\sigma}$ where $x = [eV + \varepsilon_{d2}]$ and q are the asymmetric factors depending on the choice of t_c . With increasing t_c , the value of q is decreased, and the Fano line shape evolves into a Lorentzian line shape. Therefore, here, we choose a relatively small $t_c = 0.2\Gamma_N$ to show the Fano effect. In the presence of MZMs ($\lambda \neq 0$), the Fano resonance in spin-up (spin-down) Andreev differential conductance at positive (negative) bias voltage is drastically changed, whereas that at a negative (positive) bias regime remains almost unchanged. For a sufficiently large value of λ , the directions of the tails in spin-up and spin-down conductances are interchanged. This phenomenon provides an efficient means to detect the existence of the MZMs and is also important in spintronics devices. Moreover, a zero-bias abnormal Fano-type dip emerges at both spin-up and spin-down Andreev differential conductance but with different directions of the tail in the Fano line shape. With increasing λ , the positions of the Fano resonance and antiresonance are interchanged, and then, the directions of the tails in the line shape are reversed, accordingly. This interesting result is fundamentally different from that in the system of QDs coupled to two normal metal leads, in which a zero-bias anomaly (ZBA) in the conductance peak is brought about by the interaction between the QDs and the MZMs [18, 19]. This ZBA is a reliable evidence of the existence of the MZMs.

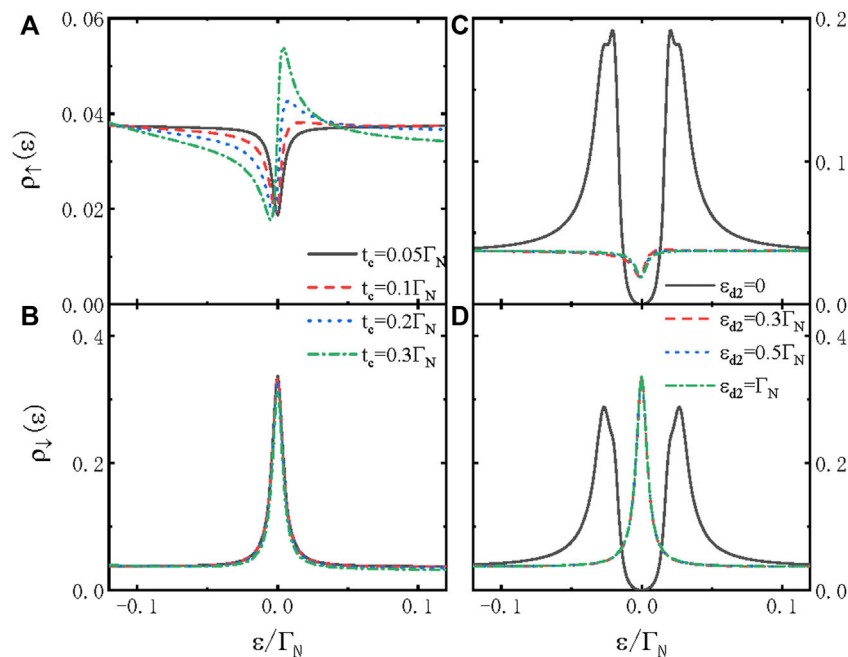


FIGURE 3

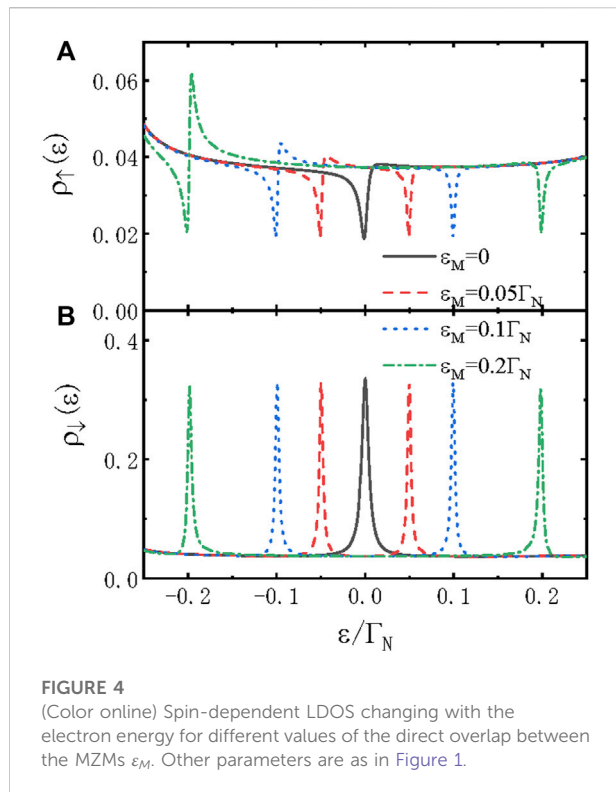
(Color online) Spin-dependent LDOS as a function of the electron energy ε for different values of t_c in (A) and (B), and different ε_{d2} in (C) and (D). Unless indicated, other parameters are as in Figure 1.

However, in the present system of the QDs coupled to one metallic and one superconductor lead, the ZBA evolves into a zero-bias abnormal dip due to the pairing state by the superconductor lead. If the MZMs are replaced by regular fermions, such as another QD, the structure then becomes triple QDs coupled to two leads, which has been studied before. Then, there will be newly emerged Fano peaks in the LDOS and the differential conductance, whose positions are determined by the coupling strengths between the dots and their energy levels. In the present structure, however, the MZMs mainly influence the properties of the structure around the zero-energy point. This is determined by the exotic zero-energy property of the MZMs.

In Figure 3, we present the impacts of the interdot coupling t_c and dot level ε_{d2} on the LDOS. Figure 3A shows that the spin-up LDOS has a Lorentzian-type dip when the electron energy ε is aligned to the dot level $\varepsilon_{d1} = 0$ for a small value of $t_c = 0.05\Gamma_N$ (the solid line). The spin-down LDOS in Figure 3B, however, has a Lorentzian-type peak at $\varepsilon = 0$. With increasing t_c , the quantum interference effect brought about by the additional dot is strengthened, and thus, the spin-up LDOS in Figure 3A shows the Fano line shape. The spin-down LDOS remains in the Lorentzian line shape with a lower peak height. Figures 3C,D show that the LDOS of both the spin-up and spin-down electrons has a symmetrical double-peak configuration, with $\rho_\sigma(0) \equiv 0$ for $\varepsilon_{d2} = 0$. For non-zero ε_{d2} , a Fano (Lorentzian)-type

resonance emerges in the zero-energy spin-up (spin-down) LDOS due to the quantum interference effect. These results are consistent with those in Figures 3A,B. It should be noted that the MZMs are quasiparticles of Majorana fermions, which are characterized by the zero-energy property. Therefore, the MZMs will induce a sharp peak in the spectral function located at the zero-energy level or the zero-bias peak in electrical conductance, which are the most reliable signatures of the existence of MZMs for far. Apart from the zero-energy state, there are no distinct peaks or valleys in spectral function, and then, these states are relatively less important as compared to the zero-energy state. In the presence of the Coulomb repulsive interaction between electrons on the QD, there are two energy states without the external magnetic field. One is at the Fermi level (which is usually at zero-energy), and the other is aligned to the Fermi energy plus the strength Coulomb interaction. As was discussed previously, the state concerning the Coulomb interaction is less influenced by the MZMs, and then, we neglect the Coulomb interaction in the QDs.

The two modes of the MZMs will interact with each other with a strength of δ_M , which depends on the length of the nanowire hosting the MZMs. The MZM-MZM hybridization δ_M exerts significant influences on the electronic transport properties [19–21, 28–30]. For example, the half-fermionic nature of the MZMs (the zero-energy linear conductance of



the QD side-coupled to the MZMs is half of its quantum value G ($eV = 0$) $= e^2/2h$) is destroyed by δ_M [19]. It can also induce a sign reversion in the thermopower of the QD side-coupled to the MZMs [20, 21]. Figure 4 shows that the MZM–MZM hybridization split the single Fano (Lorentzian) resonance in spin-up (spin-down) LDOS for the case of $\delta_M = 0$ into double Fano (Lorentzian) resonance configuration, which is centered at $\varepsilon = \pm\delta_M$. This result is qualitatively consistent with that in [19]. The main difference in the LDOS between the present system and that of [19] is the disappearance of the central peak due to the presence of the superconductor lead. With increasing δ_M , the Fano peaks in the spin-up LDOS become more asymmetric in the negative energy regime, but that in the positive energy regime evolves into a Lorentzian one. For the spin-down electrons, their LDOS is less changed by the variation of δ_M . This is because the spin-down electrons are not directly coupled to the MZMs in the present structure. At last, we note that in experiments, the two modes may interact with the QD simultaneously. [19] Usually, the coupling of the QD to both the modes will enhance or suppress the impacts of the MZMs depending on the arrangement of the coupling strength of different modes. Such a case generally will not change the qualitative functions of the MZMs on the LDOS or the Andreev differential conductance. Another impact of the coupling between the dots with the two modes of the MZMs is the introduction of a phase factor arising from the closed geometry. This phase factor will also exert

important influences on the quantum interference effect and is worth discussing in the future.

4 Summary

In summary, we have studied electronic transport through T-shaped DQDs with the central dot coupled to one normal metallic and one superconductor lead, as well as to a nanowire hosting MZMs. Our numerical results show that the combined effects of the QD–MZM interaction and the on-dot pairing from the superconductor lead exert significant impacts on the LDOS and the Andreev differential conductance. Under some conditions, a Fano- or Lorentzian-type resonance emerges in the spin-resolved LDOS or conductance, which depends on whether the electrons are coupled to the MZMs. Either the position or the strength of the resonance can be efficiently tuned by the quantities related to the MZMs, such as QD–MZMs or MZM–MZM hybridization strengths. The quantum interference arising from the side-coupled dot will change the molecular states induced by the MZMs and the superconductor lead, thus providing an effective means to adjust the system's transport properties.

Data availability statement

The original contributions presented in the study are included in the article/Supplementary Material; further inquiries can be directed to the corresponding author.

Author contributions

L-LS derived the formulae, performed the numerical calculations, and wrote the original manuscript. JL helped derive the formulae and explain the physical mechanisms of the results.

Funding

The authors gratefully acknowledge the financial support from the R&D Program of Beijing Municipal Education Commission (KM201910009002) and the NSFC (Grant No. 12264037).

Conflict of interest

The authors declare that the research was conducted in the absence of any commercial or financial relationships that could be construed as a potential conflict of interest.

Publisher's note

All claims expressed in this article are solely those of the authors and do not necessarily represent those of their affiliated

organizations, or those of the publisher, the editors, and the reviewers. Any product that may be evaluated in this article, or claim that may be made by its manufacturer, is not guaranteed or endorsed by the publisher.

References

- Deacon RS, Tanaka Y, Oiwa A, Sakano R, Yoshida K, Shibata K, et al. Tunneling spectroscopy of andreev energy levels in a quantum dot coupled to a superconductor. *Phys Rev Lett* (2010) 104:076805. doi:10.1103/PhysRevLett.104.076805
- Mourik V, Zuo K, Frolov M, Plissarde R, Bakkers PAM, Kouwenhoven LP. Signatures of majorana fermions in hybrid superconductor-semiconductor nanowire devices. *Science* (2012) 336:1003–7. doi:10.1126/science.1222360
- Weymann I, Wojcik KP. Andreev transport in a correlated ferromagnet-quantum-dot-superconductor device. *Phys Rev B* (2015) 92:245307. doi:10.1103/PhysRevB.92.245307
- Sun QF, Guo H, Wang J. Hamiltonian approach to the ac josephson effect in superconducting-normal hybrid systems. *Phys Rev B* (2002) 65:075315. doi:10.1103/PhysRevB.65.075315
- Sun QF, Wang J, Lin TH. Photon-assisted andreev tunneling through a mesoscopic hybrid system. *Phys Rev B* (1999) 59:13126–38. doi:10.1103/PhysRevB.59.13126
- Rodero AM, Yeyati AL. Josephson and andreev transport through quantum dots. *Adv Phys X* (2011) 60:899–958. doi:10.1080/00018732.2011.624266
- Larsen TW, Petersson KD, Kuemmeth F, Jespersen TS, Krogstrup P, Nygard J, et al. Semiconductor-nanowire-based superconducting qubit. *Phys Rev Lett* (2015) 115:127001. doi:10.1103/PhysRevLett.115.127001
- Sun QF, Guo H, Lin TH. Excess kondo resonance in a quantum dot device with normal and superconducting leads: The physics of andreev-normal co-tunneling. *Phys Rev Lett* (2001) 87:176601. doi:10.1103/PhysRevLett.87.176601
- Baranski J, Domanski T. Fano-type interference in quantum dots coupled between metallic and superconducting leads. *Phys Rev B* (2011) 84:195424. doi:10.1103/PhysRevB.84.195424
- Baranski J, Domanski T. In-gap states of a quantum dot coupled between a normal and a superconducting lead. *J Phys : Condens Matter* (2013) 25:435305. doi:10.1088/0953-8984/25/43/435305
- Baranski J, Domanski T. Decoherence effect on fano line shapes in double quantum dots coupled between normal and superconducting leads. *Phys Rev B* (2012) 85:205451. doi:10.1103/PhysRevB.85.205451
- Calle AM, Pacheco M, Martins GB, Apel VM, Lara GA, Orellana PA. Fano–Andreev effect in a T-shape double quantum dot in the Kondo regime. *J Phys : Condens Matter* (2017) 29:135301. doi:10.1088/1361-648X/aa58c1
- Li YX, Choi HY, Lee HW, Liu JJ. Andreev reflection with spin-flip scattering through a t-shaped double quantum dot. *J Appl Phys* (2007) 101:103918. doi:10.1063/1.2724832
- Fu L, Kane CL. Superconducting proximity effect and majorana fermions at the surface of a topological insulator. *Phys Rev Lett* (2008) 100:096407. doi:10.1103/PhysRevLett.100.096407
- Nayak C, Simon SH, Stern A, Freedman M, Das Sarma S. Non-abelian anyons and topological quantum computation. *Rev Mod Phys* (2008) 80:1083–159. doi:10.1103/RevModPhys.80.1083
- Alicea J, Oreg Y, Refael G, von Oppen F, Fisher MPA. Non-abelian statistics and topological quantum information processing in 1d wire networks. *Nat Phys* (2011) 7:412–7. doi:10.1038/nphys1915
- Karzig T, Knapp C, Lutchyn RM, Bonderson P, Hastings MB, Nayak C, et al. Scalable designs for quasiparticle-poisoning-protected topological quantum computation with majorana zero modes. *Phys Rev B* (2017) 95:235305. doi:10.1103/PhysRevB.95.235305
- Ricco LS, de Souza M, Figueira MS, Shelykh IA, Seridonio AC. Spin-dependent zero-bias peak in a hybrid nanowire-quantum dot system: Distinguishing isolated majorana fermions from andreev bound states. *Phys Rev B* (2019) 99:155159. doi:10.1103/PhysRevB.99.155159
- Liu DE, Baranger HU. Detecting a majorana-fermion zero mode using a quantum dot. *Phys Rev B* (2011) 84:201308. doi:10.1103/PhysRevB.84.201308
- López R, Lee M, Serra L, Lim J. Thermoelectrical detection of majorana states. *Phys Rev B* 89 (2014) 205418. doi:10.1103/PhysRevB.89.205418
- Hong L, Chi F, Fu ZG, Hou YF, Wang Z, Li KM, et al. Large enhancement of thermoelectric effect by majorana bound states coupled to a quantum dot. *J Appl Phys* 127 (2020) 124302. doi:10.1063/1.5125971
- Chi F, Fu ZG, Liu J, Li K, Wang Z, Zhang P. Thermoelectric effect in a correlated quantum dot side-coupled to majorana bound states. *Nanoscale Res Lett* 15 (2020) 79. doi:10.1186/s11671-020-03307-y
- Majek P, Gorski G, Domanski T, Weymann I. Hallmarks of majorana mode leaking into a hybrid double quantum dot. arXiv:2202.09227v1 (2022). doi:10.48550/arXiv.2202.09227
- Feng GH, Zhang HH. Probing robust majorana signatures by crossed andreev reflection with a quantum dot. *Phys Rev B* (2022) 105:035148. doi:10.1103/PhysRevB.105.035148
- Zhang P, Wu H, Chen J, Khan SA, Krogstrup P, Pekker D, et al. Signatures of andreev blockade in a double quantum dot coupled to a superconductor. *Phys Rev Lett* (2022) 128:046801. doi:10.1103/PhysRevLett.128.046801
- Chi F, Wang J, He TY, Fu ZG, Zhang P, Zhang XW, et al. Quantum interference effects in quantum dot molecular with majorana bound states. *Front Phys* 8 (2021) 631031. doi:10.3389/fphy.2020.631031
- Zitko R. Fano-kondo effect in side-coupled double quantum dots at finite temperatures and the importance of two-stage kondo screening. *Phys Rev B* (2010) 81:115316. doi:10.1103/PhysRevB.81.115316
- Jiang C, Zheng YS. Fano effect in the andreev reflection of the aharonov–bohm–fano ring with majorana bound states. *Solid State Commun* (2015) 212:14–8. doi:10.1016/j.ssc.2015.04.001
- Zeng QB, Chen S, Lü R. Fano effect in an ab interferometer with a quantum dot side-coupled to a single majorana bound state. *Phys Lett A* (2016) 380:951–7. doi:10.1016/j.physleta.2015.12.026
- Chi F, He TY, Wang J, Fu ZG, Liu LM, Liu P, et al. Photon-assisted transport through a quantum dot side-coupled to majorana bound states. *Front Phys* 8 (2020) 2541. doi:10.3389/fphy.2020.00254



OPEN ACCESS

EDITED BY

Qiang Xu,
Nanyang Technological University,
Singapore

REVIEWED BY

Rui Yao,
China University of Mining and
Technology, China
Fuyuan Hu,
Suzhou University of Science and
Technology, China

*CORRESPONDENCE

Yunfeng Hu,
✉ huyf@zsc.edu.cn

SPECIALTY SECTION

This article was submitted to Optics and
Photonics,
a section of the journal
Frontiers in Physics

RECEIVED 19 November 2022

ACCEPTED 15 December 2022

PUBLISHED 23 December 2022

CITATION

Hu Y, Hu L, Tang B and Yi Z (2022), A
10 bit 1 MS/s SAR ADC with one LSB
common-mode shift energy-efficient
switching scheme for image sensor.
Front. Phys. 10:1102674.
doi: 10.3389/fphy.2022.1102674

COPYRIGHT

© 2022 Hu, Hu, Tang and Yi. This is an
open-access article distributed under
the terms of the [Creative Commons
Attribution License \(CC BY\)](#). The use,
distribution or reproduction in other
forums is permitted, provided the
original author(s) and the copyright
owner(s) are credited and that the
original publication in this journal is
cited, in accordance with accepted
academic practice. No use, distribution
or reproduction is permitted which does
not comply with these terms.

A 10 bit 1 MS/s SAR ADC with one LSB common-mode shift energy-efficient switching scheme for image sensor

Yunfeng Hu*, Lexing Hu, Bin Tang and Zichuan Yi

Zhongshan Institute, University of Electronic Science and Technology of China, Zhongshan,
Guangdong, China

A 10 bit 1 MS/s SAR ADC with one LSB common-mode shift energy-efficient switching scheme for image sensor is presented. Based on the two sub-capacitor arrays architecture and the common-mode technique, the proposed switching scheme achieves 98.45% less switching energy over the conventional architecture with common-mode shift in one LSB. The comparator uses a low power dynamic comparator. The sampling switch adopts a bootstrap circuit with low sampling error. SAR logic is composed of Bit-Slice circuit with low power consumption and few transistors. Simulated in 180 nm CMOS process and 1 MS/s sampling rate, the ADC achieves the 60.06 dB SNDR, the 75.43 dB SFDR and the 10.45 μ W power consumption.

KEYWORDS

image sensor, SAR ADC, switching scheme, energy-efficient, common-mode shift

1 Introduction

In recent years, successive approximation register (SAR) analog-to-digital converter (ADC) has been widely used in image sensors because of its low power consumption [1–4]. Figure 1 shows the basic processing units in a image sensor application, ADC is an intermediate unit that converts analog signals into digital signals. Among the components of SAR ADC, the energy consumed by capacitor array DAC accounts for a large part of the total energy consumed [5–7]. In order to improve the power efficiency of capacitor DAC, some energy-efficient switching schemes [8–11] have been proposed. Compared to a conventional switching scheme [12], set and down [8], Wang [9], Tri-level [10], and VMS [11] reduce the switching energy by 81.26%, 90.61%, 96.89%, and 97.66%, respectively. However, common-mode shift of these schemes is large.

In this paper, a new one LSB common-mode shift energy-efficient switching scheme is proposed to reduce common-mode shift. Based on the two sub-capacitor arrays architecture and the common-mode technique, the average switching energy of the proposed one LSB common-mode shift switching scheme for 10-bit SAR ADC is $21.08 CV_{ref}^2$. Compared with the conventional [12] switching scheme, the switching



FIGURE 1

Block diagram of image sensor.

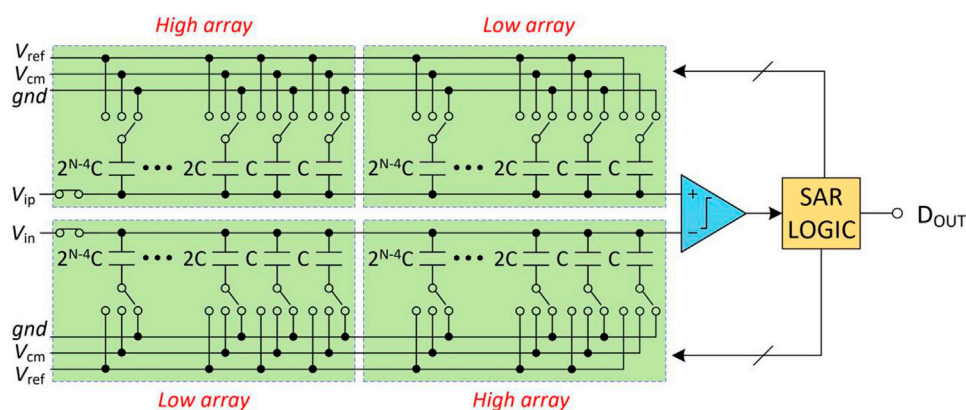


FIGURE 2

The proposed architecture of N-bit SAR ADC.

energy of the proposed switching scheme is reduced by 98.45%. A 10-bit 1 MS/s SAR ADC with the proposed one LSB common-mode shift energy-efficient switching scheme for image sensors is designed and simulated. The comparator uses a fully dynamic low-power comparator. In order to reduce the sampling error, the sampling switch adopts a bootstrap switch circuit [13, 14]. The SAR logic adopts a logic circuit based on Bit-Slice circuit, which can reduce the number of transistors and power consumption of SAR logic [15–17]. This SAR ADC is suitable for image sensor due to the adoption of various low power consumption techniques.

This paper is organized as follows. Section 2 explains the proposed SAR ADC architecture, which includes various low-power design technologies, such as one LSB common-mode shift energy-efficient switching scheme, dynamic comparator, bootstrap sampling switch, SAR logic based on dynamic circuit, etc.; The simulated results and the comparison with the state of the art are shown in Section 3. Finally, Section 4 concludes this article.

2 Proposed SAR ADC

The N-bit SAR ADC of the proposed architecture is shown in Figure 2. The SAR ADC consists of DAC, comparator,

sampling switch and SAR logic. The DAC consists of positive capacitor array and negative capacitor array, and each array is composed of the same two sub-capacitor arrays (high array and low array).

2.1 Proposed one LSB common-mode shift switching scheme

To explain the operation of the proposed one LSB common-mode shift switching scheme, a 4-bit proposed SAR ADC is used. As shown in Figure 3, the operation includes four phases: 1st comparison, 2nd comparison, 3rd to (N-1)th comparison and Nth comparison.

1st comparison: The reference voltages of the high arrays are connected to V_{ref} , and the reference voltages of the low arrays are connected to gnd . The input signals are sampled to the top-plates of all capacitors through the sampling switch. The sampling switches are turned off after sampling. Then, the comparator directly compares the top-plates voltages of the positive and negative capacitor arrays, and outputs the comparison result D_1 (MSB). Therefore, the first comparison did not consume switching energy ($E_1 = 0$).

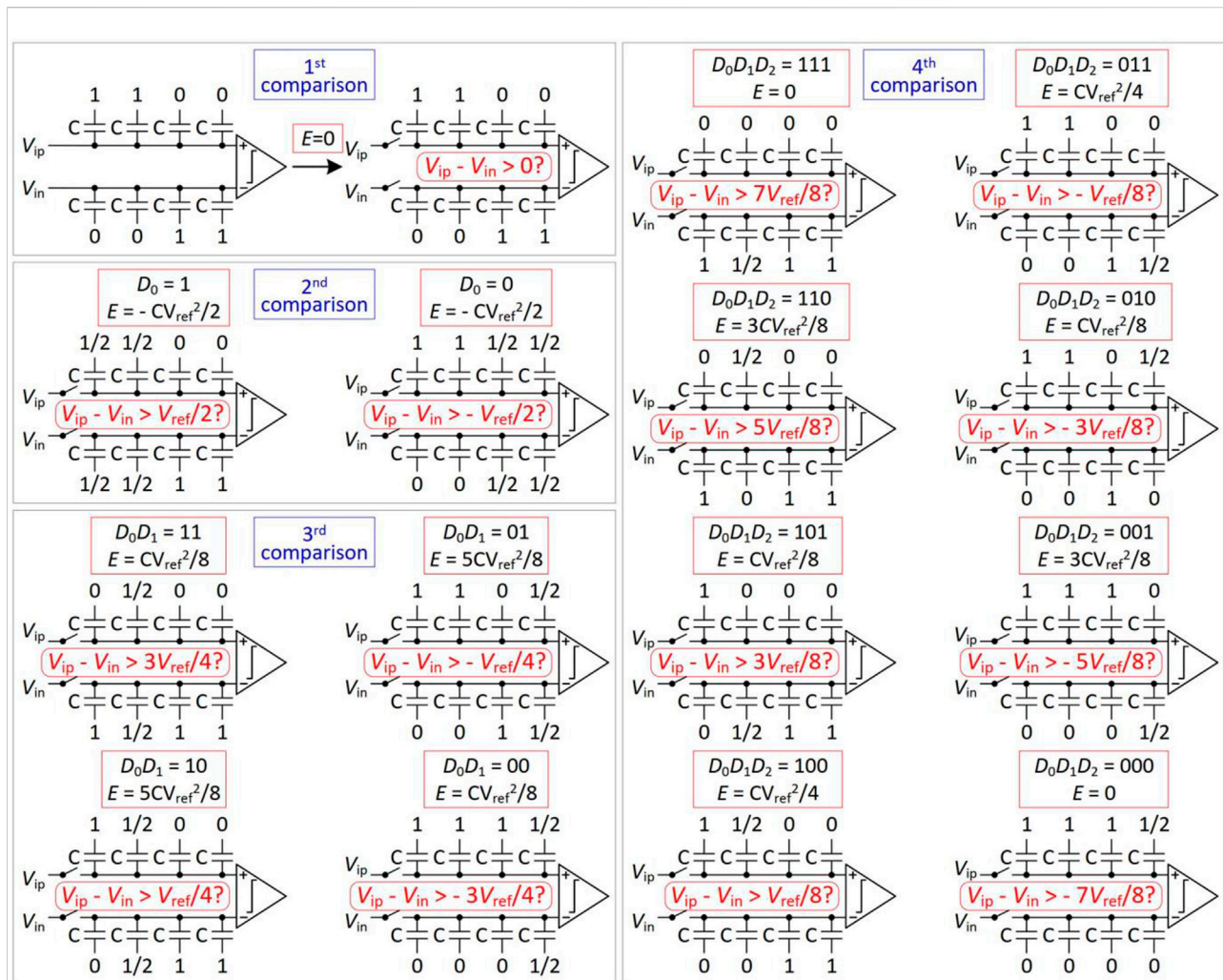


FIGURE 3
Switching procedure of 4-bit SAR DAC.

2nd comparison: If $D_1 = 1$, the reference voltages of the high array in positive capacitor array and the low array in negative capacitor array become V_{cm} ($V_{ref}/2$), and the reference voltages of other capacitors remain unchanged. If $D_1 = 0$, the reference voltages of the low array in positive capacitor array and the high array in negative capacitor array become V_{cm} , and the reference voltages of other capacitors remain unchanged. Therefore, the voltage on the higher side decreases by $V_{ref}/4$, the voltage at the lower side increases by $V_{ref}/4$. Then, the second comparison is performed, and the comparator outputs the result of the second comparison.

3rd to (N-1)th comparison: From the third comparison to the (N-1)th comparison, according to the results of the previous comparison, the reference voltage of the corresponding capacitor in the high-voltage capacitor

array changes from V_{cm} to gnd, and the reference voltage of the corresponding capacitor in the low-voltage capacitor array changes from V_{cm} to V_{ref} . For example, in the third comparison, if $D_2 = 1$, the reference voltage of the largest capacitor connected to V_{cm} in the positive capacitor array is changed from V_{cm} to gnd, and the reference voltage of the largest capacitor connected to V_{cm} in the negative capacitor array is changed from V_{cm} to V_{ref} . If $D_2 = 1$, the operation of positive and negative capacitor arrays will be exchanged. ADC repeats this operation until the (N-1)th comparison is completed. During this process, the common-mode voltage remains unchanged. From the third to (N-1)th comparison, the switching energy of each comparison is derived as

$$E_i = 2^{N-i-2} - 2^{N-2i-1} + (1 - 2D_{i-1}) \sum_{j=1}^{i-2} (2D_j - 1) 2^{N-i-j-2} \quad (1)$$

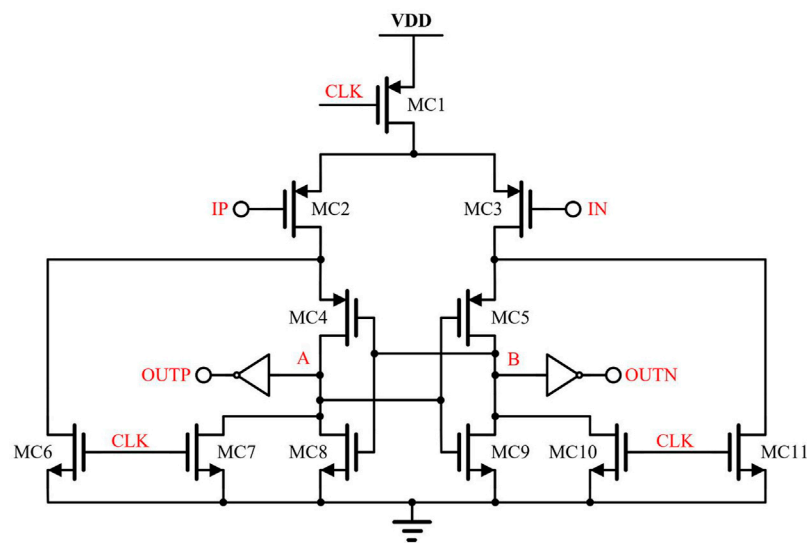


FIGURE 4
Dynamic comparator.

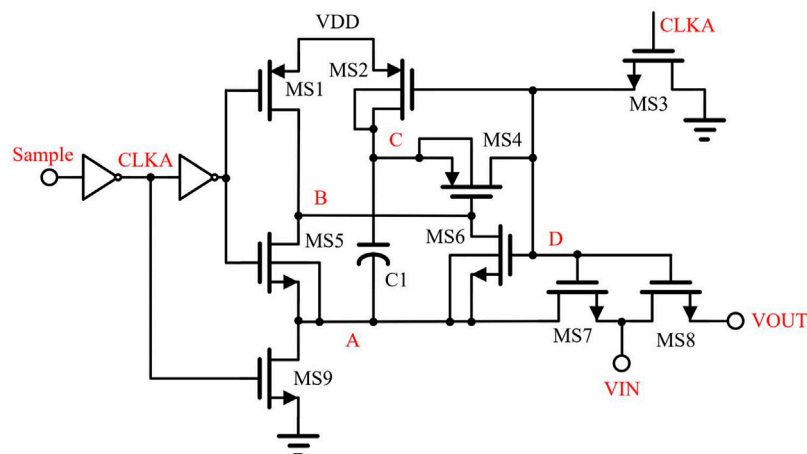


FIGURE 5
Bootstrapped sampling switch.

N^{th} comparison: If $D_{N-1} = 1$, the reference voltage of the last capacitor connected to V_{cm} in the positive capacitor array changes from V_{cm} to gnd, and the reference voltage of the capacitor in the negative capacitor array remains unchanged. If $D_{N-1} = 0$, the operation of positive capacitor array and negative capacitor array will be exchanged. In the N^{th} comparison, the common-mode voltage shifts one LSB. The switching energy in the N^{th} comparison is found to be

$$E_N = 2^{-2} - 2^{-N} + (1 - 2D_{N-1}) \sum_{j=1}^{N-2} (2D_j - 1) 2^{-j-2} \quad (2)$$

The average switching energy of proposed one LSB common-mode shift switching scheme for N -bit SAR ADC is:

$$E_{\text{average}} = 2^{N-2} - 2^{-2} - 2^{-N} + \sum_{i=1}^{N-1} 2^{N-2i-1} \quad (3)$$

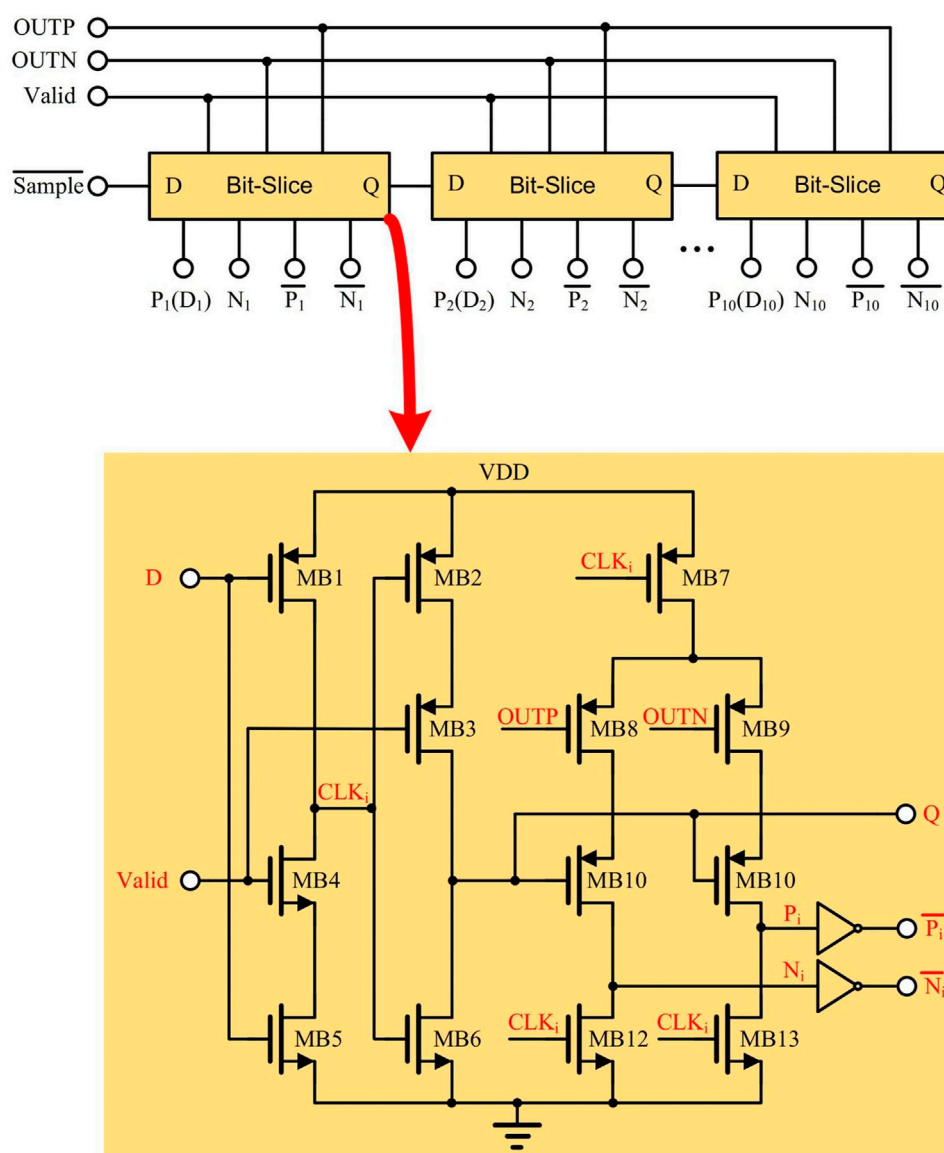


FIGURE 6
SAR control logic.

2.2 Comparator

Dynamic comparators are widely used in ADCs because of their low power consumption. In the application of the dynamic comparator, the NMOS is generally used as the input port [18–21]. As shown in Figure 4, in order to improve the accuracy of comparison, this paper uses PMOS as the input port for low VDD. The comparator work is divided into two phases. In the first phase, when CLK is high, MC1 is OFF, the paths connecting A and B to VDD are OFF, MC6, MC7, MC10, and MC11 are ON, A and

B are connected to ground, and the output ports OUTP and OUTN are high. In the second phase, CLK is low, MC6, MC7, MC10, and MC11 are OFF, the paths from A and B to ground are disconnected, MC1 is ON, VDD charges A through MC1, MC2, and MC4, and through MC1, MC3, and MC5 charges B. The charging speed is related to the voltage of IP and IN. If $IP > IN$, the voltage of A is greater than the voltage of B. Since MC4, MC5, MC8, and MC9 constitute a positive feedback latch circuit, eventually the voltage of A will become low, the voltage of B will become high, OUTP will become high, and OUTN will become low

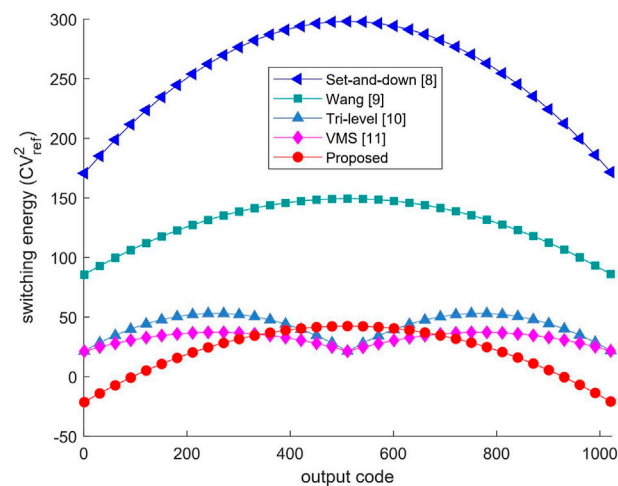


FIGURE 7
Switching energy against output codes.

TABLE 1 Comparison of energy saving and Common-mode shift for different switching schemes of a 10-bit SAR ADC.

Switching scheme	Average energy CV_{ref}^2	Energy saving	Common-mode shift
Conventional [12]	1,363.3	Reference	0
Set-and-down [8]	255.5	81.26%	512 LSB
Wang [9]	128	90.61%	512 LSB
Tri-level [10]	42.42	96.89%	512 LSB
VMS [11]	31.88	97.66%	256 LSB
Proposed	21.08	98.45%	1 LSB

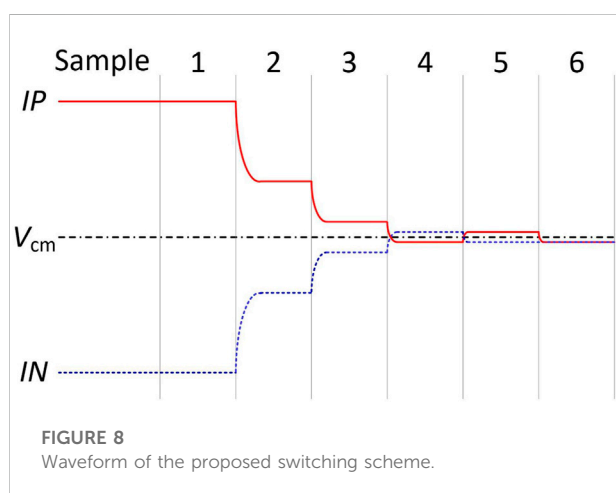


FIGURE 8
Waveform of the proposed switching scheme.

level. If $IP < IN$, then finally the voltage of A will become high, the voltage of B will become low, OUTP will become low, and OUTN will become high. During the operation of the comparator, there is no DC path from VDD to ground, so only dynamic power is consumed.

2.3 Sampling switch

In order to reduce the sampling error, the sampling switch generally adopts a bootstrap circuit [13, 14]. As shown in Figure 5, the bootstrap process is divided into two phases. In the first phase, when Sample is low, CLKA is high, MS1, MS2, MS3, and MS9 are ON, and MS4, MS5, MS6, MS7, and MS8 are OFF. At this time, A and D are low, B and C

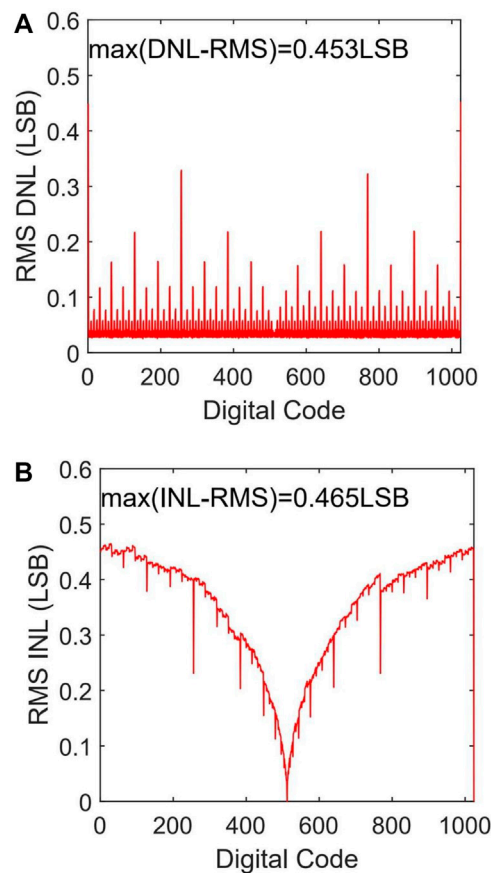


FIGURE 9
DNL and INL of DAC. (A) DNL. (B) INL.

are high. In the second phase, when sample is high, CLKA is low, MS1, MS2, MS3, and MS9 are OFF, MS4, MS5, MS6, MS7, and MS8 are ON, so the voltages of A and B are the input signals VIN. The voltages of C and D are bootstrapped as $V_{DD} + V_{IN}$. So the sampling switch MS8 realizes the bootstrap sampling.

2.4 SAR logic

The conventional SAR logic uses D flip-flop [8, 22, 23], which requires a large number of transistors and consumes a lot of power. In order to reduce the power consumption of the SAR logic, some papers use Bit-Slice circuit [15–17]. The Bit-slice circuit has fewer transistors and lower power consumption. As shown in Figure 6, during the sampling phase, Sample and Valid are high, P_i and N_i are low, \overline{P}_i and \overline{N}_i are high. After sampling, Sample becomes low, D of the first

Bit-Slice becomes high, CLK_1 becomes low. At this time, if OUTP is greater than OUTN, then P_1 becomes high level, \overline{P}_1 becomes low, N_1 keeps low, and \overline{N}_1 keeps high. If OUTP is smaller than OUTN, then P_1 keeps low, \overline{P}_1 keeps high, N_1 becomes high, and \overline{N}_1 becomes low. When Valid becomes low, the result of the first comparison is latched, and Q of the first Bit-Slice becomes high. According to the working principle of the first Bit-Slice, the second to tenth Bit-Slices sequentially save the results of the second to tenth comparisons.

3 Simulation results and discussion

Several switching schemes for 10-bit SAR ADC are simulated in MATLAB. The average switching energy of the proposed one LSB common-mode shift switching scheme for 10 bit SAR ADC is $21.08 CV_{ref}^2$. Compared with the conventional switching scheme [12], the average

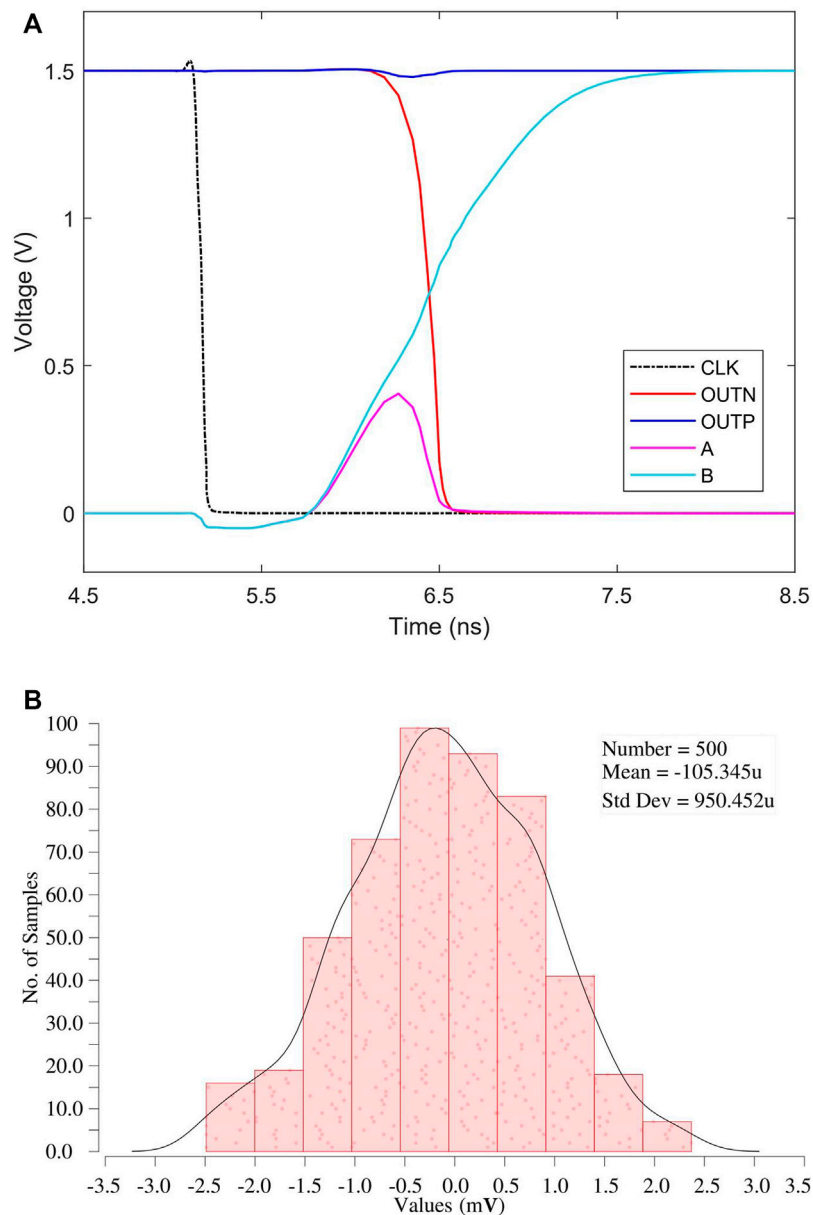


FIGURE 10

Simulation of dynamic comparator. (A) Transient simulation. (B) Monte Carlo simulation of the offset voltage.

switching energy is reduced by 98.45%. The switching energy at each output code for different switching schemes are shown in Figure 7. The comparison of several switching schemes [8–11] for 10-bit SAR ADC are shown in Table 1. These switching schemes [8–11] show great energy efficiency at the expense of very large common-mode shift. The common-mode shift of the proposed one LSB common-mode shift switching scheme shifts by one LSB which is less than those of the switching schemes [8–11]. The successive

approximation waveform of the proposed one LSB common-mode shift switching scheme is shown in Figure 8. From the first comparison to the $(N-1)^{\text{th}}$ comparison, the common-mode voltage remains V_{cm} , and in the last comparison, the common-mode voltage shifts by one LSB. Figures 9A, B show the 500 times Monte Carlo simulation results of the proposed DAC switching scheme. When the unit capacitance mismatch is $\sigma_u/C_u = 2\%$, the RMS DNL and RMS INL of the proposed DAC switching scheme

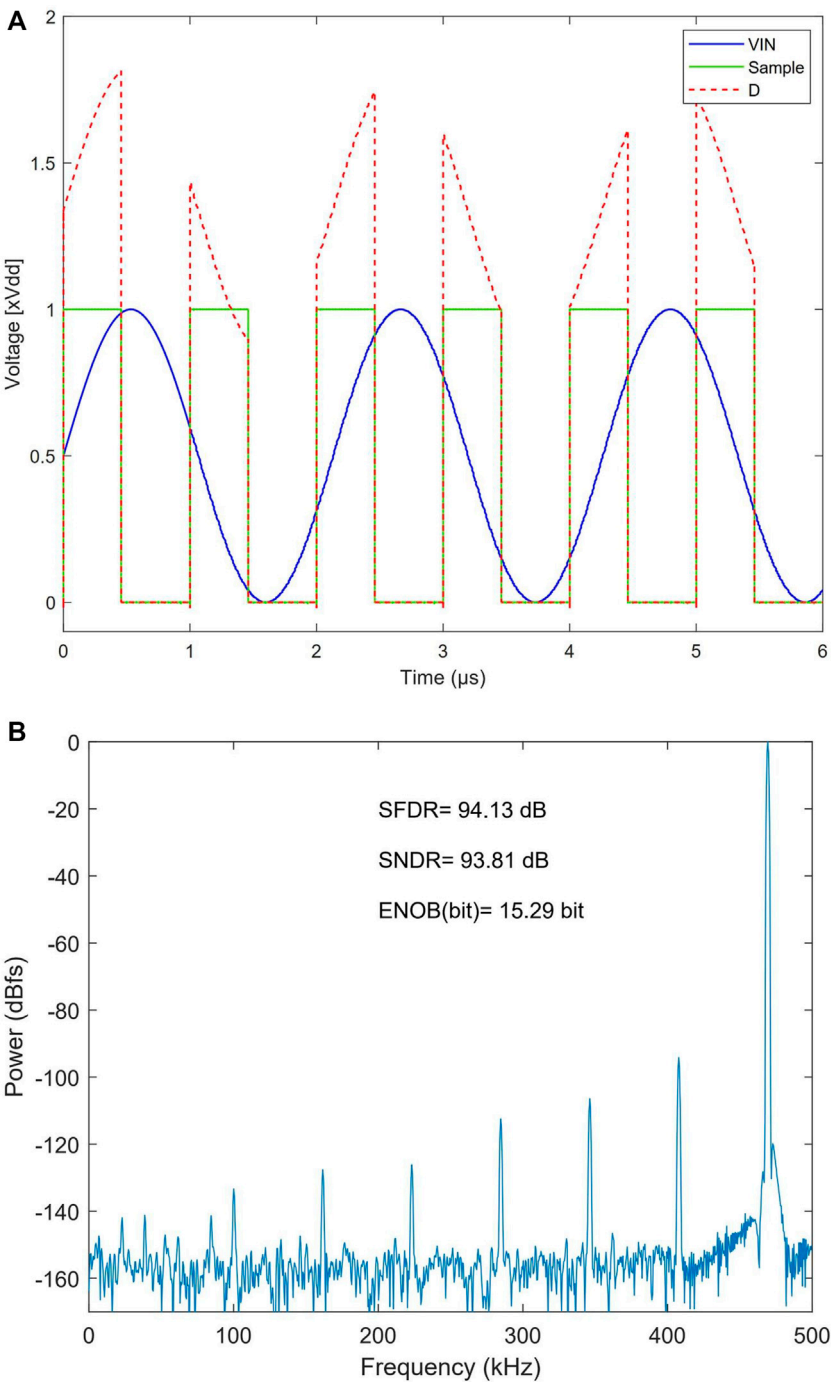


FIGURE 11
Simulation of bootstrapped sampling switch. (A) Transient simulation. (B) FFT of Bootstrapped sampling switch.

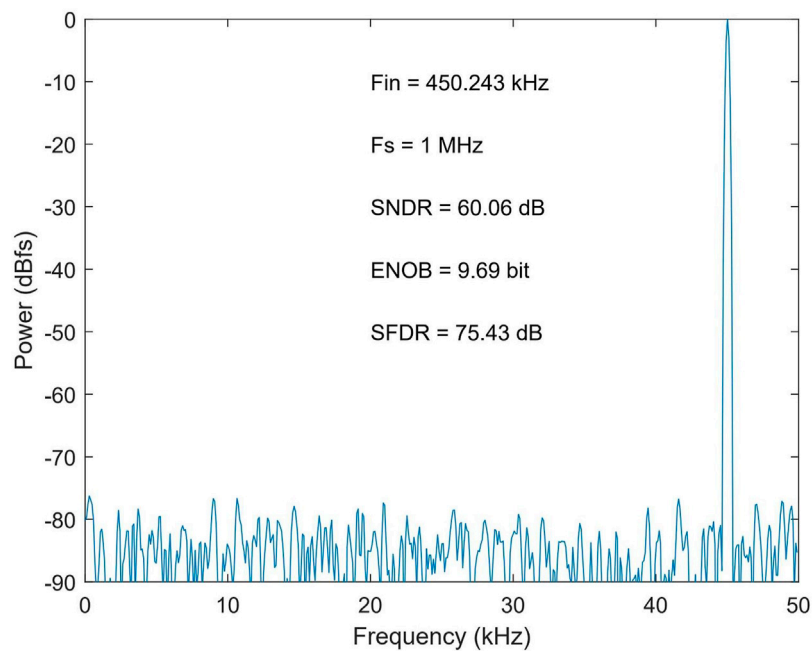


FIGURE 12
FFT of ADC.

are .453 LSB and .465 LSB respectively, meeting the requirement that the ADC non-linear error should be less than .5 LSB.

The transient simulation of the comparator is shown in Figure 10A. The differential input signals IP and IN of the comparator are 752.5 mV and 747.5 mV respectively. It can be seen from the figure that when CLK drops to low, A and B first increase the voltage together, and then gradually separate, one becomes higher and the other becomes lower. Finally, OUTP and OUTN become one high and one low. The comparator completes the output of comparison results. As shown in Figure 10B, the offset voltage of the dynamic comparator is 950.452 μ V after 500 Monte Carlo simulations. The offset voltage does not exceed 1.46 (1,500/1,024) mV.

The transient simulation diagram of bootstrap sampling switch is shown in Figure 11A. It can be seen from the figure that when the sampling signal sample is high, the control signal D of the sampling switch is bootstrapped up and changes with the input signal VIN. Therefore, V_{GS} of transistor MS8 remains unchanged during sampling, thus reducing the sampling error. Figure 11B shows the spectrum analysis results of the bootstrap sampling switch. The SFDR and SNDR are 94.13 dB and 93.81 dB respectively, and the ENOB of the sampled signal is 15.29 bit, which can meet the requirements of 10 bit SAR ADC.

The proposed SAR ADC was designed and simulated using 180 nm CMOS technology. The simulation settings are as follows: the power supply is 1.5V, the full swing input signal frequency is 450.243 kHz, and the sampling rate is 1 MS/s. Figure 12 shows the FFT spectrum of the proposed SAR ADC. The ADC achieves 75.43 dB spurious-free dynamic range (SFDR) and 60.06 dB signal-to-noise and distortion ratio (SNDR), respectively. Figures 13A, B show the variation of SFDR and SNDR with input signal frequency and sampling frequency. The simulated DNL and INL of the proposed SAR ADC are shown in Figure 14A, B. The peak DNL and INL are $-.30$ – $+.33$ LSB and $-.36$ – $+.20$ LSB, which are both less than .5 LSB. The proposed SAR ADC has a total power consumption of 10.45 μ W. Figure 15 shows the percentage of each circuit module in the total power consumption of the SAR ADC. Performance comparison of various ADC [24–28] is shown in Table 2. The proposed SAR ADC is suitable for image sensors. The Figure-of-Merit (FoM) was calculated from the following equation:

$$FoM = \frac{Power}{2^{ENOB} \times f_{sampling}} \quad (4)$$

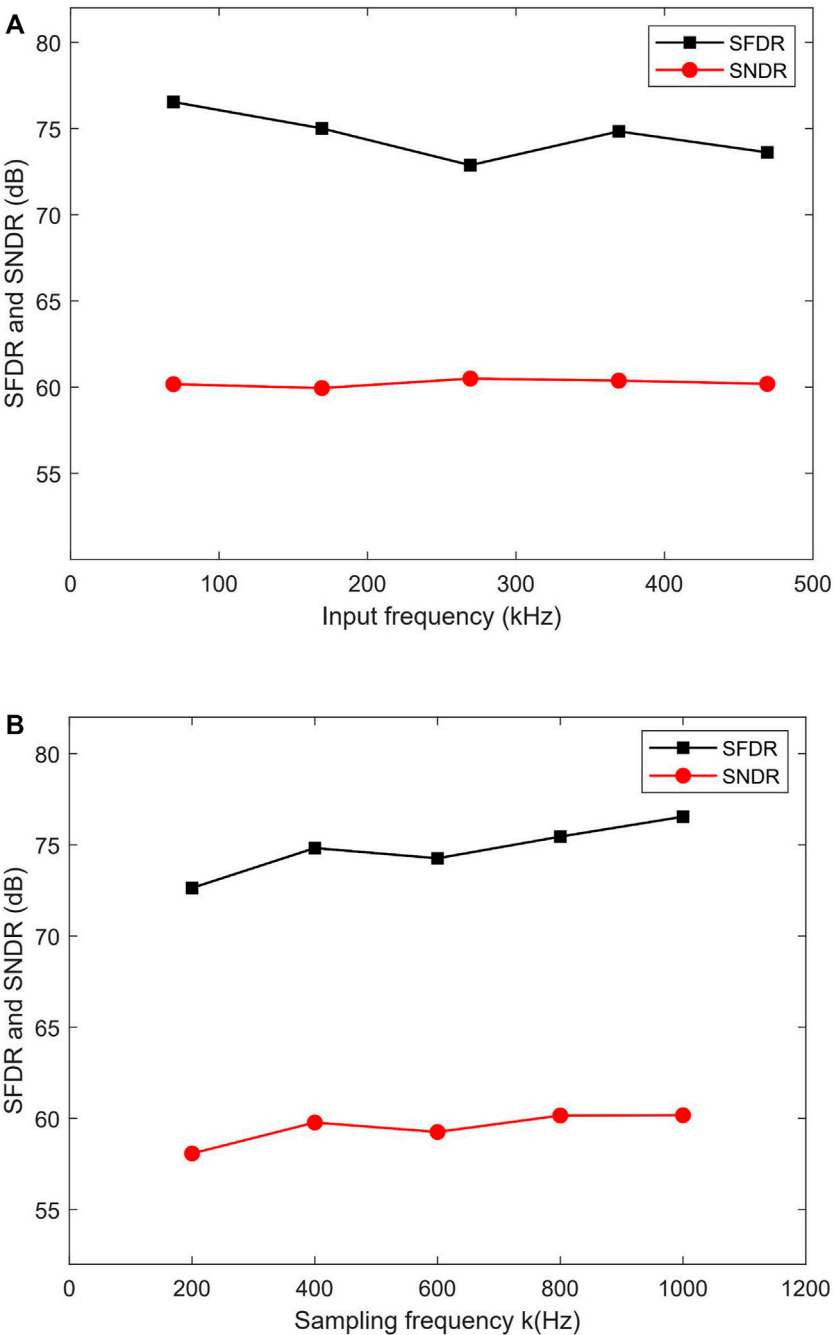


FIGURE 13 SNDR/SFDR with various input frequencies and various sampling frequencies. **(A)** Various input frequencies. **(B)** Various sampling frequencies.

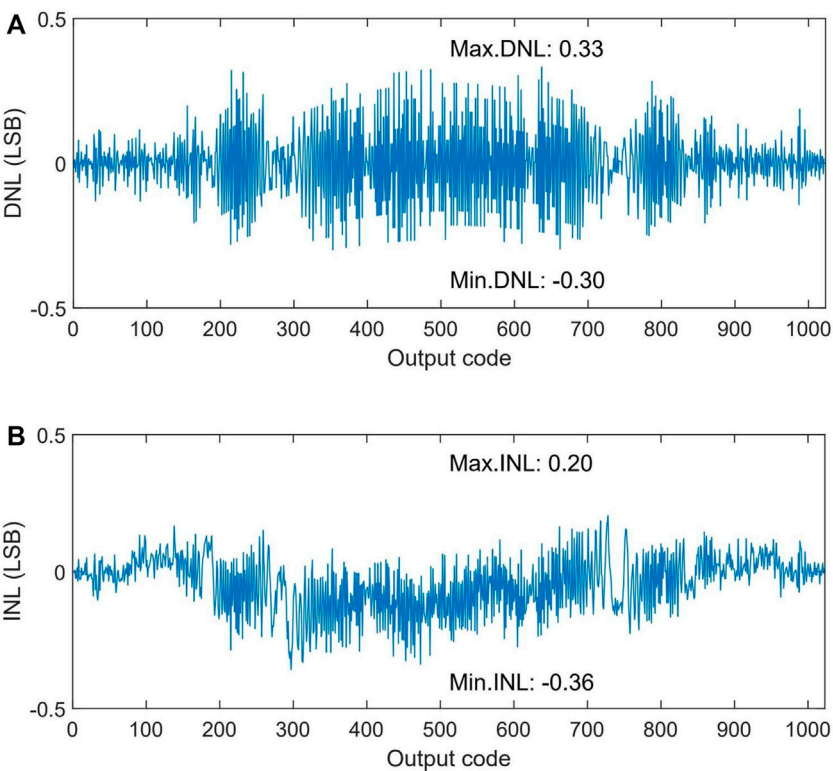


FIGURE 14
DNL and INL of ADC. (A) DNL. (B) INL.

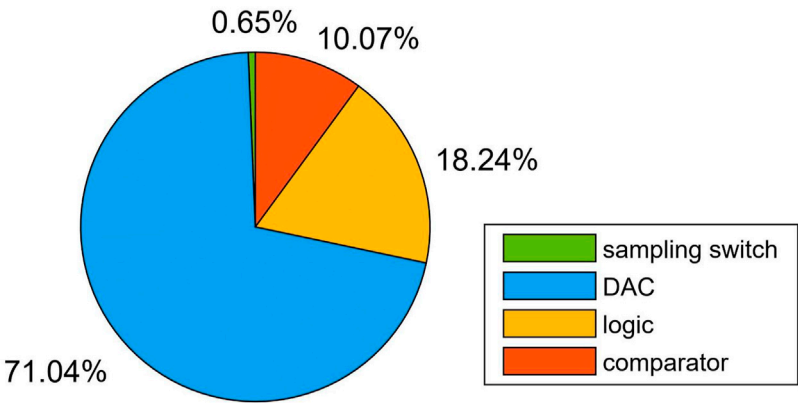


FIGURE 15
Power breakdown of the ADC.

TABLE 2 Performance comparison.

Parameter	[26]	[25]	[24]	[27]	[28]	This work*
Process (nm)	130	180	180	55	180	180
Resolution (bits)	10	8	10	10	12	10
Sampling Rate (MS/s)	1	1	1	1	1	1
Supply Voltage (V)	.8	1.8	1.2	1	1.4	1.5
SNDR (dB)	–	45.3	–	60.39	–	60.06
ENOB (bits)	8.8	7.23	8.7	9.74	11.25	9.69
DNL (LSB)	–.33/.56	.66	.4	–.5/.7	.54	–.30/.33
INL (LSB)	–.61/.55	.61	.46	–.7/.6	.89	–.20/.36
Power Consumption (μ W)	9	10.3	34.6	14.8	44.78	10.45
FoM (fj/conv. Step)	20	67	83	17.3	18.39	12.65

*Simulated results.

4 Conclusion

This paper has presented a 10 bit 1 MS/s low-power SAR ADC for image sensors. The proposed SAR ADC consists of DAC, dynamic comparator, bootstrap sampling switch and SAR logic. The DAC consists of positive capacitor array and negative capacitor array, and each array is composed of the same two sub-capacitor arrays. Based on these sub-capacitor arrays, the DAC uses a one LSB common-mode shift energy-efficient switching scheme to reduce power consumption. Compared with conventional switching scheme, the proposed switching scheme achieves an energy savings of 98.45%. In addition, the simulation shows that the offset voltage of the comparator and the ENOB of the sampling switch meet the requirements of ADC. Bit-Slice circuit makes the power consumption of SAR logic lower and the number of transistors less. Simulated in 180 nm CMOS process and 1 MS/s sampling rate, the ADC achieves 75.43 dB SFDR, 60.06 dB SNDR and 10.45 μ W power consumption. The FoM of the proposed SAR ADC is 12.65 fj/conv.-step. The proposed low-power SAR ADC is suitable for image sensors.

Data availability statement

The original contributions presented in the study are included in the article/Supplementary Material, further inquiries can be directed to the corresponding author.

Author contributions

YH: Conceived the project, organized the paper content, wrote and edited the manuscript. LH: Designed and

simulated the circuit. BT: Drawn the figure. ZY: Edited the manuscript.

Funding

This work was financially supported by the Key Field Project of Colleges and Universities in Guangdong Province (Grant no. 2022ZDZX1044), the Key Project of Social Welfare and Basic Research Project in Zhongshan City (Grant no. 2021B2020), the Construction Project of Professional Quality Engineering in 2020 (Grant no. YLZY202001), the Construction Project of Professional Quality Engineering in 2021 (Grant no. JD202101).

Conflict of interest

The authors declare that the research was conducted in the absence of any commercial or financial relationships that could be construed as a potential conflict of interest.

Publisher's note

All claims expressed in this article are solely those of the authors and do not necessarily represent those of their affiliated organizations, or those of the publisher, the editors and the reviewers. Any product that may be evaluated in this article, or claim that may be made by its manufacturer, is not guaranteed or endorsed by the publisher.

References

- Jin-Yi L, Kwang-Han C, Chen-Che K, Shih-Chin L, Yan-Jiun C, Pei-Chen L, et al. An 8-bit column-shared sar adc for cmos image sensor applications. In: 2015 IEEE International Symposium on Circuits and Systems (ISCAS). Lisbon, Portugal: IEEE (2015). 301–4. doi:10.1109/ISCAS.2015.7168630
- Xie S, Theuvsen A. A 10 bit 5 Ms/S column sar adc with digital error correction for cmos image sensors. *IEEE Trans Circuits Syst Express Briefs* (2020) 67(6):984–8. doi:10.1109/tcsii.2019.2928204
- Zhang X, Fan W, Xi J, He L. 14-Bit fully differential sar adc with pga used in readout circuit of cmos image sensor. *J Sens* (2021) 2021:2021–17. doi:10.1155/2021/6651642
- Choo KD, Xu L, Kim Y, Seol J, Wu X, Sylvester D, et al. Energy-efficient motion-triggered iot cmos image sensor with capacitor array-assisted charge-injection sar adc. *IEEE J Solid-state Circuits* (2019) 54(11):2921–31. doi:10.1109/JSSC.2019.2939664
- Byung-Geun L. Power and bandwidth scalable 10-B 30-ms/S sar adc. *IEEE Trans Very Large Scale Integr VLSI Syst* (2015) 23(6):1103–10. doi:10.1109/TVLSI.2014.2331354
- Lin JY, Hsieh CC. A 0.3 V 10-bit 1.17 F sar adc with merge and split switching in 90 Nm cmos. *IEEE Trans Circuits Syst Regul Pap* (2015) 62(1):70–9. doi:10.1109/TCSI.2014.2349571
- Zhangming Z, Yuhua L. A 0.6-V 38-nw 9.4-enob 20-ks/S sar adc in 0.18- μ m cmos for medical implant devices. *IEEE Trans Circuits Syst Regul Pap* (2015) 62(9):2167–76. doi:10.1109/TCSI.2015.2451812
- Liu CC, Chang SJ, Huang GY, Lin YZ. A 10-bit 50-ms/S sar adc with a monotonic capacitor switching procedure. *IEEE J Solid-state Circuits* (2010) 45(4):731. doi:10.1109/Jssc.2010.2042254
- Wang H, Zhu Z. Energy-efficient and reference-free monotonic capacitor switching scheme with fewest switches for sar adc. *IEICE Electron Expr* (2015) 12(7):20141202. doi:10.1587/ele.12.20141202
- Yuan C, Lam Y. Low-energy and area-efficient tri-level switching scheme for sar adc. *Electron Lett* (2012) 48(9):482–3. doi:10.1049/el.2011.4001
- Zhangming Z, Yu X, Xiaoli S. Vcm-based monotonic capacitor switching scheme for sar adc. *Electron Lett* (2013) 49(5):327–9. doi:10.1049/el.2012.3332
- Johns D, Martin K. *Analog integrated circuit design*. New York, USA: John Wiley & Sons (1997).
- Abo AM, Gray PR. A 1.5-V, 10-bit, 14.3-ms/S cmos pipeline analog-to-digital converter. *IEEE J Solid-state Circuits* (1999) 34(5):599–606. doi:10.1109/4.760369
- Zhu Z, Xiao Y, Liang L, Liu L, Yang Y. A 3.03 Mw 10-bit 200 Ks/S sar adc in 0.18 μ m cmos. *J Circuits Syst Comput* (2013) 22(4):1350026. doi:10.1142/s0218126613500266
- Harpe PJA, Zhou C, Yu B, van der Meijs NP, Xiaoyan W, Philips K, et al. A 26 Mw 8 bit 10 Ms/S asynchronous sar adc for low energy radios. *IEEE J Solid-state Circuits* (2011) 46(7):1585–95. doi:10.1109/jssc.2011.2143870
- Zhu Z, Xiao Y, Wang W, Wang Q, Yang Y. A 0.6 V 100 Ks/S 8-10 B resolution configurable sar adc in 0.18 μ m cmos. *Analog Integr Circ S* (2013) 75(2):335–42. doi:10.1007/s10470-013-0062-6
- Zhu Z, Xiao Y, Xu L, Ding H, Yang Y. An 8/10 Bit 200/100ms/S Configurable Asynchronous Sar Adc. *Analog Integr Circ S* (2013) 77 (2):249–255. doi:10.1007/s10470-013-0133-8
- Schinkel D, Mensink E, Klumperink E, Ev T, Nauta B. A double-tail latch-type voltage sense amplifier with 18ps Setup+Hold time. In: 2007 IEEE International Solid-State Circuits Conference Digest of Technical Papers. San Francisco, CA, USA: IEEE (20072007). p. 11314–605. doi:10.1109/ISSCC.2007.373420
- Babayan-Mashhadi S, Lotfi R. Analysis and design of a low-voltage low-power double-tail comparator. *IEEE Trans Very Large Scale Integr VLSI Syst* (2014) 22(2):343–52. doi:10.1109/TVLSI.2013.2241799
- Savani V, Devashrayee NM. Analysis and design of low-voltage low-power high-speed double tail current dynamic latch comparator. *Analog Integr Circ S* (2017) 93(2):287–98. doi:10.1007/s10470-017-1040-1
- Wicht B, Nirschl T, Schmitt-Landsiedel D. Yield and speed optimization of a latch-type voltage sense amplifier. *IEEE J Solid-state Circuits* (2004) 39(7):1148–58. doi:10.1109/JSSC.2004.829399
- Liu CC, Huang YT, Huang GY, Chang SJ, Huang CM, Huang CH. A 6-bit 220-ms/S time-interleaving sar adc in 0.18- μ m digital cmos process. In: 2009 International Symposium on VLSI Design, Automation and Test. Hsinchu: IEEE (2009). p. 215–8. doi:10.1109/VDAT.2009.5158133
- Cao ZH, Yan SL, Li YC. A 32 Mw 1.25 Gs/S 6b 2b/step sar adc in 0.13 μ m cmos. *IEEE J Solid-state Circuits* (2009) 44(3):862. doi:10.1109/Jssc.2008.2012329
- Saisundar S, Jia HC, Minkyu J. A 1.8v 1ms/S rail-to-rail 10-bit sar adc in 0.18 μ m cmos. In: 2012 IEEE International Symposium on Radio-Frequency Integration Technology (RFIT). Singapore: IEEE (2012). p. 83–5. doi:10.1109/rfit.2012.6401621
- Wen-Cheng L, Jhin-Fang H, Wei-Jian L. 1ms/S low power successive approximations register adc for 67-fj/conversion-step. In: 2012 IEEE Asia Pacific Conference on Circuits and Systems. Kaohsiung, Taiwan: IEEE (2012). p. 260–3. doi:10.1109/APCCAS.2012.6419021
- Yonghong T, Yong L. A 0.8-V, 1-ms/S, 10-bit sar adc for multi-channel neural recording. *IEEE Trans Circuits Syst Regul Pap* (2015) 62(2):366–75. doi:10.1109/TCSI.2014.2360762
- Verma D, Shehzad K, Khan D, Kim SJ, Pu YG, Yoo S-S, et al. A design of low-power 10-bit 1-ms/S asynchronous sar adc for dsrsc application. *Electronics* (2020) 9(7):1100. doi:10.3390/electronics9071100
- Kuo H-L, Lu C-W, Chen P. An 18.39 Fj/Conversion-Step 1-ms/S 12-bit sar adc with non-binary multiple-lsb-redundant and non-integer-and-split-capacitor dac. *IEEE Access* (2021) 9:5651–69. doi:10.1109/access.2020.3048979

Frontiers in Physics

Investigates complex questions in physics to understand the nature of the physical world

Addresses the biggest questions in physics, from macro to micro, and from theoretical to experimental and applied physics.

Discover the latest Research Topics

[See more →](#)

Frontiers

Avenue du Tribunal-Fédéral 34
1005 Lausanne, Switzerland
frontiersin.org

Contact us

+41 (0)21 510 17 00
frontiersin.org/about/contact

